Università degli Studi di Torino
**Scuola di Dottorato**

---

**Dottorato in Fisica**

# Understanding climate mechanisms and future projections using state-of-the-art Earth-system models: a focus on extreme precipitation and hot-spot regions

**Presented by: Olivia Ferguglia**

**Tutor: Prof.ssa Elisa Palazzi**

XXXVI cycle
February 2024

*En nuestras cosmovisiones somos seres surgidos de la tierra, el agua y el maíz, de los ríos somos custodios ancestrales el pueblo lenca. Resguardados por los espíritus de las niñas que nos enseñan que dar la vida de múltiples formas por la defensa de los ríos es dar la vida por el bien de la humanidad y de este planeta*

Berta Cáceres

*L'attuale modo di produzione e di consumo dei paesi capitalisti avanzati, basato su una logica di accumulazione illimitata, di spreco di risorse, di consumo ostentato e di distruzione accelerata dell'ambiente, risulta incompatibile con l'ambiente e non può assolutamente essere esteso all'intero pianeta, pena una grave crisi ecologica. Questo sistema è quindi necessariamente fondato sul mantenimento e sull'aumento delle disuguaglianze tra Nord e Sud, tra sfruttatori e sfruttati.*

Michael Löwy

# Ringraziamenti

Desidero esprimere la più profonda gratitudine alla Professoressa Elisa Palazzi per aver accettato di essere il mio tutor durante il dottorato. Grazie per la tua guida ed il supporto in questi quasi quattro anni, per avermi stimolata e per tutte le opportunità che mi hai offerto. Sei stata un mentore, non solo nell'insegnarmi cosa significa fare ricerca ma anche, guardando ogni giorno il tuo lavoro, come coniugarla con la divulgazione e l'insegnamento. Per questo ti ringrazio e non potrei essere più felice di continuare a lavorare e imparare con te.

Ringrazio il Professor Jost von Hardenberg e il Professor Enrico Arnone, i due co-supervisor su cui ho sempre potuto contare nelle due fasi del mio progetto di dottorato. Grazie per aver dedicato così tanto del vostro tempo e della vostra energia a questo lavoro ed in generale al mio percorso di formazione.

Desidero ringraziare le Professoresse Susanna Corti e Claudia Pasquero per aver accettato di far parte della mia commissione di dottorato e per aver valutato il mio manoscritto. Vi ringrazio per l'attenzione che avete dedicato al mio lavoro, per i suggerimenti e per le belle parole che avete speso nel giudicarlo. Un ringraziamento al Professor Claudio Cassardo per aver accettato di far parte della commissione.

Un sincero e speciale ringraziamento al Professor Nick Pepin per la bellissima accoglienza presso l'Università di Portsmouth, per essersi coinvolto da subito e con passione nel mio progetto e per i preziosi

consigli che mi ha offerto. Il tuo modo di interpretare i dati mi ha suggerito un approccio nuovo che porterò con me.
*I would like to express heartfelt and special thank you to Professor Nick Pepin for the warm welcome at the University of Portsmouth, for his immediate and passionate involvement in my project, and for the invaluable advice he has provided. Your way of reading and interpreting data has inspired a fresh approach that I will carry in my future researches.*

Grazie a tutte le dottorande, giovani ricercatrici, dottoresse e professoresse che ho incontrato in questi anni. Ognuna di voi mi ha ispirato con la sua passione e professionalità, offrendomi preziosi spunti ed una gran voglia di continuare questa avventura. Un grazie speciale a Elena, mia amica e punto di riferimento. Senza i tuoi consigli, a qualsiasi ora del giorno e della notte, non avrei finito nemmeno la triennale, figuriamoci il dottorato. E a te, devo il fatto di aver potuto anche solo pensare di arrivare fino a qui.

Grazie,
Alle mie amiche e ai miei amici, di una vita e per la vita.
Alle compagne, alle ame, che senza di loro avrei avuto tanto di quel tempo libero da non sapere come riempirlo.
A mia zia. A mia nonna, che si è stancata di sentirmi dire che studio più di quanto mi sia stancata io di studiare.
A mia mamma e a mio papà, che fin da piccola mi hanno insegnato la bellezza dello studio, lo stupore e la curiosità che hanno fatto della scienza e della ricerca prima la mia passione e poi il mio lavoro.
A mia sorella. Per l'infinito e incondizionato supporto, in ogni momento e per ogni cosa.

# Contents

# Abstract

The intensification of the hydrological cycle associated with climate change has resulted in a pronounced increase in extreme precipitation, particularly noteworthy in mountainous regions, that are also recognized as climate change hotspots. Recent assessments reveal an elevation-dependent stratification of long-term changes in various climate variables, such as precipitation. This phenomenon, referred to as Elevation-Dependent Precipitation Change (EDPC), is of particular concern due to its potential to trigger geo-hydrological hazards, making the projection of its future changes crucial. Climate models are an indispensable tool for analysing historical and future climate variability and change, although they are affected by uncertainties, largely attributed to the coarse model resolution and the use of parameterizations for sub-grid processes. The aim of this thesis was to provide new insights on extreme precipitation changes, firstly analysing model uncertainties in their future projections, then, focusing on high-elevated areas to assess the altitudinal stratification of the change in precipitation extremes using reanalysis data and state-of-the-art climate models.

To reduce the inter-model spread in precipitation extremes future projections, in the first part of this thesis the Emergent Constraints (ECs) methodology was used. An EC is a physically-explainable relationship between model simulations of a past climate variable (predictor) and projections of a future climate variable (predictand). By constraining the predictor through observations, it is possible to narrow future model projections of the predictand, as long as a significant correlation between the predictor and the predictand exists. The main challenge in determining an EC is establishing if the predictor-predictand relationship found is physically meaningful and robust to the model ensemble composition. Four previously documented ECs, tested with CMIP3/CMIP5 and focusing on extreme precipitation have been reconsidered in the thesis and their robustness and sensitivity to the ensemble composition evaluated. Most of the considered ECs did not survive the use of another model ensemble (CMIP6) nor the change in its composition, highlighting the limitations of applying this technique to precipitation extremes.

In the second part of the thesis, EDPC was investigated using ERA5 data and CMIP6 climate models. Altitudinal patterns in mean precipitation

and a selection of extreme precipitation ETCCDI indices trends were computed for the recent past, encompassing various global mountain regions: the Tibetan Plateau, the Greater Alpine Region, the US Rocky Mountains, and both the tropical and subtropical Andes. The analysis with ERA5 revealed the presence of an EDPC signal in most of the considered mountainous areas, showing consistency (i.e. same altitudinal stratification) in mean precipitation, extreme precipitation - R10mm, annual count of days when precipitation exceed the threshold of 10 mm/day - and persistency of rain condition - CWD, annual maximum number of consecutive wet days. Additionally, an enhanced wetting effect at high altitudes was observed in all areas, except the Rockies. A validation of the historical model experiment was performed to assess the CMIP6 model's capability in accurately simulating EDPC in the recent past. Good model performances were observed in the Tibetan Plateau and the Greater Alpine Region, while the Rockies and the tropical Andes posed significant challenges for CMIP6 models, displaying inconsistent behavior in representing extreme precipitation and its altitudinal stratification when compared to ERA5. The spatial resolution of CMIP6 models was found to play a crucial role in simulating the phenomenon, particularly in small or narrow areas.

In this context, further research aimed at identifying EDPC drivers and leading mechanisms might involve the use of the EC technique, using its capability to establish connections between various climate variables rather than narrowing the spread between climate models.

# Sommario

L'intensificazione del ciclo idrologico associato ai cambiamenti climatici ha comportato un marcato aumento delle precipitazioni estreme, particolarmente accentuato nelle regioni montuose riconosciute come hotspot dei cambiamenti climatici. Studi recenti hanno rivelato che i cambiamenti a lungo termine di diverse variabili climatiche mostrano una stratificazione con la quota, tra queste la precipitatione. Questo fenomeno, chiamato *Elevation-Dependent Precipitation Change* (EDPC), contribuisce all'acuirsi del rischio idro-geologico e per questo l'analisi del suo sviluppo nel futuro deve essere di primaria importanza. I modelli climatici rappresentano uno strumento indispensabile per analizzare la variabilità climatica nel passato e nel futuro, nonostante siano affetti da incertezze, principalmente attribuibili alla risoluzione spaziale dei modelli e all'uso di parametrizzazioni per includere i processi sotto-griglia. L'obiettivo di questa tesi è stato approfondire le variazioni della precipitazione estrema, analizzando inizialmente le incertezze dei modelli nelle loro proiezioni future. Successivamente, lo studio si è focalizzato sulle aree montuose per valutare la stratificazione altitudinale del cambiamento nelle precipitazioni estreme, utilizzando dati di rianalisi e l'output di modelli climatici globali.

Nella prima parte di questa tesi, è stata analizzata una nuova tecnica denominata *Emergent Constraints* (ECs), volta a ridurre la variabilità tra i modelli nelle proiezioni future della precipitazione estrema. Un EC è una relazione fisica tra le simulazioni del modello di una variabile climatica nel passato (*predictor*) e le proiezioni di una variabile climatica nel futuro (*predictand*). Vincolando il *predictor* attraverso dati osservativi, è possibile limitare l'incertezza nelle proiezioni future del *predictand*, purché tra i due sussista una correlazione significativa. La maggiore difficoltà nel determinare un nuovo EC è stabilire se la relazione trovata è fisicamente supportata e significativamente robusta rispetto alla composizione dell'*ensemble* dei modelli. In questa tesi, sono stati presi in considerazione quattro EC sviluppati per la precipitazione estrema, documentati in letteratura e testati con i modelli dei precedenti progetti CMIP3/CMIP5; ne è stata valutata la robustezza e la sensibilità alla composizione dell'*ensemble* dei modelli. La maggior parte degli EC considerati non ha superato questo test, evidenziando i limiti dell'applicazione di questa tecnica alle precipitazioni estreme.

Nella seconda parte della tesi, i dati di ERA5 e dei modelli climatici CMIP6 sono stati utilizzati per indagare l'EDPC. Sono stati calcolati i pattern altitudinali dei trend temporali della precipitazione media e di una selezione di indici ETCCDI per la precipitazione estrema, considerando un periodo nel passato recente ed includendo varie regioni montuose del globo: il Tibetan Plateau, la Greater Alpine Region, le US Rockies e le Ande tropicali e subtropicali. L'analisi con ERA5 ha mostrato la presenza di un segnale di EDPC nella maggior parte delle aree montuose considerate, mostrando coerenza (la stessa stratificazione altitudinale) nella precipitazione media, in quella estrema (R10mm) e nella durata massima dei periodi piovosi (CWD). Inoltre, è stato osservato un effetto di aumento delle precipitazioni ad alta quota in tutte le aree, ad eccezione delle Rockies. Le performance dell'esperimento *historical* dei modelli CMIP6 nel simulare l'EDPC nel passato recente sono state valutate, effettuando un confronto con il dataset ERA5. Buoni risultati sono stati riscontrati nel Tibetan Plateau e nella Greater Alpine Region, mentre nelle Rockies e nelle Ande, i modelli hanno ottenuto performances peggiori, mostrando un segnale di EDPC opposto rispetto ad ERA5. Dalle analisi condotte, è emerso inoltre come la risoluzione spaziale dei modelli CMIP6 sia un elemento fondamentale nella simulazione dell'EDPC, specialmente in aree montuose poco estese o particolarmente strette.
In questo contesto, ulteriori ricerche volte a identificare i *driver* e i meccanismi principali responsabili dell'EDPC potrebbero coinvolgere l'uso degli ECs, sfruttando la capacità di questa tecnica di stabilire connessioni tra diverse variabili climatiche piuttosto che concentrarsi sulla sua capacità di ridurre l'incertezza dei modelli climatici.

Chapter 1

# Introduction: the State of Art

## 1.1 Climate Change

Climate change is defined as the statistically significant long-term variation of averaged weather conditions and patterns. While it can occur naturally, driven by factors such as variations in the sun's activity or significant volcanic eruptions, since the 1800s human activities have increasingly taken on the predominant role in driving observed climate change. This is primarily attributed to the combustion of fossil fuels like coal, oil, and gas, to produce energy. Many of the changes in climate that have been observed are unprecedented in hundreds of thousands of years, and some of them, such as sea-level rise, are irreversible over hundreds to thousands of years (AR6 IPCC, Masson-Delmotte et al., 2021). The Intergovernmental Panel on Climate Change (IPCC), the international scientific body established by the United Nations (UN) in 1988, is tasked with assessing scientific information related to climate change, its impacts, and potential adaptation and mitigation strategies, synthesizing them in periodic assessment reports. The latest report (AR6, Masson-Delmotte et al., 2021) shows unequivocally that emissions of greenhouse gases from human activities are responsible for approximately 1.1°C of warming since 1850-1900, and it states that, averaged over the next 20 years, global temperatures are expected to reach or exceed 1.5°C of warming.
Numerous other aspects of climate change are directly influenced by global warming, including alterations in moisture levels, wind patterns, snow and ice cover, ocean conditions and variation in the global water cycle. Specifically, the interconnection between the global climate and the water cycle is profound: water plays a crucial role in

exchanging both mass and heat among the atmosphere, the ocean, the cryosphere, the biosphere, and the land surface and thus has an impact on climate. Similarly, climate change can significantly affect the water cycle: on the one hand, hydrological processes are influenced by climate variables, such as precipitation and temperature, On the other hand, the hydrological cycle affects the global energy budget, altering the radiation balance through the presence of clouds and atmospheric water vapor. In general, what has been observed over the last decades is that the hydrological cycle is accelerating and intensifying, triggered by global warming: temperature rise enhances evapotranspiration, precipitation, and intense precipitation.
Global water cycle can be described in terms of a mathematical relationship that represents the continuity equation in term of mass of water, taking into account the main hydrological processes. Taking a land surface water balance perspective, the cycle can be described as

$$P - E = Q + \frac{dS}{dT} \tag{1.1}$$

where P is precipitation, E is evapotranspiration, Q is runoff, and S is the total water storage in the basin.

***Precipitation*** Global mean precipitation changes are related to the Earth's energy balance, while regional changes are dominated by the transport of water vapor and by dynamical processes, particularly at scales smaller than ∼4000 km. As the climate changes, the competing constraints operating at global and local scales alter key water cycle characteristics, such as precipitation frequency, intensity, and duration (Allan et al., 2020). Global annual mean precipitation is projected to increase between 2% and 10% by 2100 under a high-emissions scenario. Moreover, along with an increase in global annual mean precipitation, changes in both frequency and intensity in the distribution of precipitation are expected (Thackeray et al., 2022)

***Evapotranspiration*** Surface evapotranspiration is a fundamental branch of the global water and energy cycles. Climate change causes modifications in evapotranspiration, influencing various hydrometeorological factors via interactions between the surface and the atmosphere. As the most evident mechanism, higher temperatures lead to more evaporation from water bodies and transpiration from vegetation, causing an increase in evapotranspiration rates in many regions

of the world. Moreover, shifts in the vegetation types, in the seasonality of snow and cultivation and the increase in extended periods of drought, will have strong impacts on evapotransipiration (Piao et al., 2007).

***Runoff*** Predicting changes in continental runoff with reliability is crucial for mitigating the adverse consequences of hydroclimate variability, including droughts, floods, and the associated losses of ecosystem goods and services. However, understanding how runoff responds to increasing atmospheric $CO_2$ levels is a complex task, influenced by intricate land-atmosphere processes and their interactions. Over land, the direct radiative forcing from $CO_2$-induced atmospheric warming can have dual effects: it may lead to increased precipitation and enhanced atmospheric evapotranspiration, resulting in both increased and decreased runoff, respectively. Furthermore, changes in precipitation characteristics, such as rainfall intensity and the fraction of precipitation falling as snow, can also influence runoff generation processes (Zhou et al., 2023).

Global mean evapotranspiration and precipitation are profoundly linked to the atmospheric and surface energy budget's response to radiative forcing (Deangelis et al., 2015), as described in Equation 1.2.

$$L_v P = LWC - SWA - SH \tag{1.2}$$

Latent heat flux, released through precipitation ($L_v P$), is balanced by the net atmospheric longwave radiative cooling (LWC) minus the heating from shortwave absorption (SWA) and sensible heating from the surface (SH).

Figure 1.1 shows a schematic representation of how global-mean precipitation responds to $CO_2$ forcing on two different timescales. The energy budget of the atmosphere (A) responds instantaneously to radiative forcing (B): as the greenhouse effect is enhanced by the increase in the $CO_2$, LWC decreases and so does precipitation. Then, after rapid and semi-rapid environment adjustments (C and D), involving land surface and vegetation response, further modifications in atmospheric circulation patterns and the ocean response, a long-term and different response comes out more clearly (E). The environment set to a new balance configuration with a higher equilibrium surface temperature: LWC increases, SWA increases owing to cloud feedbacks, and,

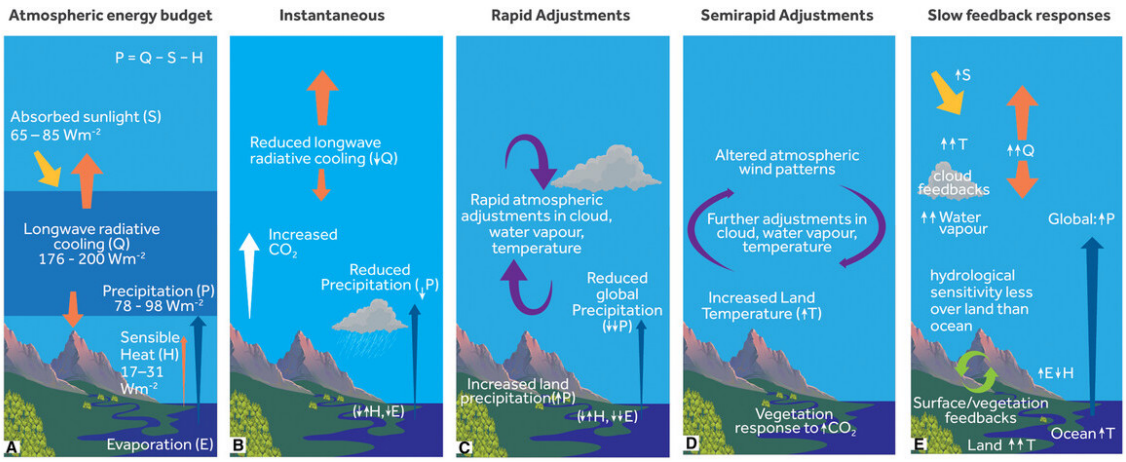


**Figure 1.1:** Schematic representation of the various responses of the atmospheric energy balance and global precipitation to high $CO_2$ levels. *Credit: Allan et al. (2020)*

as a result, global mean precipitation increases (Deangelis et al., 2015; Allan et al., 2020).
Another key factor that links global warming to the intensification of the hydrological cycle is the Clausius-Clapeyron equation (Equation 1.3), the quantitative relationship between atmospheric temperature and the water vapor.

$$\frac{de_s}{dT} = \frac{L_v}{T(\alpha_B - \alpha_A)} \sim \frac{L_v}{T(\alpha_B)^2} = \frac{L_v e_s}{R_v T^2} \tag{1.3}$$

where $e_s$ describes the water vapour pressure and $L_v$ the latent heat of vaporization. The latter two terms of the equation are derived by considering that the specific volume of water vapor ($\alpha_B$) largely exceed the specific volume of liquid water ($\alpha_A$), and by substituting the equation of state for water vapour.
This equation reveals that a temperature increase of 1°C, results in an approximate ∼7% increase in in the atmosphere's water holding capacity. Consequently, this leads to the enhancement of the global hydrological cycle, driven by increased evapotranspiration and precipitation. Due to this intensification, the study of the hydrological cycle and the evaluation of precipitation extremes have gained substantial importance, also in terms of the climate agenda. This is essential for the sustainable management of water resources and the evaluation and prediction of risks associated to the occurrence and intensification of water-related extreme events – such as floods and droughts – that can lead to catastrophes (e.g. chapters 4 and 11 of the IPCC AR6, Masson-Delmotte et al., 2021). The Special Report on Manag-

ing the Risks of Extreme Events and Disasters to Advance Climate Change Adaptation (SREX IPCC, Field et al., 2012) provided a comprehensive assessment on changes in meteoclimatic extremes and how exposure and vulnerability to these events determine the impacts and likelihood of disasters.

### 1.1.1 Climate change and its amplified effects in mountains

Mountains can be defined as geological structures in which cryospheric elements, such as snow, glaciers and permafrost, play a leading role. These elements are crucial to the planet's hydrological cycle as they contribute to the seasonal and long-term storage of water resources for roughly half of global population (Beniston, 2003). Hence, mountains are regarded as the planet's "water towers" (Viviroli et al., 2011; Pepin et al., 2022). Moreover, mountains are storehouse of biological diversity and endangered species: they support 25% of the terrestrial biodiversity and half of the world's biodiversity hot-spots is concentrated in mountains (Viviroli et al., 2007). The influence of mountains extends far beyond their ranges: they provide services to over half the global population, making them not only crucial for people living in mountains, but also for those living downstream: provisioning services (e.g. water, food, energy, timber); regulating services (mountain water cycle and regional feedbacks, modulation of runoff regimes, mitigation of the risks from natural hazards, water storage) and cultural and aesthetic services.

Globally, from the Andes to the Himalayas, the majority of mountain areas are experiencing serious environmental and ecological degradation, with numerous potential impacts including a decreasing in biodiversity (Sorte and Jetz, 2010), shrinking habitats for many species (Parmesan, 2006), reduced snowpacks (Mote et al., 2018), and retreating glaciers (Kuhn, 1989; Huss et al., 2017; Huss and Hock, 2018). A declining cryosphere leads to serious consequences, such as the possible reduction of water resources for billions of individuals in downstream regions across the globe (Viviroli et al., 2020) and the alteration of snowmelt timing from early spring to late winter (Musselman et al., 2017).

High-altitude regions have been identified as hot-spots of climate change: in the mountains, climate change is being faster compared to the globally-averaged signal, so that its consequences are anticipated or amplified with respect to what is occurring in the adjacent low-land areas. Evidences of the acceleration of climate change can be seen in

all the "climatic spheres", particularly in the cryosphere with glaciers retreat, changes in snowpack depth and seasonality, permafrost thawing, ice and rock avalanches, formation of glacier lakes and their outburst floods, and in the atmosphere with weather and climate *whiplash effect*, defined as abrupt shifts in precipitation regimes from wet extremes to dry extremes or vice versa.
In 2019, a Special Report on the Ocean and Cryosphere in a changing climate (SROCC, Portner et al., 2019) was released, featuring an entire chapter dedicated to high-altitude mountain areas. This chapter's primary emphasis lies in the assessment of recent and projected transformations in high-elevation regions, particularly pertaining to glaciers, snow cover, permafrost, as well as lake and river ice. It also goes into the causes of these alterations and their implications for the various services furnished by the cryosphere, along with associated adaptation strategies. The key message is unequivocal: there is an urgent need to enhance the monitoring of mountain environments to gain a deeper understanding of the factors driving observed changes and to predict how mountains will respond to future climate conditions.

***Elevation Dependent Warming*** In the last ten years, many studies have assessed that mountain warming rates are elevation-dependent. Elevation dependent warming (EDW) - literally the stratification of warming rates with the elevation - has been observed in different mountain regions of the globe (Pepin et al., 2015), often with higher rates of warming having occurred at increasingly higher altitudes over the past decades.
To assess the existence of EDW, different steps are suggested (see NextDataProject report): first of all, long-term temporal trend (or rate of change) of surface temperature (mean, minimum or maximum) are calculated. The second step involves evaluating whether the warming signal exhibits a dependence with the elevation. This analysis entails calculating the slope obtained through a linear regression of temperature trends against the elevation. This regression can be carried out at each grid point (for gridded observational datasets, reanalysis products, and model data) or location (for station data), or data can be averaged within elevational bands (Palazzi et al., 2016). When the rate of the temperature trend is found to exhibit a statistically significant relationship with the altitude, it can be concluded that EDW is occurring. This characterization can be applied on a global scale, within specific regions, or even localised in a single mountain range. In principle, the slope does not need to be strictly positive or

negative, as in accordance with the literal definition of EDW, or necessarily linear which is often not the case; however, it must demonstrate systematic behavior (Palazzi et al., 2016).
EDW has been assessed using various datasets, including in-situ measurements, satellite and reanalysis data, as well as model simulations, each having its own strengths and weaknesses. The majority of studies based on observations suggests that an enhanced warming is occurring at higher elevations while some others show an opposite sign of EDW, no elevational-dependency or even a more complex situation (e.g. no significant elevational gradient but highest warming rates at intermediate elevations) (Pepin et al., 2015).

The SROCC IPCC special report (Portner et al., 2019) offers a comprehensive overview of mean annual surface air temperature trends in mountain regions, summarising findings from 40 studies that used a total of 8703 observation stations over different time periods, partly overlapping. On average, the rate of warming in mountain areas is recorded at **0.3°C per decade**, slightly higher than the global average of 0.2°C per decade. Pepin et al. (2022) conducted comparisons between individual mountain regions and their adjacent lowland areas and in many cases, notable differences in warming rates were observed. Particularly, in 20 cases, warming rates are found to be enhanced with increasing altitude, while in just 5 cases, they show a negative dependence. The altitudinal-dependency of warming rates is particularly pronounced in the Tibetan Plateau, the Great Alpine Region, the Andes, and US Rockies Mountains. In the same study, Pepin et al. (2022) emphasized a relevant issue related to the assessment of EDW. It is essential to consider the lack of consistency in the approaches and data used for evaluating EDW, which includes variations in time periods, the selection of comparison stations, temporal and spatial resolutions, the chosen elevation ranges, and other factors. This lack of consistency can complicate the comparison and review of studies, hindering the identification of general patterns.

***Precipitation in mountains*** Mountainous regions display distinctive dynamics that exert localized impacts on large-scale climatic patterns. The effect of orography results in pronounced spatial climate variability within mountainous areas (Daly, 2006). The presence of complex terrain can significantly influence local precipitation through orographic lifting of air masses, a phenomenon that facilitates condensation and cloud formation (Napoli et al., 2019). As a result, the to-

tal precipitation in mountainous areas includes both the amount that would occur without the relief and an orographic component due to the intensified precipitation formation mechanism over mountains, driven by the forced uplift of air masses by the terrain (Johnson and Hanson, 1995). This combined effect leads to an increase in rainfall with the altitude, commonly referred to as **orographic enhancement of precipitation**. The amount of orographic precipitation varies across different spatial scales and is influenced by several factors. These factors encompass synoptic-scale pressure patterns, local vertical motion arising from terrain complexity, such as steepness and slope orientation, and microphysical processes within clouds, including the presence of aerosols and the evaporation of falling raindrops (Barry, 1981).
The response of orographic precipitation to climate change depends on many aspects: firstly, as many studies highlight, shifting the freezing level at higher altitudes cause a increase in liquid precipitation at the expense of solid precipitation, resulting in a strong decrease in the snowpack and a higher risk of floods (Siler and Roe, 2014). Moreover, changes in wind speed or direction manage to displace and modify atmospheric moisture transport and consequently the quantity of precipitation (Shi and Durran, 2014). Analyzing severe orographic precipitation poses a significant research challenge due to the complexity of the phenomena and the limited distribution of station data, as well as the heterogeneity in its availability. Despite these challenges, such analyses remain of outstanding importance as they represent a serious threat to infrastructures, cities, and populations (Abbate et al., 2022).

### 1.1.2 Climate extremes

The Fifth Assessment Report (AR5, Stocker et al., 2013) and the SREX (Field et al., 2012) of IPCC have provided compelling evidence, based on observations, that climate extremes have undergone substantial changes since the mid-20$^{\text{th}}$ century, primarily as a result of human influences. Furthermore, these changes are projected to enhance in the future. On a global scale, many of the shifts in climate extremes can be attributed directly to the increase in the radiative forcing associated with global warming, the expansion of atmospheric water-holding capacity, and the modifications in vertical stability and meridional temperature gradients that impact climate dynamics (Chapter 11, AR6-IPCC, Masson-Delmotte et al., 2021).
Starting from the IPCC definition, extreme weather events are defined as “events that are rare at a particular place and time of year”

and **extreme climate events** as a "pattern of extreme weather that persists for some time, such as a season" (Chapter 11, AR6-IPCC, Masson-Delmotte et al., 2021). Nevertheless, the definition of rare is not unique, numerous criteria exist to assess the occurrence of an extreme weather or climate event, depending on distinct geographic regions.
From a strictly mathematical standpoint, an extreme event can be defined as an uncommon occurrence situated at either the upper or lower end of a particular variable's value range. The likelihood of values falling within this range is described by a probability distribution or density function, often exhibiting a shape resembling a normal or Gaussian distribution (Henderson-Sellers, 1995).
Figure 1.2 illustrates the impact on temperature distribution resulting from variations in both the mean and variance, with particular emphasis on their influence on extreme events. In figure 1.2a, increasing only the average temperature, the range between the hottest and coldest temperature does not change, however this could result in the emergence of previously unrecorded, exceptionally high temperatures in this hypothetical climate scenario. An increase in the variability but not in the mean indicates an increase in the probability and in the amplitude of both hot and cold extremes (Figure 1.2b). When both the mean and variability increase (Figure 1.2c), the probability of hot and cold extremes is affected, with more frequent hot events and fewer cold events. This suggests that the relative alterations in extreme events are significantly more pronounced than the relative changes observed in the mean and standard deviation.

The probability distribution function of daily rainfall looks very different from the gaussian distribution curve of temperature (Chapter 10, Henderson-Sellers, 1995); consequently, changes in both mean and variability would lead to very different results. For example, daily precipitation follows a gamma distribution (Equation 1.4)

$$f(x) = \frac{\left(\frac{x}{\beta}\right)^{\alpha-1} e^{-\frac{x}{\beta}}}{\beta\Gamma(\alpha,\beta)}, \alpha, \beta > 0 \tag{1.4}$$

where $x$ is the precipitation amount, $\Gamma$ is the Gamma function and $\alpha$ and $\beta$ are the shape and scale parameters, respectively.
This equation can be mathematically integrated to derive the probability of exceeding a specific rainfall threshold. For instance, the 95$^{\text{th}}$

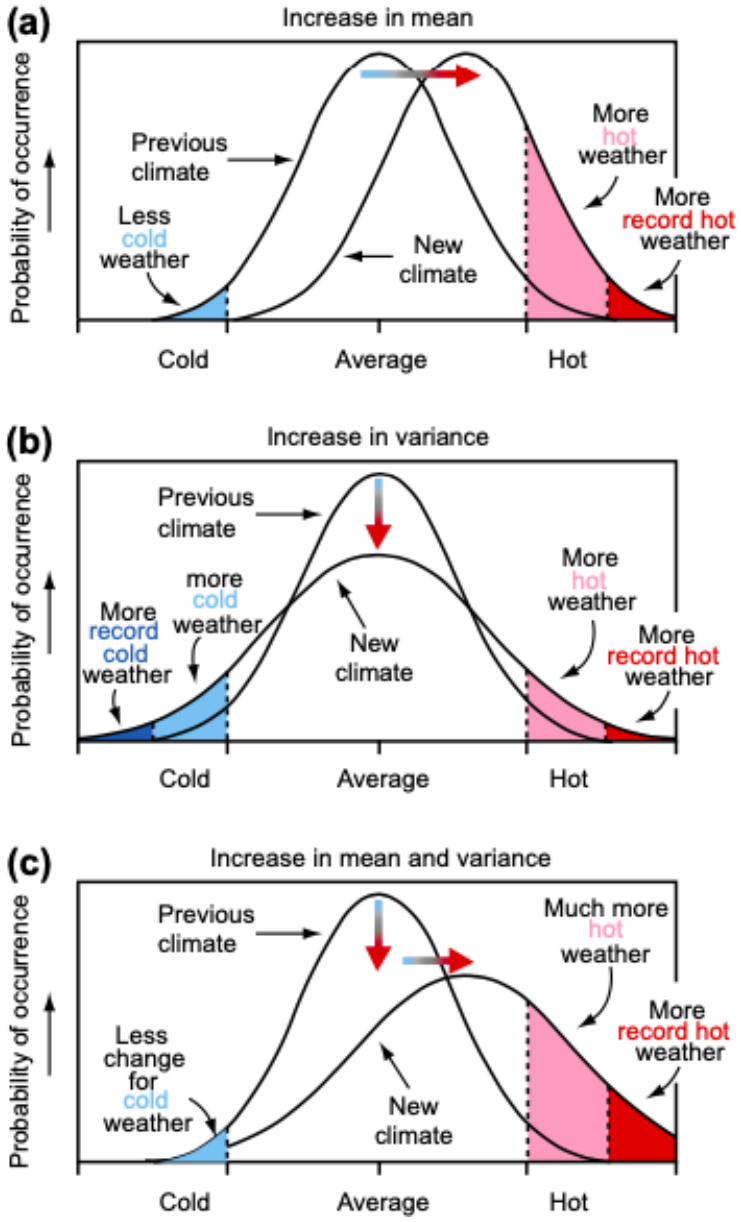


**Figure 1.2:** Schematic representation showing the effect on temperature extremes when (a) the mean temperature increases, (b) the variance increases, and (c) when both the mean and variance increase for a normal distribution of temperature. *(Credits: Figure 2.32 from Watson and the Core Writing Team (AR3-IPCC, 2001))*

percentile of the Gamma distribution might be selected as the threshold value at which precipitation would be categorized as "intense" or "extreme".

When we have to deal with extreme events, we need to consider that their outcomes occur with very low probability and this could affect

the representation of the tail of the probability distribution: the Extreme Value Theory (EVT) is a branch of statistics and probability theory that deals with the study of extreme or rare events. In particular, this theory aims to analyse the tail ends of probability distributions, describing the minimum or maximum values (e.g. yearly maximum one day precipitation) obtained from large sets of independent random variables or threshold exceedances (e.g., the precipitation amounts above a specified large value).
Nonetheless, these statistical methods were initially formulated to handle isolated extreme events within a dataset, consequently, they may not be universally applicable to defining extreme events characterized by persistence (e.g., heatwaves or droughts), the simultaneous behavior of multiple variables, or events considered extreme due to their spatial extent (Chapter 10, Henderson-Sellers, 1995). Large international efforts have been taken to elaborate a standardize definition of climate extremes; in the early 21$^{st}$ century, the World Meteorological Organization (WMO) and the World Climate Research Program (WCRP) established the Expert Team on Climate Change Detection and Indices (**ETCCDI**) and defined 27 representative climate indices to assess extremes in climate change globally and regionally (Karl et al., 1999b). Extremes like the annual maximum daily precipitation (Rx1day) or the annual maximum wind speed have conventionally been modeled using one of three distinct Extreme Value Distributions in engineering applications. While a few of these indices may align with the conventional definition of extreme events, the majority do not.

### Precipitation extremes under climate change

Precipitation extremes and extreme events in the context of climate change has been subject of numerous studies, considering the consequences that they may have on both human society and ecosystems (Chapter 4, SREX-IPCC, Field et al., 2012). These events are expected to increase in both frequency and intensity, not just in the global mean but across nearly all latitudes, differently to what has been assessed for total precipitation (Thackeray et al., 2022). Understanding changes in precipitation extremes is a research challenge. On the one hand, the record of precipitation might be insufficient to detect long-term trends of rare events; on the other hand, changes in both atmospheric dynamics, thermodynamics and microphysics need to be considered simultaneously to assess and understand the overall

effect.

To better understand how extreme precipitation events react to rising temperatures, a useful approach is to begin with an approximation of the equation that describes the surface precipitation rate during such events:

$$P \sim -\epsilon\{w(p)S(T,p)\} \tag{1.5}$$

where $\epsilon$ is the precipitation efficiency, $w$ is the vertical velocity in pressure coordinates (negative for upward motion), $S(T,p)$ is the derivative of the saturation specific humidity $q_s$ with respect to pressure $p$ taken at constant saturation equivalent potential temperature (along a moist adiabatic) and $\{\ \}$ is a mass-weighted vertical integral over the troposphere.
This equation can help separating all different contribution: **thermodynamical** ($S$ depends only on pressure and temperature), **dynamical** ($w$ is the vertical velocity) and **microphysical** (from changes in the precipitation efficiency).

**Thermodynamical** Warming leads to an expansion of the atmosphere's water-holding capacity, in accordance with the Clausius–Clapeyron (C-C) relationship (see Equation 1.3). This thermodynamic effect causes a concurrent rise in extreme precipitation on a global scale. It suggests that precipitation extremes will escalate at a similar rate, or possibly even more rapidly, if the strength of the updrafts associated with extreme precipitation events increases as the climate warms (Chapter 11, AR6 IPCC, Masson-Delmotte et al., 2021).

**Dynamical** At the regional level, alterations in extreme precipitation patterns are further influenced by changes in atmospheric dynamics. Large-scale climate phenomena, e.g. the North Atlantic Oscillation (NAO) or El Niño–Southern Oscillation (ENSO), contribute to the modulation of extreme precipitation through variations in environmental conditions or the intensity of storms. On a more localized scale, additional dynamic factors can contribute: the future warming trend may intensify extreme monsoonal precipitation events; moreover, shifts in both tropical and extratropical cyclogenesis (convective precipitation) can lead to modifications in extreme precipitation patterns or alterations in sea surface temperatures can impact extreme precipitation patterns

near coastal areas (Chapter 11, AR6 IPCC, Masson-Delmotte et al., 2021).

**Microphysical** The effectiveness of transforming atmospheric moisture into precipitation may be modified by cloud microphysical changes due to warming; this could lead to shifts also in precipitation extremes. Research has shown that aerosols can influence significantly heavy precipitation: a reduction in atmospheric aerosols induces warming, thereby causing an increase in extreme precipitation, as a thermodynamic consequence (Samset et al., 2018). Furthermore, alterations in atmospheric aerosol levels also trigger dynamic transformations, as observed in tropical cyclones (Takahashi et al., 2017).

In conclusion, the thermodynamic alterations caused by warming lead to a pronounced increase in extreme precipitation, following a rate close to the one described by the C-C relationship. Nevertheless, the impacts of warming-induced shifts in dynamic drivers on extreme precipitation are more complex and challenging to quantify; they constitute a source of significant uncertainties in climate future projections and warrant further research.

## 1.2 Assessing mountain precipitation and extremes with observational based datasets

The majority of mountainous environments and ecosystems around the world are responding rapidly to ongoing climate change, therefore it is fundamental to monitor climate and weather conditions of those environment. Long-term climatological time series are essential for enhancing our comprehension of the leading mechanisms and in providing more realistic projections of future impacts. According to the widely used definition, 13–30% of the global land surface (excluding Antarctica) can be considered mountainous, but still high elevation regions tend to be comparatively under-represented (Thornton et al., 2022). As assessed by the SROCC IPCC special report (Chapter 2, Portner et al., 2019), the possibility to detect changes in various components of the high mountain cryosphere and attribute them to specific climate drivers is limited by the paucity of in-situ station and the reduced spatial density and temporal extent of observation records at high elevations. Those gaps in observations pose serious challenges in quantifying past trends and in simulating future evolution of the

mountain climate.

There are many methods and datasets that can be used to assess specifically precipitation and precipitation extremes in mountain areas: ground *in-situ* rain gauge station, weather radar networks, satellite observations, atmospheric reanalysis, or model-based investigations. It is fundamental to acknowledge both advantages and limitations associated with each of these sources.

***In-situ stations*** In mountains, in-situ data assume a great importance in unraveling the complexity of physical processes. However, they are affected by the limitation of data coverage, that includes the geographical or spatial coverage - the density of station distribution -, the temporal coverage - the length of station records - , and the elevational coverage of a given set of observations. In their work, Thornton et al. (2022) considered spatial, temporal, and elevational coverage for daily frequency records of global precipitation, analysing its data coverage, geographical differences and common patterns. What they found is that spatial and temporal data coverage varies greatly between mountain regions globally, spatial density and record length appear partially inversely related: e.g., dense but short records in North America, with longer but less dense records in Africa, Asia, and Siberia. Moreover, data collected from traditional rain gauges are susceptible to systematic measurement **biases**: in mountainous areas, the significant occurrence of snowfall (Goodison et al., 1998), the substantial spatial variability of orographic precipitation, and elevated wind speeds (Kochendorfer et al., 2017) exacerbate the challenges of reliable data collection.

***Weather radar and satellite based products*** Weather radar networks offer precipitation estimates characterized by high spatial and temporal resolutions. However, in mountainous regions, the accuracy of radar-derived rainfall estimates tends to be compromised due to various observational limitations, for example the beam blockages and its interaction with the vertical structure of precipitation (Mei et al., 2014). Additionally, radar observations have limited applicability in cold weather conditions, as the radar beam primarily detects snow, making the assessment of surface precipitation more challenging (Schneebeli et al., 2013). Satellite-based estimates of precipitation can potentially provide a solution to the spatial sampling limitations of ground-based sensors but are affected by different source of uncertain-

ties. First of all, their temporal coverage is still limited for detecting climate trends and their statistical significance (Palazzi et al., 2016). Secondly, satellite-based precipitation estimates can be hindered by cloud cover; in fact, clouds can obscure the view of the Earth's surface, making it challenging to accurately detect and measure precipitation. Furthermore, satellites may have difficulty in distinguishing between snowfall and rainfall, particularly in cold mountainous areas and this can lead to inaccuracies in estimating the type and amount of precipitation (Levizzani and Cattani, 2019). Moreover, inconsistencies among the available products raise concerns about their accuracy when applied to mountainous areas (Krakauer et al., 2013; Cattani et al., 2021).

***Observational gridded datasets and reanalyses*** Gridded precipitation datasets employ various interpolation techniques to estimate precipitation values on a regular grid, either regionally or globally; instead of relying solely on point measurements from individual weather stations, gridded datasets provide a comprehensive spatial representation of precipitation over a specific area. Recently, their development has increased, as they find widespread applications in climate studies, model evaluation, and water resource management (Merino et al., 2021). A significant advantage of interpolated datasets over in-situ stations is their ability to reduce biases arising from irregular station distribution, as they offer homogeneous spatial coverage of the region of interest. However, the creation of high-quality gridded datasets necessitates an adequate number of underlying weather stations within each grid cell to account for sub-grid variations. Unfortunately, the current distribution of available rain gauges is uneven, resulting in numerous grid cells lacking observational data. Furthermore, precipitation is a discontinuous variable with distinct spatial gradients, particularly in the case of convective precipitation. These factors together introduce substantial uncertainties (Merino et al., 2021). Gridded datasets can be generated by combining data from various sources, as is the case with reanalysis products. Reanalyses are constructed by assimilating a wide range of observational data, including information from weather stations, satellites, weather balloons, within numerical weather models. This data assimilation process yields a consistent dataset that spans several decades, enhancing the accuracy of estimated variables and providing a detailed representation of Earth's atmospheric and surface conditions.

## 1.3 Global Climate Models (GCMs)

In climatology, models are essential tools to study and understand mechanisms responsible for climate variability and they are fundamental to make projections for its future evolution.
In broad terms, a "mathematical" model of the climate system is formally defined as a mathematical representation of the Earth system based on physical, biological, and chemical relationships. Models have been developed to study the response of the climate to perturbations or forcings and, in particular, to perform projections of the future climate evolution in response to anthropogenic emissions of greenhouse gases and aerosols. They are based on key explicit equations, such as the Navier-Stockes equations, that need numerical methods to be solved. Therefore, solutions are discrete corresponding to the model spatial and temporal resolution. Initial and boundary conditions are interpolated onto the numerical grid to approximate real-world conditions. Even in models with the most refined resolution, the numerical grid remains too coarse to fully represent all phenomena within each cell, such as turbulence or cloud microphysics. Consequently, **parameterizations** are developed and implemented based on empirical evidence or theoretical postulates. However, given that they only capture the first-order effects and may not hold universally across all conditions, they may introduce large uncertainties in climate model simulations. A way to differentiate between different types of models is related to the number of components they include and the detail in the description of the processes that they incorporate. The most complex models are general circulations models or **Global Climate Models (GCMs)** which attempt to account for all the important properties of the system at the highest affordable resolution. On the other side of the spectrum, there are the energy-balance models (EBMs) the simplest models, in which variables are averaged over large areas (the entire Earth or latitude bands) and many processes are not included or simplified by means of parameterizations. Earth Models of Intermediate Complexity (EMICs) lie in between. GCMs provide the most precise and complex description of the climate system; presently, their grid resolution typically ranges from 50 to 200 kilometers, with ongoing advancements aimed at refining their precision. Because of the large number of processes that are included in these models, they require a high computational power. To basically explain how do they work, they divide the globe into a three-dimensional grid of cells and for each of them, the set of primitive equations are numerically solved,

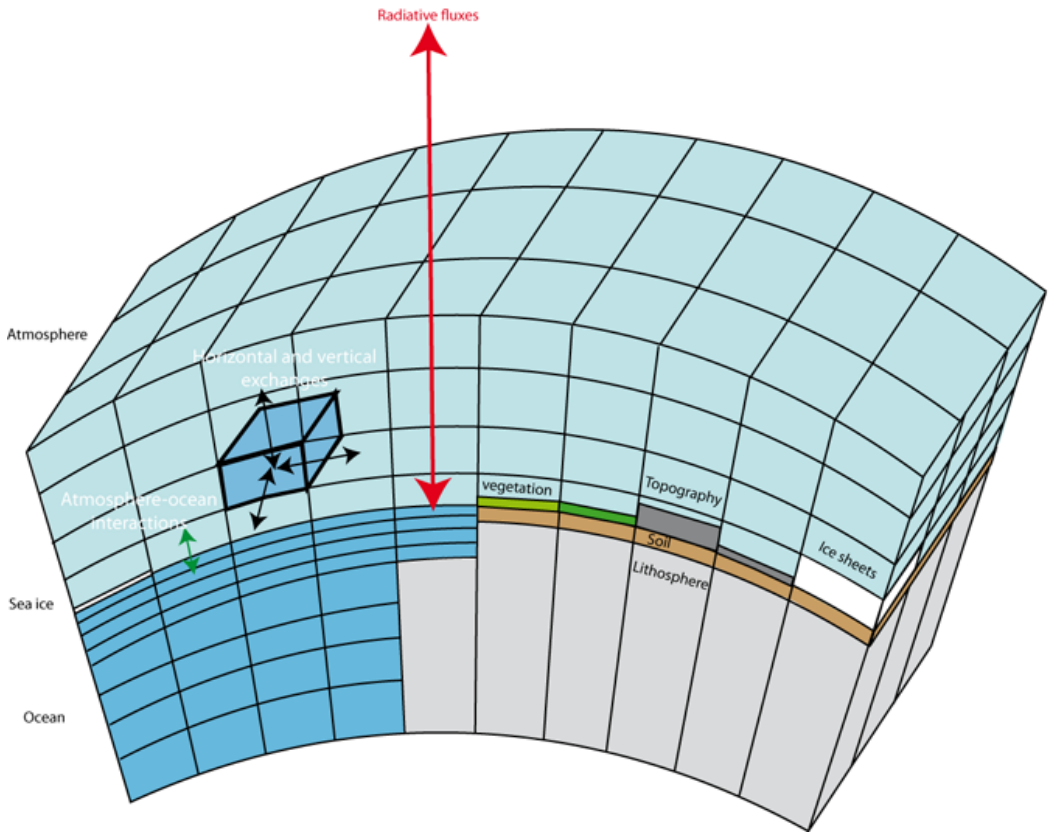


**Figure 1.3:** A simplified representation of a GCM, delineating some fundamental componets and processes. *Credits: Figure 3.6 from Goosse (2015)*

together with the employed empirical formulas and the parameterizations.

In order to analyse and validate models performances, in 1995 the Coupled Model Intercomparison Project (CMIP) was established by the global Working Group on Coupled Modelling. The primarily objective of the CMIP effort is to evaluate state-of-the-art climate models and assess their performance. Climate model evaluation and validation are crucial for understanding the strengths and weaknesses of climate models and enhancing their accuracy in simulating various aspects of the Earth's climate system. Secondary, they are essential in better understanding past, present and future climate changes arising from unforced variability or natural and anthropogenic forcings accounting for different scenarios. The most recent phase of CMIP (CMIP6, Eyring et al., 2016) provides the foundational data for the IPCC's Sixth Assessment Reports. Last but not less important goal is that CMIP multi-model outputs are available in a standardised format.

### 1.3.1 Model uncertainties

Figure 1.4 shows the three main source of model uncertainties that can be identified: natural internal variability (shown in orange), modelling uncertainties (blue) and scenario uncertainties (green).

**Natural internal variability**: Natural internal variability accounts

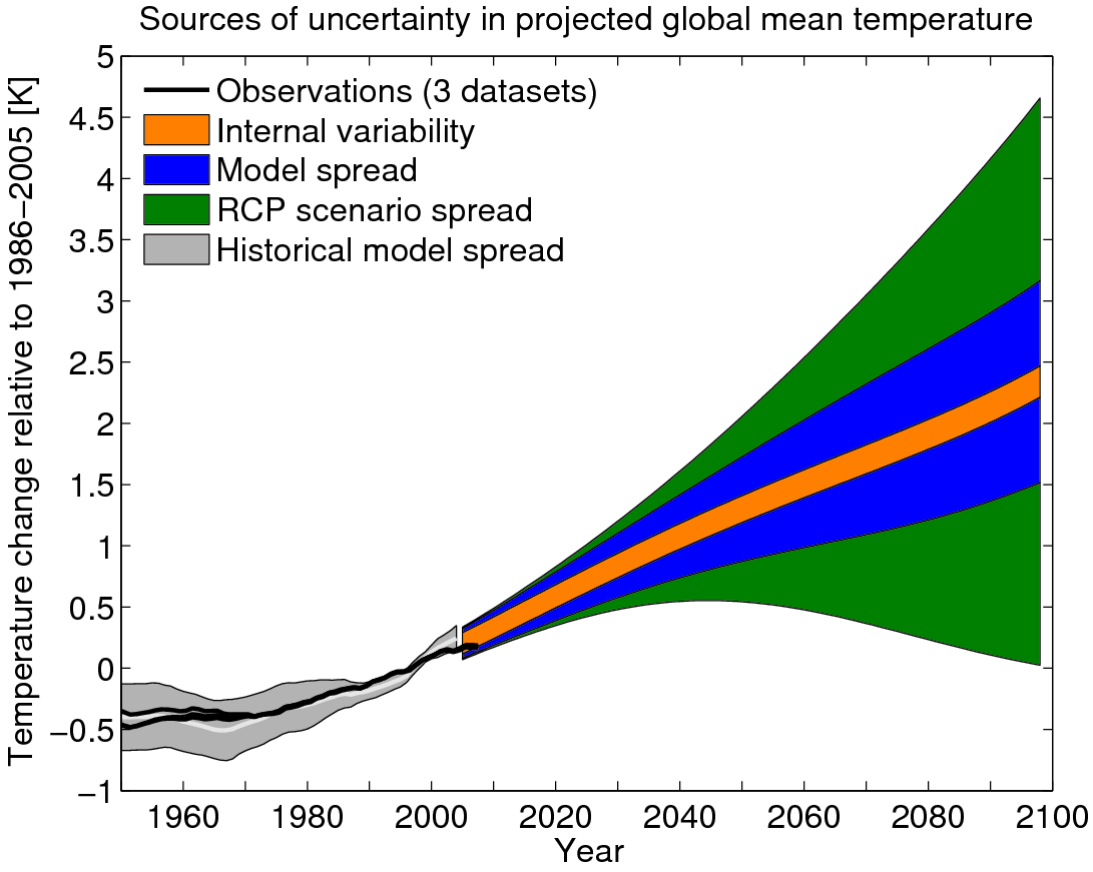


**Figure 1.4:** The sources of uncertainty in global decadal temperature projections, expressed as a 'plume' with the relative contribution to the total uncertainty coloured appropriately. The shaded regions represent 90% confidence intervals. *Credits: Figure 11.8a from Stocker et al. (AR5 IPCC, 2013)*

for the temporal variation of the climate system around a mean state due to its internal processes. The climate system has many components operating over different time scales that can affects each other. As a consequence, the average temperature of the planet shows variations on temporal scales that are shorter than those generally induced by external forcing, such as year-to-year or decadal variability. Reliable models of the climate system should be able to simulate how the system varies as an effect of internal processes (Neelin, 2010)

**Modelling uncertainties**: As already mentioned, climate models are highly complex computer programs that incorporate a large number of variables and use equations to simulate how the climate evolves over time. Since solutions are discrete, they can only provide outputs representing conditions at a specific resolution. Furthermore, each climate model is different from another, depending on how modelers have chosen to represent sub-grid processes through parameterizations, for example, or according to its own resolution. The implementation of different parameterizations introduces uncertainties in the models; combined with climate feedbacks, they can trigger further variability resulting in a greater spread among models that may not be easily discernible. Consequently, even when the models are fed with the same inputs, the results might differ. A deeper understanding of model uncertainties and their sources, as well as efforts to reduce the inter-model variability, are essential steps in model development, evaluation, and validation. These efforts aim to increase confidence in future projections.

**Scenario uncertainty**: Scenario uncertainty is related to the imperfect knowledge about the socio-economic and technological developments of the global society in the future, resulting in different greenhouse gas emissions. Scenarios can be defined as possible "stories" about the future evolution of greenhouse gas emissions based on how quickly human population will grow, how land will be used, what technologies and kind of energies will be employed. Figure 1.4 clearly shows that over long time scales, the uncertainty related to emissions scenarios is much larger than the model uncertainty and the natural variability.

### 1.3.2 Model uncertainties in precipitation and its extremes over mountain areas

Simulating precipitation and its spatial and temporal variability is an arduous exercise. One difficulty is related to the parameterizations of sub-grid processes that affect precipitation such as those for radiation, heat transfer, cloud microphysics, orographic lifting and deep convection (Palazzi et al., 2014; Arakawa, 2004; Stevens and Bony, 2013). Orographic precipitation mechanisms, such as orographic lifting, play an important role in determining patterns of small-scale precipitation

in areas with complex orography (Terzago et al., 2018).
As previously described in Chapter 1.1.2, precipitation and its extremes are additionally affected by microphysical aspects, specifically the ability of aerosol particles to alter cloud optical properties. The study conducted by Wilcox et al. (2013) emphasizes the importance of incorporating aerosol indirect effects into GCMs. This study suggests that the variations in model outcomes may be associated with the diverse ways aerosol load and cloud sensitivity to aerosols are represented. In particular, it is highlighted that CMIP5 models which include a representation of the indirect effects of sulfate aerosols provide a more accurate representation of the reduction in global mean annual-mean temperatures during the 1950s and 1960s, along with the simultaneous decrease in precipitation.

The Earth's hydrological cycle interconnects processes involving the atmosphere, lithosphere, biosphere, hydrosphere, and anthroposphere, making them all influential on precipitation, including its extremes. However, due to the multitude of land surface processes and the complexity of climate interactions between the surface and the atmosphere, including the full spectrum of potential implications for extreme hydrological events represents a challenge. Moreover, these processes are difficult to both measure and model, particularly when considering terrestrial components of the hydrological cycle, such as groundwater, snowmelt, and permafrost hydrology. These challenges introduce an additional significant sources of uncertainty into model projections. Furthermore, it is important to note that certain anthropogenic influences, such as irrigation, dams, river regulation, and agricultural land use changes and management, are often omitted in GCMs. In essence, a more comprehensive approach is required, involving detailed land hydrological simulations and land-atmosphere coupling simulations, to unravel the intricate interplay between human water usage and the global hydrology-climate system (Yang et al., 2021).

### 1.3.3 Emergent Constraints

In recent years, a methodology called "Emergent Constraints (ECs)", pioneered by Hall and Qu (2006), has been developed to reduce uncertainties in climate change projections. An EC is defined as a physically-explainable empirical relationship between intermodel variations in a quantity describing some aspects of the observed climate—the current climate predictor—and inter-model variations in a future pre-

diction of some climate quantity—the future climate predictand (Klein and Hall, 2015). The figure 1.5 shows a hypothetical linear relationship (the EC) between a varible A, called predictor, and a variable B, called predictand, simulated by 20 climate models. The idea is that, by constraining A through observations, in the plot represented by the blue shaded area, we can identify which models are more realistic in providing future projections of B, represented by the green shaded area.

The most important requirement for a trustworthy EC is that a strong

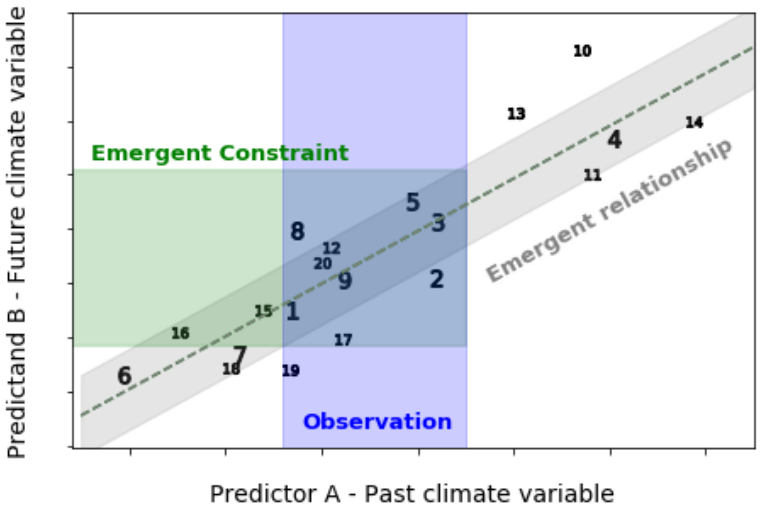


**Figure 1.5:** Schematic representation of the most common procedure to derive an EC between a predictor (x axis) and a predictand (y axis) simulated by climate models. The grey dotted line represents the hypothetical EC relationship, the blue shaded area the constraint made by the observation data and the green shaded area the result of the EC procedure, including all more realistic models in simulating the predictand.

physical explanation exists for the predictor-predictand correlation. A three-step definition has been proposed to establish an EC:

1. a potential EC is one in which a significant correlation exists between the predictor and the predictand;
2. a promising EC is when a physical explanation is proposed to support the correlation;
3. an EC is confirmed if a strong physically-based evidence that justifies the correlation between the predictor and the predictand (i.e., the proposed explanation at item 2) is verified (Klein and Hall, 2015)

Recently, Hall et al. (2019) presented a framework in which a potential Emergent Constraint (EC) is elevated to a confirmed status when accompanied by a plausible and explainable physical mechanism, and its resilience is assessed through out-of-sample testing (Simpson et al., 2021). Over the last few decades, as the potential of ECs as a technique to reduce inter-model spread gained recognition (Hall and Qu, 2006), numerous ECs have been tested and applied across various branches of climate science. These applications include studies on Equilibrium Climate Sensitivity, cloud feedbacks, analyses of the carbon cycle, high-latitude processes, applications to the hydrological cycle, and others (e.g. Brient, 2020; Williamson et al., 2021).
Of particular interest is the application of this technique to the hydrological cycle, especially precipitation. As previously noted, uncertainties surrounding the response of precipitation to global warming are considerable and demand further reduction. Furthermore, precipitation proves to be one of the most challenging variables to model, with precipitation formation mechanisms often integrated into models using parameterization (e.g., convection or orographic precipitation). O'Gorman and Schneider (2009) suggest that potential observational constraints for changes in precipitation extremes may lie in the connections between natural variability in extreme precipitation and temperature, particularly since the underlying physical mechanisms are relatively well understood. These constraints commonly suggest a substantial increase in heavy rainfall with warming (O' Gorman, 2012; Borodina et al., 2017). Nevertheless, the exploration of emergent constraints (ECs) in the context of precipitation and precipitation extremes has been limited, particularly in the context of the new CMIP6 phase models. This area presents a compelling and underexplored field for investigation.

## 1.4 Elevation dependency of climate change key-variables

As explained in Chapter 1.1.1, high elevation areas are attracting increasing attention by the scientific community: hot-spots, or sentinels, of climate change, mountains climatic equilibrium may be more rapidly promptly altered further showing early and enhanced signs of change. Moreover, signals of climate change could have a dependency with the altitude, as happens for temperature variance: **Elevation Dependent Warming (EDW)**. Due to the complexity and varied nature of mountain climates, quantify the pertinent processes is a

challenge. Consequently, the quantification of past and future climate change patterns as a function of elevation is affected by significant uncertainty (Pepin et al., 2022). As mountain regions are often isolated and experience harsh weather conditions, observational networks are either limited in their coverage or not structured to capture variations in climate with respect to elevation (Oyler et al., 2015). Moreover, measurements obtained from complex terrains typically exhibit unique characteristics; consequently when it comes to determine differential climate trends between mountainous areas and adjacent plains, it becomes imperative to have a high spatial data density. Furthermore, it is essential to have long-term time series data to evaluate the relationship between temperature trends and elevation, allowing the separation of the observed trends from any inter-decadal variability.

Gridded datasets that interpolate data from sparse networks, particularly in regions with intricate orography and limited data coverage, encounter these challenges and necessitate the use of sophisticated interpolation techniques (Daly, 2006), as discussed in chapter 1.2. Climate model simulations, either global or regional, can be used as valuable tools for investigating the mechanisms driving mountain processes, whether in historical simulations or future projections. Indeed, numerical models provide comprehensive outputs, comprehending all the required variables and their dynamic relationships to construct a comprehensive understanding of the processes governing EDW (Palazzi et al., 2019). Nonetheless, these models typically exhibit coarse spatial resolutions, meaning they do not fully capture, or only partially represent, the scales of spatial diversity within mountainous terrain and the pertinent meteorological phenomena. Moreover, they require observation based datasets for the validation process, making difficult to assess their robustness both in the past and consequently in future projections (Palazzi et al., 2016). Furthermore, numerical models depend on parameterizations to account for the sub-grid processes, and such processes, especially over mountainous regions, are still not fully understood (Chow et al., 2019).

### 1.4.1 Drivers of EDW

The EDW results from a combination of various physical processes, and accurately quantifying their individual contributions has proven to be a challenging task, as noted in previous studies (Minder et al., 2018; Palazzi et al., 2019). Generally, the rate at which tempera-

ture decreases with increasing elevation in mountainous regions is the result of the combination of the free-tropospheric temperature lapse rate and local effects, which are primarily governed by the surface energy balance. These local effects, which impact the temperature variation on a climatological scale, are influenced by various physical mechanisms. These mechanisms have been extensively described in previous reviews (Pepin et al., 2015; Rangwala and Miller, 2012), here will be briefly discussed. The physical shape of their relationship with the altitude is shown in Figure 1.6, as described by Pepin et al. (2015).

1. The **snow-albedo feedback** is a significant positive feedback mechanism in high altitudes regions, characterized by snow cover. As global and local temperature are increasing, the position of the snowline is expected to shift to higher elevations. The relationship between elevation and snow cover duration is nonlinear and the rate of retreat of the snowline is likely to accelerate with respect to the increase in temperature. This will result in a substantial increase in the absorption of incoming solar radiation leading to a progressively increase in temperature and an upward migration of the snowline (Pepin and Lundquist, 2008; Scherrer et al., 2012).

2. Increase in atmospheric water vapor pressure could increase downward longwave radiation, causing an enhancement in warming at high elevations (Rangwala et al., 2009, 2016)

3. The elevated moisture content in the atmosphere can lead to a smoother atmospheric lapse rate profile, meaning that air temperature decreases less rapidly with increasing altitude. This phenomenon is particularly significant in tropical regions (AR5 IPCC, Stocker et al., 2013)

4. The majority of atmospheric aerosol pollutants, such as atmospheric brown clouds and black carbon, are primarily concentrated at relatively lower elevations (below 3 km). This concentration is expected to reduce the influx of shortwave radiation to the lower slopes of mountains, a phenomenon known as the surface dimming effect. However, these pollutants typically have limited or no impact on higher mountains situated above the polluted layer (Pepin et al., 2015).

5. A specific alteration in radiative forcing triggers more pronounced temperature adjustments in colder conditions, which are frequently

encountered in mountainous regions. This occurs due to the Stefan-Boltzmann effect (Ohmura, 2012)

6. Changes in land cover that are tied to elevation-dependent factors, such as the systematic migration of vegetation species and the upward shift of treelines, have a notable impact on various aspects of the environment. These changes, in turn, influence surface albedo, energy flux distribution, and, consequently, climate in an elevation-dependent manner (Vitasse et al., 2012; Harsch et al., 2009)

The method developed in the literature to determine which variables can be classified as drivers of EDW (Palazzi et al., 2016; Rangwala et al., 2016) involves several steps. Initially, all variables that exhibit a substantial correlation with elevation and whose dependence on elevation aligns with the sign of the EDW rate are considered. Then, the actual drivers are identified as those variables which, independently of elevation, maintain a correlation with temperature changes at each grid point.

### 1.4.2 From EDW to EDCC

Recent accumulations of data have revealed that EDW involves more than just temperature variations. Changing in climatic forcing have induced modifications in the atmosphere, surface energy distribution, convection, cloud cover, precipitation, and the water cycle, along with shifts in air pollution. Therefore, it is more accurate to label this phenomenon as **Elevation-dependent Climate Change (EDCC)**, which encompasses changes in boundary layer stability, energy, water, greenhouse gases, and aerosols exchange between the Earth and the atmosphere (Kuhn and Olefs, 2020). Using the term EDCC implies the concept that various climatic variables, such as temperature o precipitation, may exhibit a dependency with altitude, with greater impacts at higher elevations compared to adjacent lowland areas.
This new concept is strictly related to the concept of Essential Mountain Climate Variable (EMCVs) (Thornton et al., 2021), a set of interdisciplinary variables that could provide a broad and realistic overview of mountain environment and climate change (e.g. evapotraspiration for hydrosphere and biosphere, glacier debris cover for cryosphere or aerosol absorption and scattering for atmosphere). The idea of EDCC is to investigate which of this EMCV exhibit a stratification with the elevation.

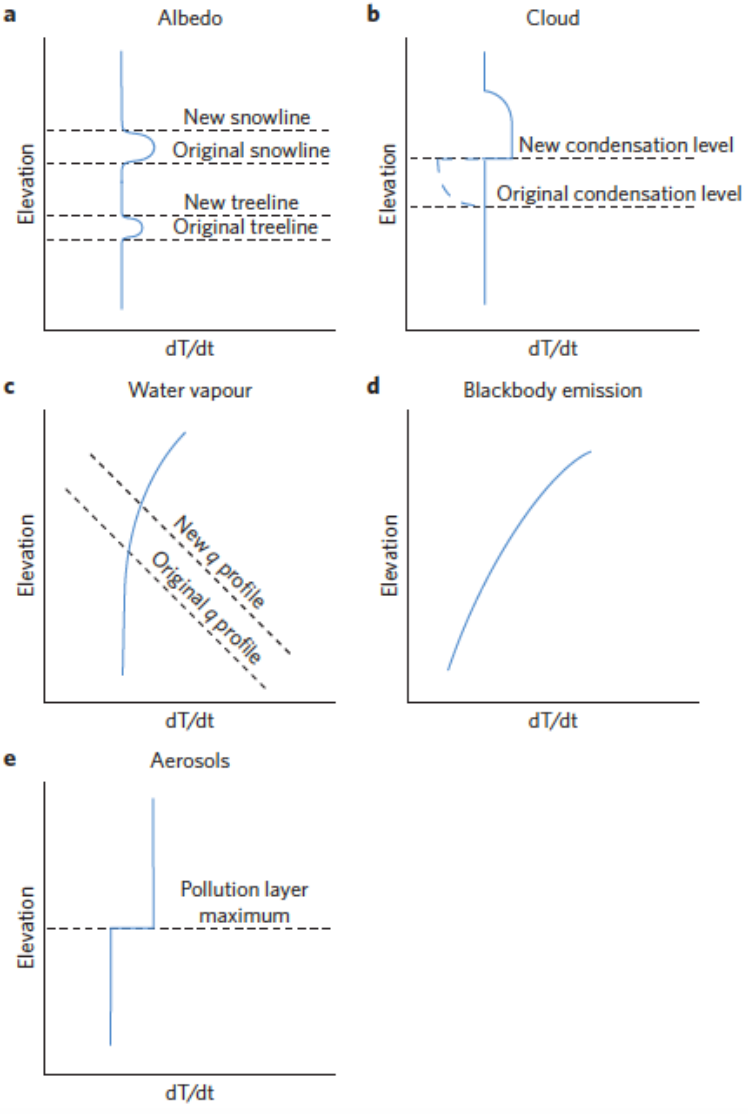


**Figure 1.6:** Schematic representation of the vertical profile of different EDW drivers. The specific aspects of each mechanism are discussed in the main text; the x-axis (dT/dt) denotes the warming rate (dT/dt). *Credit: Figure 2 from Pepin et al. (2015)*

Chapter 2

# Precipitation Emergent Constraints in CMIP6 models

Global warming is linked to the intensification of the hydrological cycle and together with the occurrences of extreme precipitation, as substantiated by mounting evidence from theoretical frameworks, observations, and model simulations (O'Gorman and Schneider, 2009; O'Gorman, 2015). To address the consequences of extreme precipitation events, such as floods, disruptions to ecosystems, and economic impacts, effective mitigation and adaptation planning necessitates accurate forecasts of extreme precipitation (Kotz et al., 2022). Nevertheless, contemporary state-of-the-art climate models display considerable uncertainty in predicting the extent of changes in extreme precipitation, especially notable at regional levels. Recently, a methodology called Emergent Contraints (ECs) have been developed in order to reduce model uncertainties. We recall that an EC is defined as a physically explainable relationship between a predictor, past climate variable, and a predictand, future projection, both simulated by models. The application of EC technique to reduce precipitation and precipitation extremes inter-model spread is affected by significant challenges. Firstly, the absence of long-term, high-quality observations of extreme precipitation with extensive spatial coverage impedes a reliable estimation of their changes (section 1.3.2). Secondly, the observed changes in extreme precipitation in past decades are influenced by both external factors and internal variability. Moreover, the EC relationships proposed for extreme precipitation projections are primarily applicable to large spatial averages, such as over tropical or extratropical wet regions as a whole, whereas decision-making neces-

sitates regional and local information (Zhang et al., 2022). Finally, the understanding of the physical mechanisms underlying many of the proposed ECs remains limited.
This chapter is broadly based on Ferguglia et al. (2023).

## 2.1 Robustness of EC in CMIP6

Recently, Caldwell et al. (2018) and Hall et al. (2019) showed that a relevant number of hydrological cycle-related ECs analysed in the literature lack a satisfying physical explanation: owing to the large number of possible observables and the relatively small number of models, spurious relationships might result by chance (Caldwell et al., 2014). Furthermore, most of the ECs recently published use models from only the Coupled Model Intercomparison Project phase 5 (Taylor et al., 2012, CMIP5) to test the statistical relationship between the predictor and the predictand. As suggested by Hall et al. (2019), to demonstrate the robustness of an EC, other model ensembles, and in particular then most recent CMIP6 (Eyring et al., 2016), should be used, a validation which, so far, has been performed only in a limited number of cases (Pendergrass, 2020; Schlund et al., 2020; Simpson et al., 2021).

The climate science community maintains a great interest in projecting future changes in precipitation due to their profound implications for both natural and human systems. Nevertheless, the complexity of the spatio-temporal variability of precipitation presents significant challenges in terms of both observation and prediction, as described in Sections 1.2 and 1.3.2. These factors contribute to the large inter-model uncertainties in future precipitation projections. It is crucial to reduce this uncertainty, particularly for policymakers and infrastructure planners who rely on model-based forecasts. EC technique has been applied to various aspects of the hydrological cycle across diverse scales, as documented in studies by Borodina et al. (2017); Deangelis et al. (2015); Li et al. (2017a); O' Gorman (2012); Rowell (2019); Watanabe et al. (2018); Zhang et al. (2022) and others. However, a recent published assessment of ECs analysed by Pendergrass (2020) reveals that using the new model ensemble CMIP6, the EC determined by Deangelis et al. (2015) reduces its robustness and strength while the one assessed by Watanabe et al. (2018) no longer exists. In the present section, we reconsider four precipitation ECs which were orig-

inally identified using previous generations of model ensembles (Meehl et al., 2007; Taylor et al., 2012, CMIP3 and CMIP5), and analyze to what extent they are still verified in CMIP6—including a comparison with CMIP5, checking both their existence in the new ensemble and their robustness as suggested by Simpson et al. (2021).

## 2.2 Data and Methods

The output of 27 global climate models (GCMs) from CMIP5 and of 29 GCMs from CMIP6 was analysed. The selected models are shown in Table 2.1 for CMIP5 and 2.2 for CMIP6. Data were downloaded from the Earth System Grid Federation (ESGF) with the Synda tool. We selected the models for which daily precipitation and monthly temperature data were available at the time when we downloaded the data (May 2021). The requirement of daily precipitation data is needed to calculate precipitation extremes indices. In order to accomplish a fair comparison among various models and between historical and future conditions, we considered only the models for which the same ensemble member was available both in the historical and in the scenario simulations. Data were selected from the historical experiment of each model, to define a present climatology, and from scenario simulations, using RCP8.5 in CMIP5 (Meinshausen et al., 2011) and SSP585 in CMIP6 (Kriegler et al., 2017), to define a future climatology. The time period chosen to define either the past or future climatology was not necessarily the same for each EC, as better explained in the following section and summarized in Table 2.3 (second and third column). The following model variables were considered: daily mean precipitation flux (pr), monthly near-surface air temperature (tas) and monthly surface temperature (ts).

The robustness for each EC was tested by assessing its sensitivity to variations in the model ensemble set. To achieve this, a bootstrap analysis was conducted on both model ensembles. This involved randomly selecting sub-samples, each comprising approximately two-thirds of the complete model set (unless otherwise specified), and repeating this procedure 10000 times to replicate the predictor-predictand relationship.

**Table 2.1:** List of 27 CMIP5 models considered in this study, accompanied by a key reference. The ensemble member r1i1p1 was considered for CMIP5.

| CMIP5 | | |
|---|---|---|
| Model name | Institution name | Reference |
| ACCESS1-0 | CSIRO-BOM | Bi et al. (2013) |
| ACCESS1-3 | CSIRO-BOM | Bi et al. (2013) |
| bcc-csm1-1 | BCC | Wu et al. (2013) |
| bcc-csm1-1-m | BCC | Wu et al. (2013) |
| CanESM2 | CCCma | Arora et al. (2011) |
| CCSM4 | NCAR | Meehl et al. (2012) |
| CESM1-BGC | NSF-DOE-NCAR | Hurrell et al. (2013) |
| CESM1-CAM5 | NSF-DOE-NCAR | Hurrell et al. (2013) |
| CNRM-CM5 | CNRM-CERFACS | Voldoire et al. (2013) |
| CSIRO-Mk3-6-0 | CSIRO-QCCCE | Rotstayn et al. (2012) |
| FGOALS-g2 | LASG-CESS | Li et al. (2013) |
| GFDL-ESM2G | NOAA-GFDL | Delworth et al. (2006) |
| GFDL-ESM2M | NOAA-GFDL | Delworth et al. (2006) |
| HadGEM2-CC | MOHC | Martin et al. (2011) |
| HadGEM2-ES | MOHC | Bellouin et al. (2011) |
| INM-CM4 | INM | Volodin et al. (2010) |
| IPSL-CM5A-LR | IPSL | Hourdin et al. (2013) |
| IPSL-CM5A-MR | IPSL | Hourdin et al. (2013) |
| IPSL-CM5B-LR | IPSL | Hourdin et al. (2013) |
| MIROC5 | MIROC | Watanabe et al. (2010) |
| MIROC-ESM | MIROC | Watanabe et al. (2011) |
| MIROC-ESM-CHEM | MIROC | Watanabe et al. (2011) |
| MPI-ESM-LR | MPI | Giorgetta et al. (2013) |
| MPI-ESM-MR | MPI | Giorgetta et al. (2013) |
| MRI-CGCM3 | MRI | Yukimoto et al. (2012) |
| MRI-ESM1 | MRI | Adachi et al. (2013) |
| NorESM1-M | NCC | Bentsen et al. (2013) |

## 2.3 General description of the chosen ECs and of their analysis methods

Each EC is identified with an acronym whose last letter indicates the initial of the surname of the first author that first proposed it. Here we provide a general overview of the four ECs considered in this study and describe the corresponding analysis method of each EC.

### ECT (from Thackeray et al., 2018)

ECT assesses a relationship between global-mean hydrological sensitivity and local changes in extreme precipitation. The global-mean hydrological sensitivity (global-mean HS, the predictor) is defined as the global-mean precipitation change normalized by global-mean surface air temperature change. The predictand is calculated as the change of the $99^{\text{th}}$ percentile of precipitation, normalized by the global-mean surface air temperature change ($\Delta P_{99}/\Delta T$). Changes are evaluated as the difference between the 2060–2099 future climatology and the

**Table 2.2:** List of 29 CMIP6 models considered in this study, accompanied by a key reference. The ensemble member r1i1p1f1 was considered for CMIP6.

| CMIP6 | | |
|---|---|---|
| Model name | Institution name | Reference |
| ACCESS-ESM1-5 | CSIRO | Ziehn et al. (2020) |
| ACCESS-CM2 | CSIRO-ARCCSS | Bi et al. (2013) |
| BCC-CSM2-MR | BCC | Wu et al. (2022) |
| CanESM5 | CCCma | Swart et al. (2019) |
| CESM2 | NCAR | Danabasoglu et al. (2020) |
| CESM2-WACCM | NCAR | Gettelman et al. (2019) |
| CMCC-CM2-SR5 | CMCC | Cherchi et al. (2019) |
| CMCC-ESM2 | CMCC | Cherchi et al. (2019) |
| CNRM-CM6-1 | CNRM | Voldoire et al. (2019) |
| EC-Earth3 | EC-Earth-Cons | Döscher et al. (2022) |
| EC-Earth3-CC | EC-Earth Cons | Döscher et al. (2022) |
| EC-Earth3-Veg | EC-Earth Cons | Döscher et al. (2022) |
| EC-Earth3-Veg-LR | EC-Earth Cons | Döscher et al. (2022) |
| FGOALS-g3 | CAS | Li et al. (2020) |
| GFDL-ESM4 | NOAA-GFDL | Dunne et al. (2020) |
| GFDL-CM4 | NOAA-GFDL | Adcroft et al. (2019) |
| IITM-ESM | CCCR-IITM | Krishnan et al. (2019) |
| INM-CM4-8 | INM | Volodin et al. (2017b) |
| INM-CM5-0 | INM | Volodin et al. (2017a) |
| IPSL-CM6A-LR | IPSL | Boucher et al. (2020) |
| KIOST-ESM | KIOST | Pak et al. (2021) |
| MIROC6 | MIROC | Tatebe et al. (2019) |
| MPI-ESM1-2-LR | MPI | Mauritsen et al. (2019) |
| MPI-ESM1-2-HR | MPI | Müller et al. (2018) |
| MRI-ESM2-0 | MRI | Yukimoto et al. (2019) |
| NESM3 | NUIST | Cao et al. (2018) |
| NorESM2-LM | NCC | Seland et al. (2020) |
| NorESM2-MM | NCC | Seland et al. (2020) |
| TaiESM | AS-RCEC | Lee et al. (2020) |

1960–1999 past climatology. The predictor and the predictand have been calculated as:

**Predictor**: Global-mean hydrological sensitivity, i.e., the global-mean precipitation change normalized by global-mean surface air temperature change.

**Predictand**: change of the 99th percentile of precipitation, normalized by the global-mean surface air temperature change. The predictand was determined by 1) computing the 99th percentile at each grid cell based on historical precipitation (excluding values lower than 0.1 mm/day); 2) calculating the total amount of precipitation above the percentile (P99) for both past and future time periods and the change between them ($\Delta$P99); 3) and normalizing the change by $\Delta$T.

Before using the CMIP5 and CMIP6 model outputs for calculating the predictor and the predictand, each model was remapped to a common 2°x2° latitude-longitude grid.

### ECL (from Li et al., 2017a)

ECL establishes a relationship between western Pacific precipitation and the change in Indian Summer Monsoon rainfall. The predictor is the past time- and space-mean daily precipitation in a western Pacific region (140°–190°W and 12°S– 12°N, WP precipitation) while the predictand is represented by the future change of mean daily precipitation averaged over the region 60°–95°E, 10°–30°N during the Indian Summer Monsoon season (May to September) normalized by global-mean SST change (ISM rainfall change). In this case the future change is evaluated as the difference between the 2070–2099 future climatology and the 1980–2009 past climatology.
**Predictor**: averaged precipitation over the region 140°–190° W and 12°S–12°N.
**Predictand**: change of mean daily precipitation averaged over the region 60°–95°E, 10°–30°N during the Indian Summer Monsoon season (May to September), normalized by SST change. SST was calculated from the surface temperature (ts), using a land-sea mask.
The change is the difference between the 2070–2099 climatology and the 1980–2009 climatology. Also in this case the CMIP5 and CMIP6 model outputs were remapped to a common 2°x2° latitude-longitude grid.
To calculate sea surface temperature from the surface temperature the following land-sea mask has been applied: following Gorman (2012), grid boxes with less than 90% ocean are excluded when considering ocean, and grid boxes with less than 90% land are excluded when considering land.

### ECG (from O' Gorman, 2012)

ECG defines a relationship between extreme tropical precipitation ($99.9^{\text{th}}$ percentile) scaled with surface air temperature over tropical oceans during the past reference period 1981–1999 (this quantity is referred to as "Sensitivity for variability", as in the original paper), and the future change in tropical extreme precipitation divided by temperature increase over the Tropics (called "Sensitivity for climate change"). In this context, the scaling procedure consists in calculating the slope between monthly time series of extreme precipitation and surface air temperature over the tropical ocean, then normalized by time- (1981–1999) and space- (the Tropics, between 30°S–30°N) averaged extreme precipitation. The future change is evaluated as the

difference between the 2081–2099 future climatology and the 1981–1999 past climatology.
**Predictor**: extreme tropical precipitation scaled with temperature increase over tropical oceans during 1981–1999 (Sensitivity for variability).
**Predictand**: tropical extreme precipitation change divided by temperature increase over the Tropics (Sensitivity for climate change).
The change is the difference between the 2081–2099 climatology and the 1981–1999 climatology. In this case, the CMIP5 and CMIP6 model outputs were remapped to a common 3°x3° latitude-longitude grid.
For the calculation of the precipitation extreme timeseries, we proceeded as follows: daily precipitation data were aggregated into monthly values over the tropical region (30°S–30°N) and the 99.9th percentile was computed. Monthly surface air temperature (tas) data were spatially averaged over the same tropical area. To obtain the Sensitivity for variability, the time series of precipitation extremes and of monthly temperature were calculated over the tropical oceans. The sensitivities for climate change were analyzed over the tropics including both land and sea areas. Timeseries were deseasonalized, by removing the mean seasonal cycle previously estimated, detrended and filtered with a 6-month running mean. Then, an ordinary-least-squares regression of precipitation extremes against surface temperature was computed. Lastly, the sensitivity for variability was expressed as a fraction of the time-mean precipitation extremes over the past reference period. To determine sensitivity for climate change, the time-series were averaged over the past and future reference time periods, the past value was subtracted to the future one and then normalized by twentieth century value and the difference in near-surface air temperature.
To calculate sea surface temperature from the surface temperature we applied the same land-sea mask already described in ECL section.

### ECB (from Borodina et al., 2017)

ECB correlates the annual maximum value of daily precipitation amounts (Rx1day index, Karl et al., 1999a) scaled with global-land temperature (Rx1day scaling), calculated over a past time period (1951–2014), to the same quantity calculated over a future period (2015–2099) in different regions of the world characterized by high climatological rainfall intensity. The scaling method in this case requires the calculation of the Theil-Sen slope (von Storch and Zwiers, 1984) of the relationship between the yearly time series of Rx1day and mean surface air tem-

perature, then normalized by space- and time-averaged Rx1day index. For the definition of the predictand, we chose the period 2015–2099 instead of 1951–2099 used by Borodina et al. (2017) in order not to include the window 1951–2014 over which the predictor is defined.
**Predictor**: annual maximum value of daily precipitation amounts (Rx1day) scaled with global-land temperature increase (Rx1day scaling), calculated over 1951–2014.
**Predictand**: same as the Predictor, but calculated over the period 2015–2099 in different regions of the world characterized by climatological high rainfall intensity.
The Rx1day index was calculated for each model on its native grid and then regridded over a regular 2.5°x2.5° grid, using a first order conservative remapping. A land-sea mask was applied to precipitation index and temperature data considering as land grid cells with at least 50% fractional land cover, as done in Borodina et al. (2017)
Climatological high-precipitation regions are identified applying a further mask which is built as follows. For each model, 1) by calculating the time mean Rx1day value over the period period 1951–1980 for each grid point and 2) by taking the 40% of the grid cells (excluding Antarctica) experiencing the highest rainfall intensity. One grid point is then selected to build the final mask if the criterion defined in item 2) above is satisfied for more than half of the models. The Rx1day and temperature time series are finally spatially-averaged over the regions selected with the mask.
Rx1day scaling was obtained as the regression slope of Rx1day and temperature, estimated with the non-parametric linear Theil-slope method (von Storch and Zwiers, 1984). The slope was then normalized by mean Rx1day temporally averaged over the past reference period.

## 2.4 Analysis

For each EC, a preliminary analysis has been performed to reproduce the results found in the reference papers using the same (or a very similar) set of models (from CMIP5) employed by the original authors (Thackeray et al., 2018; Li et al., 2017a; Borodina et al., 2017). This analysis produced successful results for each EC and will not be discussed. Table 2.3 summarizes the key characteristics of each EC that has been taken under consideration, as well as a short recap of the results obtained. Specifically, the first three columns detail, for each EC, the variables used as the predictor and predictand, along with

the time periods during which they were assessed. The results of the analysis, described in the subsequent subsections, are presented in the three rightmost columns. In the following subsections, we present in details the results of my analysis applied to the four ECs taken into consideration.

### 2.4.1 ECT

Even though the predictor contains information on the future climate and, as such, does not satisfy the proper definition of an EC, we decided to consider also this relationship in the context of Emergent Constraints. Figures 2.1a and 2.1b show, for CMIP5 and CMIP6

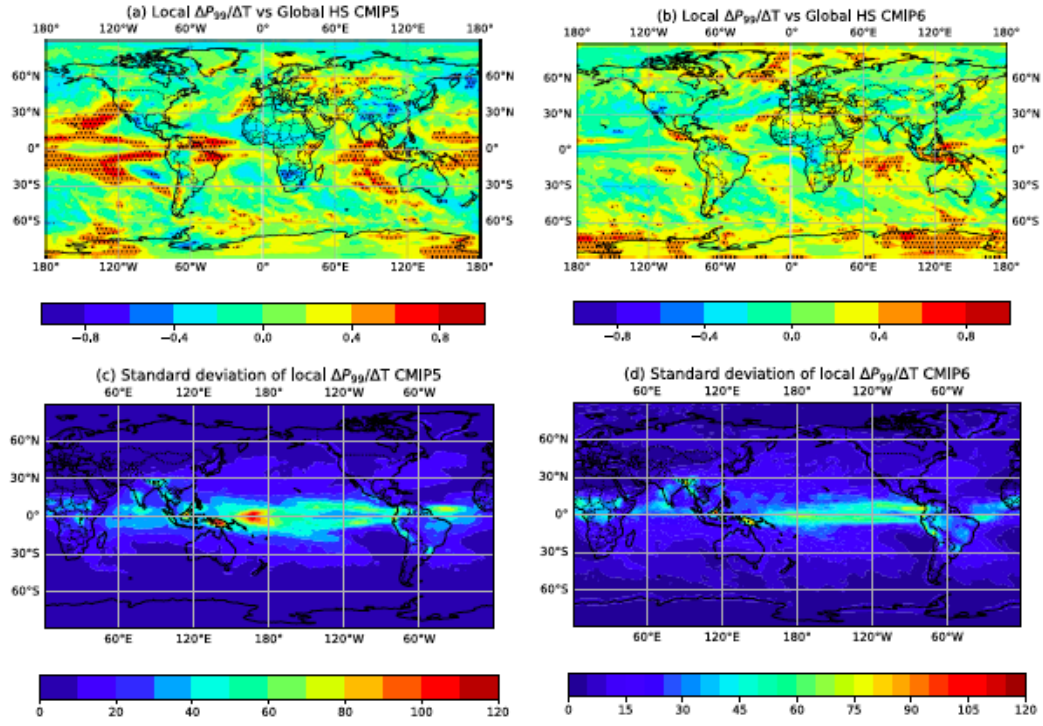


**Figure 2.1:** Analysis of ECT. (a) Inter-model correlation between the predictor (global-mean HS – [% $K^{-1}$]) and the predictand (local change in extreme precipitation per degree of global warming – [mm/year $K^{-1}$]) for CMIP5. Dotted areas show statistically-significant correlations ($p \leq 0.05$). (b) Same as (a) but for CMIP6. (c,d) Inter-model standard deviation of the predictand for CMIP5 (c) and CMIP6 (d).

respectively, the spatial map of the inter-model correlation between global-mean HS [% $K^{-1}$] and local changes in extreme precipitation ($\Delta P_{99}/\Delta T$ [mm/year $K^{-1}$]), respectively the predictor and the predictand in this EC. Dotted areas indicate where the correlation exceeds

**Table 2.3:** Summary of the ECs reconsidered in this study. The first four columns show, respectively, the EC acronym, the predictor and predictand definitions along with their reference periods, and the results discussed in the original papers in terms of correlation coefficients (all being statistically significant). The last two columns show our results (correlations coefficient, r, and p-value) obtained with CMIP5 and CMIP6 models.

| Acronym | Predictor | Predictand | Original result | CMIP5 | CMIP6 |
|---|---|---|---|---|---|
| ECT | Global-mean HS<br>[$\%K^{-1}$]<br>1960-1999 | $\Delta P_{99}/\Delta T$<br>[mm/year $K^{-1}$]<br>2060-2099 | r≥0.6 in oceanic<br>tropical regions<br>(CMIP5) | r≥0.6 with p<0.05<br>in oceanic<br>tropical regions | r≥0.6 with p<0.05<br>in southern tropical<br>Indian ocean |
| ECL | WP precipitation<br>[mm/day]<br>1980-2009 | ISM rainfall change<br>[mm/day °$C^{-1}$]<br>2070-2099 | r=0.63<br>(CMIP5) | r=0.56<br>p= $2 \cdot 10^{-3}$ | r=0.03<br>p=0.89 |
| ECG | Sensitivity for<br>variability<br>[$\%K^{-1}$]<br>1981-1999 | Sensitivity for<br>climate change<br>[$\%K^{-1}$]<br>2081-2099 | r=0.87<br>(CMIP3) | r=0.75<br>p= $8 \cdot 10^{-6}$ | r=0.73<br>p= $7 \cdot 10^{-6}$ |
| ECB | Rx1day scaling<br>historical<br>[$\%K^{-1}$]<br>1951-2014 | Rx1day scaling<br>future 8.5<br>[$\%K^{-1}$]<br>2015-2099 | r=0.82<br>(CMIP5) | r=0.88<br>p= $2 \cdot 10^{-9}$ | r=0.38<br>p=0.04 |

the 95% significance level ($p \leq 0.05$). Figure 2.1a, referring to CMIP5, shows that the areas with significant correlation are found around the Tropics, especially in the Pacific ocean, in the western Atlantic and coastal areas of Venezuela and Brazil, in the Indian ocean, and in Indonesia, in agreement with the results found by Thackeray et al. (2018). The same analysis performed with CMIP6 models is presented in panel b: in the Tropics, the correlation coefficient decreases considerably in all regions outlined above except in a small area in the Indian Ocean and around Indonesia, where $r \geq 0.6$. To better explore the reasons for this different behaviour in the two model ensembles, the inter-model standard deviation of the predictand for CMIP5 and CMIP6 models has been evaluated and is shown in Figs. 2.1c and 2.1d, respectively. CMIP6 models agree better with each other (smaller standard deviation) than CMIP5 models in projecting local extreme precipitation. On the other hand, global-mean HS does not change between CMIP5 (ensemble mean equal to $0.047 \pm 0.008$ $\%K^{-1}$) and CMIP6 ($0.046 \pm 0.009$ $\%K^{-1}$).

Our interpretation is that the reduced CMIP6 inter-model spread in the predictand prevents this relationship from still working as an EC, since the variability associated with a possible influence of the predictor can be smaller than the natural sample variability in the predictand.

### 2.4.2 ECL

Figure 2.2 shows the scatterplot between the predictor (mean western Pacific precipitation, [mm/day]) and the predictand (future change of ISM precipitation, [mm/day $^{\circ}C^{-1}$]) calculated with CMIP5 (panel a) and CMIP6 (panel b) models. Figure 2.2a shows that the two variables are positively correlated with a correlation coefficient of 0.56, not dissimilar to the one found by Li et al. (2017a), (i.e. 0.63, in Figure 2a of their original paper). For this specific EC, in order to check the sensitivity of the results to the ensemble composition, we performed a bootstrap test using a 27 sub-sample of a larger set of CMIP5 models (39 models overall, the extra ones from our set are reported in Table S1 in Appendix A). These 39 models are those for which precipitation data at monthly resolution were available – this specific EC in fact does not require daily precipitation data for its calculation, thus monthly precipitation data, available for a larger number of models, can be used to increase the size of our ensemble. The probability dis-

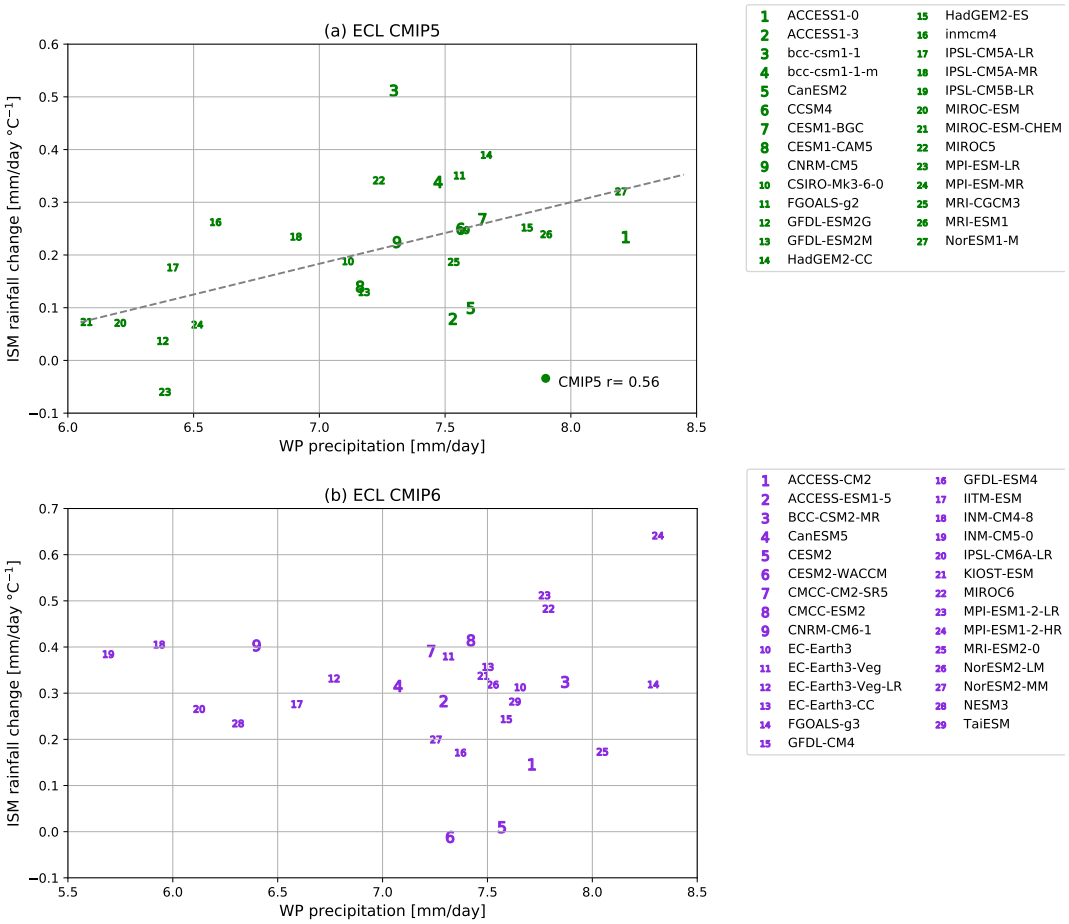


**Figure 2.2:** Analysis of ECL. (a) Scatterplot of the predictand (future change of ISM precipitation – [mm/day °C$^{-1}$]) against the predictor (western Pacific precipitation – [mm/day]) for CMIP5. The dashed line shows the ordinary least-squared best fit. (b) Same as (a) for CMIP6. Here the best-fit line is not shown as no significant correlation was found.

tribution obtained with this bootstrap analysis is shown in Figure 2.3 and exhibit a mean correlation coefficient of $0.35 \pm 0.10$, lower then the 0.56 obtained with the entire set of models. This result indicate that the correlation that supports this EC largely depends on the model ensemble composition; thus, this EC may not be particularly robust whenever the goal is to use it to reduce uncertainties in model projections. The corresponding coefficient of variation (CV), the ratio of the standard deviation to the mean, is around 29% denoting a quite high variability of the correlation coefficient as a function of the specific composition of the ensemble. The next step was to test the EC using CMIP6 models, as shown in panel b: in this case we found a correlation which drops dramatically to r=0.03 (p-value not significant),

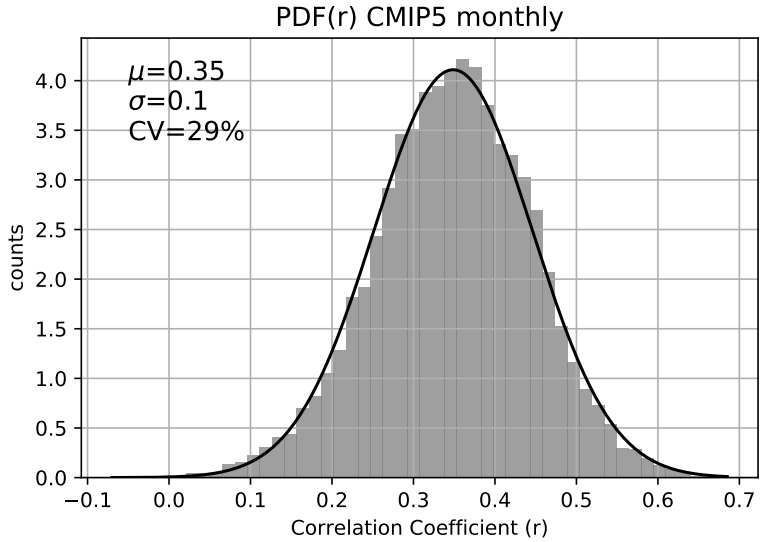


**Figure 2.3:** Probability distribution of the correlation coefficient for the bootstrap analysis of ECL (using monthly precipitation data from CMIP5 models).

confirming that this EC does not survive to changes in the model ensemble and in its composition.

Several attempts have been made to comprehend the lack of correlation in CMIP6 model ensemble. Among these, we conducted a more in-depth investigation into the climatic factors that are responsible of the EC definition. As explained by Li et al. (2017a), models that represent high present-day precipitation levels over the tropical western Pacific tend to project a more substantial increase in ISM rainfall. This is due to their excessive representation of a negative cloud-radiation feedback on sea surface temperature (SST). Inter-model differences in SST warming over the tropical western Pacific are a significant source of uncertainty in projections of changes in the Asian-Australian monsoon circulation and rainfall, particularly they have been found to be highly correlated (Chen and Zhou, 2015). On the other hand, warming of SST in the western Pacific is strongly attenuated by a negative cloud-radiation feedback that depends on the local mean cloud and precipitation levels (Lin, 2007; Meehl and Washington, 1996). An attempt to find a relevant correlation between the simulated tropical western Pacific precipitation and projected changes in SST warming patterns in the same area using CMIP6 models was done and is shown in Figure 2.4. No relevant and significant correlation was found (r=-0.04 with a p-value=0.85).

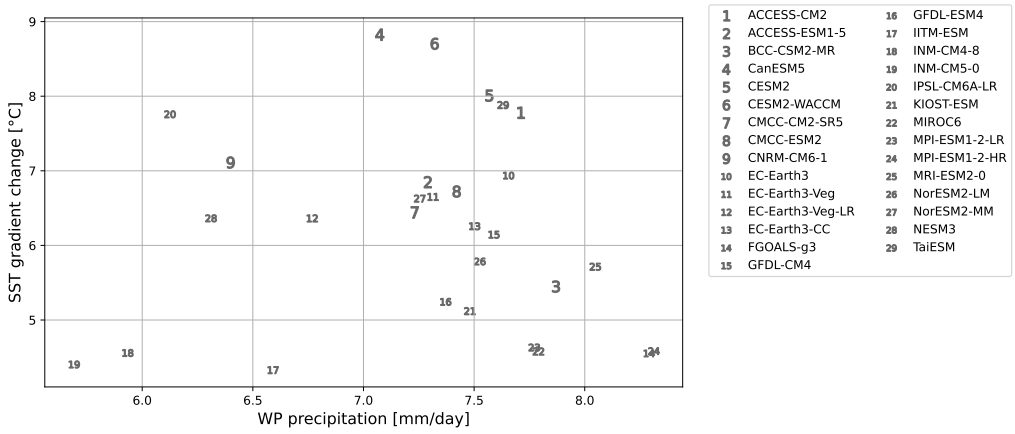


**Figure 2.4:** Scatterplot of SST gradient change in the western Pacific ocean [°C] and western Pacific present-day precipitation [mm/day]. The best-fit line is not shown as no significant correlation was found.

### 2.4.3 ECG

Figure 2.5 shows the scatterplot between the predictor (sensitivity for variability) and the predictand (sensitivity for climate change) for both CMIP5 (panel a) and CMIP6 (panel b) models. Models in the CMIP5 ensemble with high sensitivity for variability tend to project a larger increase in sensitivity for climate change, with an inter-model correlation of 0.75 ($p \leq 0.05$, see Table 2.3). In this case, since there are no more available models for both CMIP5 and CMIP6 than those specified in Tables 2.1 and 2.2 providing daily precipitation data required to calculate ECG, we performed a bootstrap analysis as described in the first part of this section, i.e., with sub-sets containing 2/3 of the models; results are shown in Figure 2.6. This analysis produced a distribution of the correlation coefficients with a standard deviation of 0.08 (mean value of 0.75). Similar results are found for CMIP6 models (panel b), with a correlation coefficient of 0.73 ($p \leq 0.05$, 0.73 $\pm$ 0.07 from the bootstrap analysis). In both CMIP5 and CMIP6 cases, the coefficient of variation, CV, is relatively low, 11% in CMIP5 and 9.6% in CMIP6, showing a low dispersion of the correlation coefficients obtained from bootstrap analysis with respect to their mean. This analysis suggests that this EC exists in both CMIP5 and CMIP6 and that it is characterised by a high and significant correlation coefficient between the predictor and the predictand.

To further test this EC robustness we replicated the previous analysis using the SSP245 CMIP6 emission scenario (Figure 2.7). The

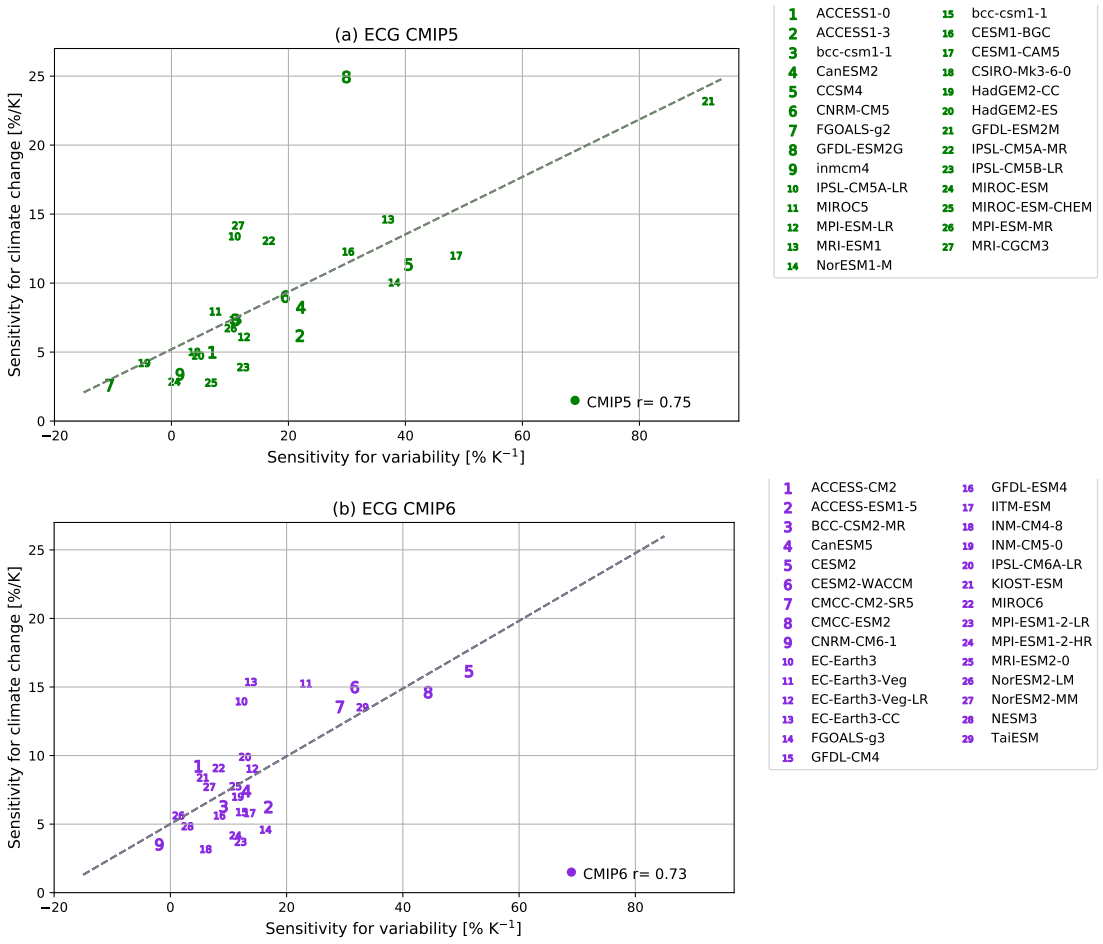


**Figure 2.5:** Analysis of ECG. (a) Scatterplot of the predictand (sensitivity for climate change) – [% K$^{-1}$]) against the predictor (sensitivity for variability – [% K$^{-1}$]) for CMIP5. The dashed line shows the ordinary least-squared best fit. (b) Same as (a) but for CMIP6.

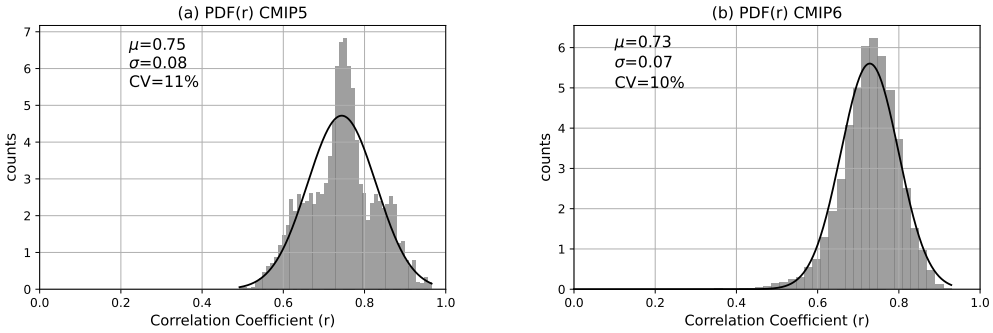


**Figure 2.6:** Probability distribution of the correlation coefficient obtained from the bootstrap analysis of ECG, using, respectively, CMIP5 (a) and CMIP6 (b) models.

results are consistent with those found for SSP585, resulting in a correlation coefficient of 0.85 ($p \leq 0.05$; $r = 0.84 \pm 0.07$ from the bootstrap

analysis), which provides evidence of the ECG robustness.

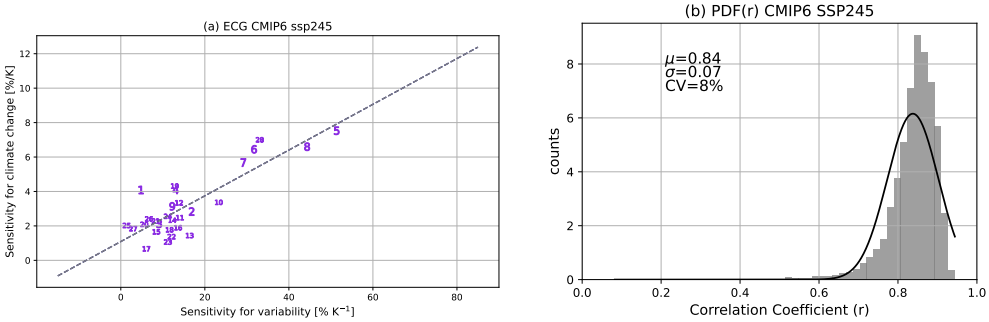


**Figure 2.7:** Analysis of ECG using the SSP245 scenario (CMIP6 models). (a) Scatterplot of the predictand (sensitivity for climate change) against the predictor (sensitivity for variability), to be compared with Figure 2.5 (panel b). (b) Probability distribution of the correlation coefficient from the bootstrap analysis, to be compared with Fig. 2.6 (panel b).

### 2.4.4 ECB

Figure 2.8 shows the scatterplot between the historical Rx1day scaling $[\%K^{-1}]$ (the predictor) and future projections of the same quantity (the predictand) with both CMIP5 (Figure 2.8a) and CMIP6 (Figure 2.8b). As can be seen in panel a, the correlation coefficient between the predictor and the predictand is high (0.88, p$\leq$0.05) and similar to the one found by Borodina et al. (2017) in the original paper (r=0.82). The bootstrap analysis performed on our CMIP5 ensemble led to an average correlation coefficient of $0.87 \pm 0.04$ and a CV of 5%, whose distribution is shown in Figure 2.9a, confirming the robustness of this relationship using CMIP5. Figure 2.8b presents the scatterplot computed with CMIP6 models: the correlation coefficient decreases as far as 0.38, with a p-value of 0.04. The bootstrap analysis led to a correlation coefficient probability distribution characterized by a standard deviation of 0.09 (mean value 0.38) and a CV of 24%, as shown in Figure 2.9b. In order to better understand the decrease of the correlation in CMIP6, global maps of inter-model standard deviation of the predictor and the predictand, for both CMIP5 and CMIP6, were calculated (see panels c-f of Fig. 2.8). For both the predictor and the predictand, the inter-model spread has clearly decreased in CMIP6 (panels d and f) with respect to CMIP5 (panels c and e). In particular, the regions showing the strongest reduction of the inter-model spread are India (for the predictor) and Africa and Southest Asia (for

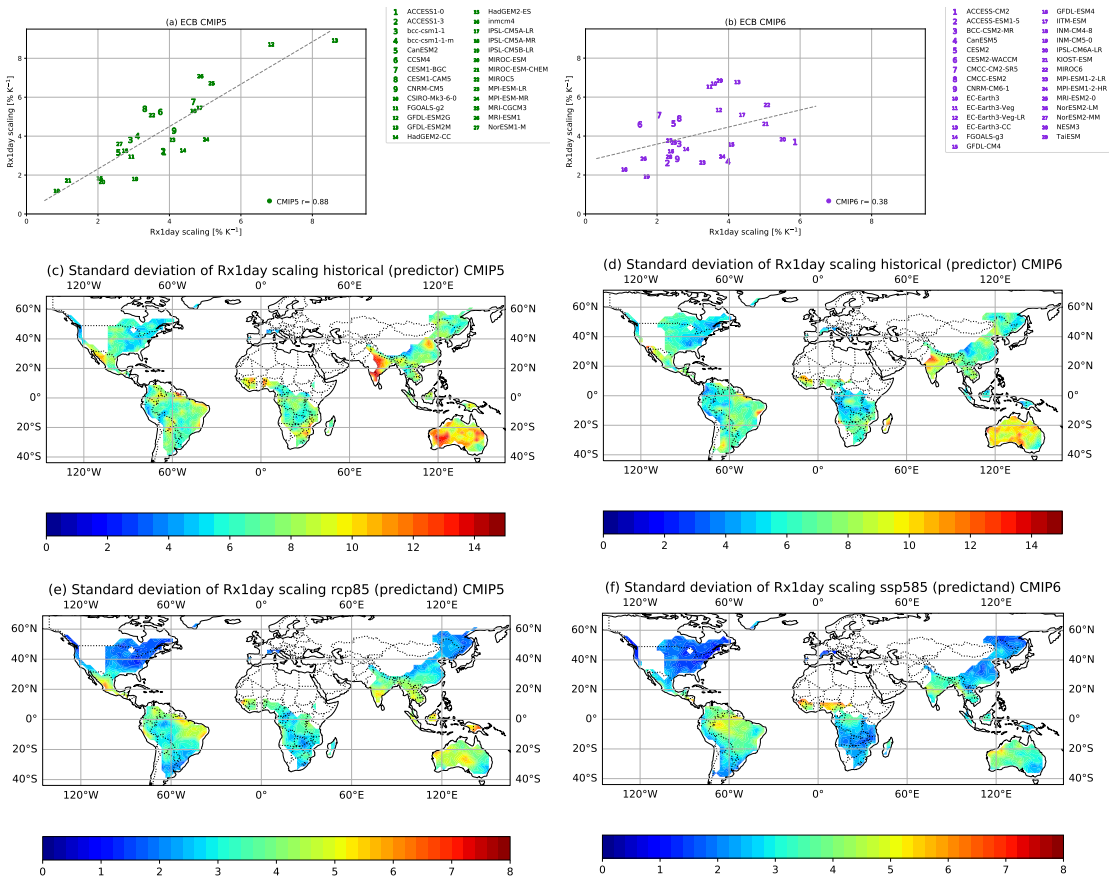


**Figure 2.8:** Analysis of ECB. (a) Scatterplot of the predictand (Rx1day scaling – [% $K^{-1}$]) against the predictor (Rx1day scaling – [% $K^{-1}$]) for CMIP5. The dashed line shows the ordinary least-squared best fit. (b) Same as (a) but for CMIP6. (c,d) Intermodel standard deviation of the predictor for CMIP5, CMIP6. (e,f) Intermodel standard deviation of the predictand (Rx1day scaling – [% $K^{-1}$]) for CMIP5,CMIP6.

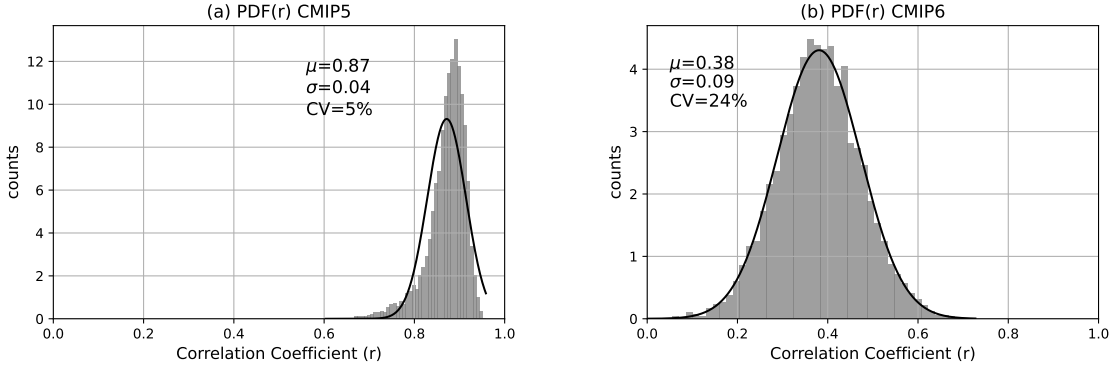


**Figure 2.9:** Probability distribution of the correlation coefficient for the bootstrap analysis of ECB, using, respectively, CMIP5 (a) and CMIP6 (b) models.

the predictand).

We also provide further details computing spatial maps of the inter-model correlation between the predictor and the predictand (Figure 2.10). They highlight the regions that most contribute to the decrease of the correlation coefficient describing ECB, namely India, Africa and Southest Asia, consistently with the previous finding. We hypothesize that spatial averaging performed over such diverse regions – inherent in the definition of this EC – may play a role in the decrease of the correlation in CMIP6. More generally, a reduction of the model uncertainty/spread in CMIP6 likely makes the application of this EC unnecessary to the aim of narrowing CMIP6 model projections.

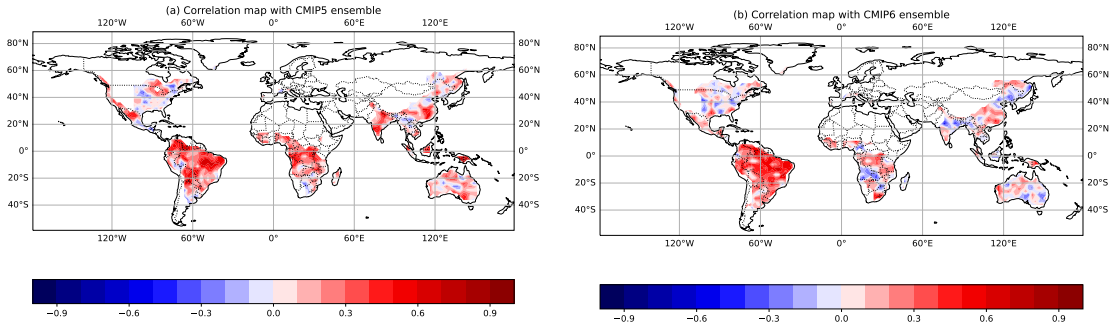


**Figure 2.10:** Map of inter-model correlation between predictor (Rx1day scaling) and predictand (Rx1day scaling) for CMIP5 (a) and CMIP6 (b) model ensemble.

## 2.5 Discussion

In this analysis, we have reconsidered the existence and the strength of four precipitation ECs already proposed in the literature and we have tested their sensitivity to the ensemble composition using different CMIP5 and CMIP6 model ensembles. Our analyses suggests that only one EC (ECG) is robust with both CMIP5 and CMIP6 models, another one (ECL) is not robust with either CMIP5 or CMIP6 and the two remaining ones (ECT and ECB) are robust with CMIP5 but not with CMIP6.

ECG analyses the relationship between tropical extreme precipitation (scaled with temperature increase over tropical oceans) during the past (a quantity which O' Gorman (2012) called Sensitivity for variability) and tropical extreme precipitation (difference between a

future and a past climatology) divided by temperature increase over the Tropics (called Sensitivity for climate change). As also suggested by O' Gorman (2012), who tested this EC in the CMIP3 ensemble, the strength of ECG arises from the fact that the predictor and the predictand are associated with the same physical process involved in precipitation formation (i.e. moist convection in the Tropics) which is included in the models by means of parameterizations. In the models, the latter are associated with similar inter-model spread in the response of tropical precipitation both in historical simulations (used to calculate the predictor) and in future projections (used to calculate the predictand). The sensitivity of ECG in CMIP6 was successfully tested not only for changes in the ensemble composition but also in different emission scenario, using both SSP245 and SSP585.

ECL establishes a relationship between western Pacific precipitation and the change in Indian Summer Monsoon rainfall, normalized by SST change. The physical process identified by the authors for this EC is related to the negative cloud-radiation feedback on sea surface temperatures: the negative feedback suppresses the local SST warming in the western Pacific area, strengthening ISM rainfall projections via atmospheric circulation. Our analysis does not lead to the same results as found in Li et al. (2017a) since we found a very low correlation both in CMIP5 and in CMIP6. In addition to the described ECL analysis, an attempt to find a relevant correlation between the simulated tropical western Pacific precipitation and projected changes in SST warming patterns in the same area was done using CMIP6 models but no relevant correlation was found (r=-0.04 with a p-value=0.85). This result suggests that the proposed atmospheric mechanism responsible for the relationship between the predictor and the predictand should be better and deeply investigated in climate models. For example, the study by Palazzi et al. (2014), analyzing precipitation patterns and climatologies in the Indian monsoon region in CMIP5, showed that GCMs including the indirect effect of atmospheric aerosol reproduce better the climatology of Indian monsoon precipitation than the models including the direct effect of aerosol particles only. The same was found for the models incorporating a fully-interactive aerosol module than those with prescribed aerosols. This suggests that aerosol particles and their interactions with clouds could be important factors to be considered in the relationship found by Li et al. (2017a) and, together with other factors, could be taken under consideration for

further analyses trying to better understand the links between the variables involved in this EC. As discussed in Section 2.1, several ECs were recently found to lack a satisfying physical basis able to sustain the correlation between the predictor and the predictand, and ECL may partially be ascribable to this category. The variables involved in this EC are probably too complex and a simple linear relationship that manages to both describe the EC and be used to narrow the model outputs can not be easily assessed.

ECT describes a relationship between global-mean precipitation change normalized by global-mean surface air temperature change and local changes in extreme precipitation normalised by global mean $\Delta$T. The physical mechanism behind this EC involves the relationship between the intensification of global hydrological cycle induced by global warming, changes in the atmospheric energy budget and increases in precipitation extremes. ECB correlates the annual maximum value of daily precipitation amounts scaled with global-land temperature increase in a past period to the same quantity calculated over a future period in different regions of the world characterized by high climatological rainfall intensity. Similarly to ECG, the formulation of this EC is based on the use of the same variable for the predictor (evaluated in a past period) and the predictand (evaluated in the future) and thus the relationship that underlies the EC is somewhat straightforward. In addition, there is no difference in the ability of the models to simulate the same variable in the past and in the future as the equations and parameterizations describing it are the same. In our analysis, both ECT and ECB turned out to be robust with CMIP5 – thus in agreement with the reference literature – but not with CMIP6. We hypothesize that this could be attributed to a reduction of the model uncertainty in the CMIP6 ensemble with respect to CMIP5, which does not make the application of these Emergent Constraints effective. In particular, we found that the inter-model spread in the projections of extreme precipitation ($99^{\text{th}}$ percentile for ECT, Rx1day for ECB) is considerably narrowed in the latest generation of climate models. For this, an EC or, more generally, a relationship between two precipitation-related variables found with CMIP5 models may not be robust or even exist in CMIP6. While the inter-model spread in CMIP6 is reduced compared to CMIP5, it is still large and still needs to be reduced in order to produce future projections useful for climate-change adaptation strategies.

A new precipitation EC assessed by Thackeray et al. (2022) constrains future changes in the occurrence of extreme precipitation with historical simulations of the same variable. As already noticed from our analysis, it seems considerably more favorable to use the same variable for the predictor and the predictand, or at least variables that are regulated in the models by means of the same parameterizations and which can be ascribed to the same physical mechanisms. This observation helps explaining why ECG is the only EC which survives in the CMIP6 ensemble – and the new study by Thackeray et al. (2022) corroborates this hypothesis. One might then wonder why ECB does not behave in the same way as ECG, given that both use the same variable in the past and in the future as the predictor and the predictand, respectively. One possible explanation was provided in Sect. 2.4.4 and we believe that it lies in the spatial aggregation inherent in the ECB definition. In fact, ECB correlates extreme precipitation in the past and in the future averaged in different regions of the world, characterized by climatological high rainfall intensity. The aggregated areas are very different to each other, since they belong to different latitudinal zones and they are subjected to different climatological regimes. Precipitation is then associated with diverse large-scale and local mechanisms and all this could affect the overall model performance in the past and in the future. In fact, we found considerable geographical differences in the inter-model spread in both the predictor and the predictand (Fig. 2.8 panels c-f) as well as in their correlation maps (Figure 2.10). This also suggests that current ECs may be limited in their geographic applicability.

Another important consideration is that the Equilibrium Climate Sensitivity (ECS) has been proven to exhibit substantial differences between CMIP5 and CMIP6, both in the mean value and in the inter-model variability (Zelinka et al., 2020). We considered the possibility that this difference, especially in the inter-model spread, may play a role in the robustness of ECs (in particular of ECT and ECB which show the major differences between the CMIP5 and CMIP6 ensembles). We think that the higher inter-model spread in ECS (in CMIP6) may introduce an additional source of uncertainty, thus reducing the signal (the correlation behind the ECs) to noise ratio. Besides influencing its robustness, the introduction of such an uncertainty makes it even more difficult to effectively use the EC technique to constrain

model uncertainties in projections.

Precipitation ECs are very powerful tools for understanding and investigating climate model response to mechanisms and dynamics linked to precipitation formation, trends and evolution. However, the analysis shown here suggests that their practical application for reducing uncertainties in model projections linking them to observable metrics should be regarded with caution, due to the large sensitivity of the EC to the model ensemble composition, which represents a weakness of the technique. In conclusion, as also suggested by Sanderson et al. (2021), the strength and potential of the EC technique should be mostly linked to its capability to interpret climate phenomena and to describe and investigate the connections between different climate variables – thus improving our knowledge of the climate system and its mechanisms, rather than only to its power to effectively narrow uncertainties in climate change projections. Exploring new emergent constraints and using them in new model ensembles thus represents a valuable way first and foremost to improve simulation of current climate and to better understand climate dynamics.

*Chapter* 3

# Elevation dependent change in ERA5 precipitation and its extremes

High elevation areas are attracting increasing attention of the scientific community: hot-spots, or sentinels, of climate change, mountains climatic equilibrium may be more rapidly altered compared to the globally-averaged signals. Climate change consequences can be anticipated or amplified at high elevation if compared to the adjacent low-land areas. In the last ten years, many studies have assessed that mountain warming rates are elevation-dependent. Elevation-dependent warming (EDW) - literally the stratification of warming rates with the elevation - has been observed in different mountain regions of the globe (Pepin et al., 2015), often with higher rates of warming at higher altitudes. Recent researches have revealed that EDW involves more than just temperature variations. Changes in climatic forcing have induced modifications in the atmosphere, surface energy distribution, convection, cloud cover, precipitation, and the entire water cycle. Therefore, it is more accurate to label this phenomenon as Elevation-dependent climate change (EDCC), which encompasses changes in boundary layer stability, energy, water, greenhouse gases, and aerosols exchange between the Earth and the atmosphere (Kuhn and Olefs, 2020). The term EDCC implies the concept that various climatic variables may exhibit a dependence with the altitude, with possibly greater impacts at higher elevations. Indeed, in mountainous regions, several variables, including circulation patterns, precipitation, and solar radiation regimes (Kittel et al., 2002), are significantly influenced by orography, contributing to notable uncertainty (Pepin et al., 2022). Understanding the precise impact of these processes on climate

variability and temporal changes in mountainous regions remains a research challenge.

Precipitation is a critical variable for mountain hydrological resources and its study is crucial under the context of climate change. Elevation is the primary factor that influence precipitation in mountainous regions. In fact, the complexity of the terrain can significantly influence local precipitation formation through orographic lifting of air masses, a phenomenon that facilitates condensation and cloud formation (Napoli et al., 2019). This effect leads to an increase in rainfall with the altitude, commonly referred to as the orographic enhancement of precipitation. Consequently, the analysis of altitudinal variations in precipitation changes becomes an interesting task, aimed at assessing whether the orographic precipitation enhancement is intensifying or decreasing over time. A recent study has assessed that when comparing mountains to low-lands, a greatly reduced orographic gradient in precipitation temporal trend was globally found in the recent past (Pepin et al., 2022). It has been highlighted a significant decrease at tropical and mid-latitudes in both hemispheres, although less clear results were encountered considering individual mountain regions. Despite this general behaviour, a simple comparison of precipitation trends at high elevation and low-lands might not well represent the actual complexity of Elevation-Dependent Precipitation Change (EDPC). Moreover, generalizing the EDPC by conducting a global comparison of orographic precipitation gradients, is highly challenging due to the lack of observations at high elevations.

The analysis of precipitation extremes within the context of climate change has been the focus of numerous studies, recognizing their potential impact on both human society and ecosystems (Chapter 4, SREX - IPCC Field et al., 2012). Understanding changes in precipitation extremes poses a significant research challenge. On the one hand, the scarcity of precipitation records may complicate the detection of long-term trends, especially for rare events. On the other hand, assessing and comprehending the overall effect requires simultaneous consideration of alterations in atmospheric dynamics, thermodynamics, and microphysics.

In mountain areas, the frequency of extreme precipitation events is usually increased due to the orographic uplift mechanism, convert-

ing atmospheric moisture into precipitation, and to the thermodynamic process that intensify extreme precipitation, as assessed by Clausius-Clapeyron relationship. Furthermore, dynamical processes and changes must be taken into account, as they can influence atmospheric circulation and other precipitation formation mechanisms, as well as the frequency of extreme events.

The aim of this chapter is to globally compare changes in long-term trends of mean and extreme precipitation occurrences within large mountainous areas, encompassing the Tibetan Plateau, Rocky Mountains, Greater Alpine Regions, and the Andes.

## 3.1 Data and Methods

We have analysed daily precipitation data provided by the fifth generation of the ECMWF reanalysis (ERA5), downloaded in october 2022 from the Copernicus Climate Change Service Climate Data Store (CDS). ERA5 is based on four-dimensional variational (4D-Var) data assimilation using Cycle 41r2 of the Integrated Forecasting System (IFS) providing records of the global atmosphere, land surface, and ocean waves. The ERA5 output is provided hourly at a 31 km horizontal resolution, then it has been summed to form the 24 hours to obtain daily precipitation totals and then interpolated on to a 0.25°x0.25° latitude-longitude regular grid. More information about the ERA5 dataset can be found in Hersbach et al. (2023).

Mean precipitation (Pm) and its variance together with a selection of indices from ETCCDI definition (Karl et al., 1999b), synthesised in the following list, were adopted in order to describe different aspects of rainfall.

1. **R10mm** Annual count of days when precipitation exceeds the threshold of 10 mm/day [Unit of measure: *days*]
2. **R20mm** Annual count of days when precipitation exceeds the threshold of 20 mm/day [Unit of measure: *days*]
3. **Rx1day** Annual maximum 1-day precipitation [Unit of measure: *mm/day*]
4. **R95p** Annual total precipitation exceeding the 95th percentile threshold on wet days evaluated over the 1961–1990 reference

period [Unite of measure: *mm/year*]

5. **CWD** Annual maximum length of wet spell: maximum number of consecutive rainy days [Unit of measure: *days*]

6. **CDD** Annual mximum length of dry spell: maximum number of consecutive dry days [Unit of measure: *days*]

Wherever needed, a wet day was assumed as a day with precipitation above 1 mm. Indices were calculated yearly for the period 1951–2020 at individual grid points.

The elevational dependency of precipitation changes was studied through complementary methodologies applied to the selected precipitation indices. At first, trends in precipitation indices over the period 1951–2020 were calculated for individual grid points within the study area. The existence of an EDPC was assessed using a linear regression analysis of the elevation distribution against trend values, testing its significance at 95% level. Additionally, we computed the reduced chi-squared analysis to determine whether a simple linear regression adequately describes the distribution's behavior. This analysis was complemented by an examination of geographical maps of trends to investigate the influence of different geographic factors.
As a second approach, study areas were divided into 500 meters high altitudinal bins, spatially averaging precipitation indices over each bin. The maximum altitude considered for binning was set requesting at least 10 grid points in each altitude bin. Temporal trends were evaluated with a linear regression over the period 1951–2020 for timeseries in each bin, accepting statistical significance at 95% confidence level. Trends were then compared at various altitude to identify positive (or negative) elevational dependency of change. For both methods, results at low land (0-500 meters) were used for comparison but not adopted in calculating vertical gradients.

Eventually, transects were extracted across mountain chains to discern the effects of elevation beyond geographical variability. Transects were considered either along the meridional or zonal direction, depending on the direction of the mountain chain, and built averaging three adjacent longitude (latitude) grid points across the transect. They were further used to differentiate West-East or South-North variations in the elevational dependency of the trends, due to the likely different climatic regimes affecting the two sides of the mountain chains (Toledo

et al., 2022).

## 3.2 Mountain areas

Elevational patterns of precipitation change were studied over four main mountain areas of the world, i.e. the Tibetan Plateau (TP, 60°–120°E; 18°–47°N), the Greater Alpine Region (GAR, 4°–19°E, 43°–49°N), the Rockies Mountains (RO, 235°–265°E, 30°–50°N) and the Andes, the latter subdivided into their tropical - Northern Andes (ANN, 280°–300°E, -23°–0°N) and mid-latitude parts – Southern Andes (ANS, 280°–300°E, -40°– -23°N). The study areas are identified in Figure 3.1 in terms of their climatological precipitation in boreal summer (panel a) and boreal winter (panel b) seasons. Besides being among the largest mountain regions in the world, the selected areas are representative of tropical and middle latitudes, monsoon and large-scale circulation influences, and a variety of regional influences. TP, GAR and RO are in the Northern mid-latitudes, all exposed to westerlies circulation, with the former largely affected by monsoon circulation, and the latter two by cyclonic activity and local summer convection. The Andes are in the summer tropics and mid-latitudes only marginally affected by westerly circulation, with most precipitation coming from the East. The Northern tropical part is reached by the ITCZ and the Southern part is exposed to an alternation of local dry winter and local wet summer. The RO and the AN share their preferential meridional orientation along the Pacific Ocean, whereas GAR and the Himalayas within the TP region have largely a zonal orientation. Further regional characteristics are discussed in the following sections.

### Tibetan Plateau

The orographical map (panel b) of the Tibetan Plateau (TP), along with elevation profiles from the three reference transects (panel a), is presented in Figure 3.2. Additionally, a geographical distribution map of the R10mm index averaged over the period 1951–2020 is provided to describe extreme precipitation patterns across the region (panel c). The TP, often referred to as the "Third Pole", stands as the world's largest and highest plateau, serving as the source of the majority of rivers that supply vital water resources to the population of South and East Asia (Immerzeel, 2020). In recent decades, the TP has un-

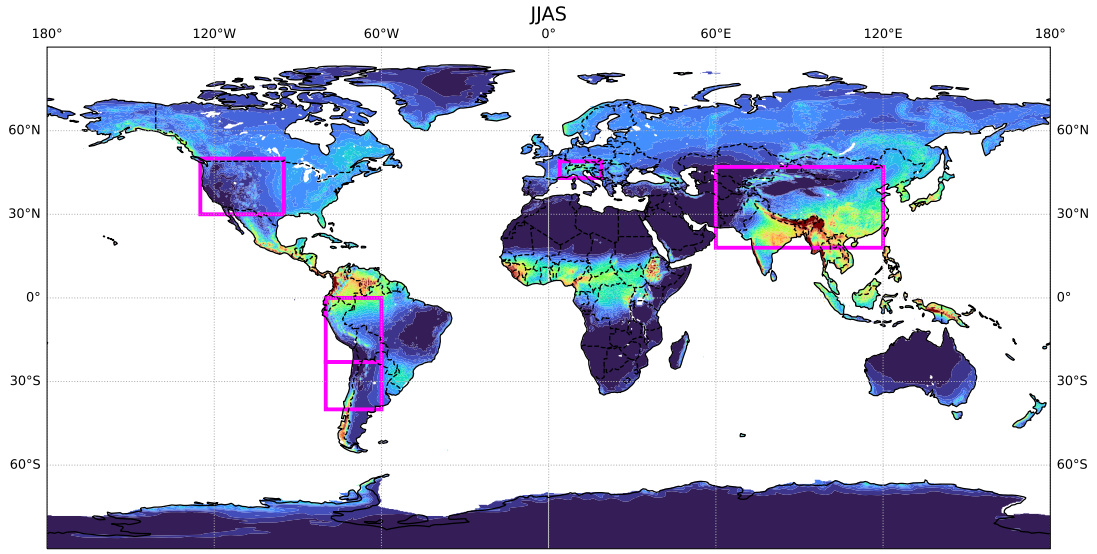


(a)

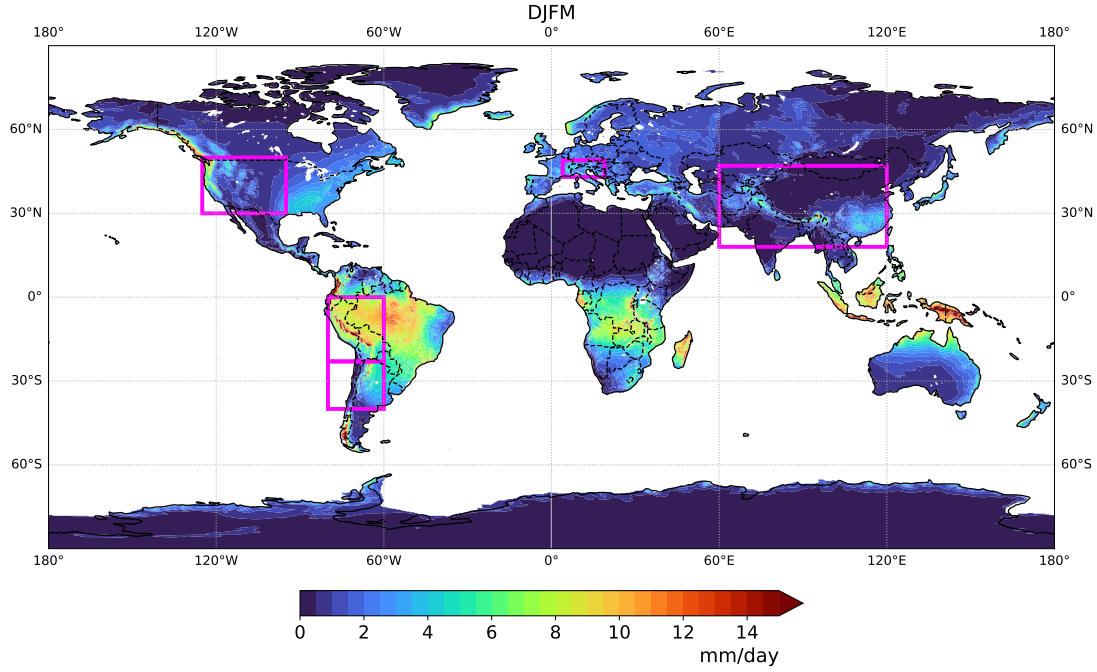


(b)

**Figure 3.1:** Definition of mountain areas selected for the study in terms of their climatological mean precipitation [*mm/days*] over the reference period 1951–2020

dergone significant warming (Bibi et al., 2018; Yao et al., 2016) and with temperature increase rates exhibiting an elevational-dependency, being more pronounced at higher compared to lower elevations (Liu

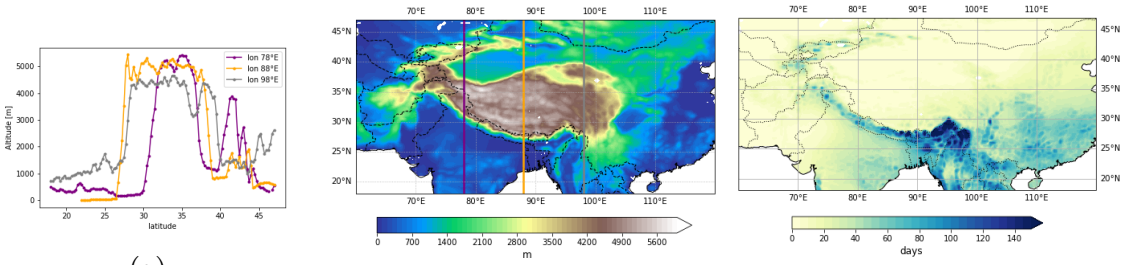


(a) (b) (c)

**Figure 3.2:** Orography [m] of the Tibetan Plateau region (a) with the elevation along three reference transects (b) and a map of the geographical distribution of extreme precipitation (R10mm index, *days*) evaluated over the 1951-2020 period (c)

et al., 2009). Furthermore, an increase in moisture content and precipitation across the TP has been observed (Yang et al., 2011). In this area, precipitation is characterised by large spatial variability, varying throughout different locations on the plateau (Bibi et al., 2018). In particular, two main sub-regions can be distinguished, depending on their exposure to the influence of different atmospheric circulation and patterns (Palazzi et al., 2013). The eastern Himalayan region receives the majority of precipitation and exhibits a peak in the number of intense rainy days, as illustrated in Figure 3.2(c). This pattern is primarily shaped by the dynamics of the monsoon: the northward movement of moisture from the Indian Ocean, driven by the southwest Indian monsoon causes a prevalence of rainfall occurring in the summer (see Figure 3.1a)(Li and Yanai, 1996). On the western side,in the Hindu-Kush Karakoram region, precipitation is observed mainly in the winter months (Figure 3.1b), primarily due to the influence of westerly winds that carry moisture from the Mediterranean and Caspian Sea (Singh and Kumar, 1995). For completeness, the maps of the seasonal climatology of R10mm are also shown in the Appendix B (Figure B.1).

## Greater Alpine Region

Figure 3.3 presents the orographical map of the Greater Alpine Region (GAR), elevation profiles along the three meridional reference transects, and the geographical distribution of the R10mm index over the period 1951–2020.

The GAR is a particularly interesting geographical area: one of the highest and largest European mountain chains, it is sensitive to

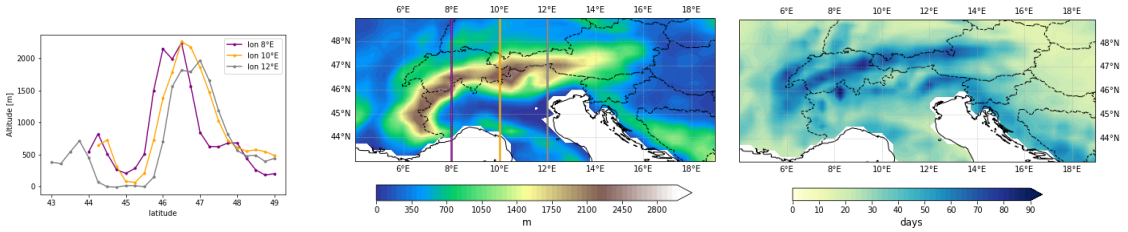


(a) (b) (c)

**Figure 3.3:** Orography [m] of the Greater Alpine region (a) with the elevation along three reference transects (b) and a map of the geographical distribution of extreme precipitation (R10mm index, *days*) evaluated over the 1951-2020 period (c)

different atmospheric synoptic regimes, mainly originating from the Atlantic or the Mediterranean sea. Precipitation patterns are influenced by several factors, including seasons and orography. These patterns exhibit substantial inter-annual variability and are also subject to the influence of larger atmospheric patterns, such as the North Atlantic Oscillation (NAO) or El Niño Souther Oscillation (ENSO). A comprehensive exploration of these regional climate characteristics can be found in the detailed study by Schär et al. (1998). The GAR is geographically positioned between two distinct climatic zones: the mid-latitude temperate climate and the Mediterranean climate type. Consequently, the alpine precipitation patterns exhibit notable spatial variations, both in terms of long-term average precipitation and intensity and frequency of extreme events. Nonetheless total precipitation generally tends to increase with increasing altitude, although the relationship between elevation and precipitation displays significant variability depending on location and season. Extreme precipitation also displays a dependence on altitude, reaching its maximum on the northern side of the mountain chain, as evident from Figure 3.3c. Furthermore, mean and extreme precipitation exhibits very similar geographical variability in the two selected seasons JJAS and DJFM, shown respectively in Figure 3.1 and Figure B.2 in the Appendix B. The northeast area shows a defined single peak during summer, whereas the northwest area experiences a second one, albeit weaker, during winter. The most intense precipitation is more prevalent during summer months, generally associated with convective weather systems (Schär et al., 1998).

## US Rockies Mountain

The figure 3.4 shows the orographical map of the US Rockies (RO) (panel b), elevation profiles along the three reference transects (panel a), and the geographical variability of R10mm within the region (panel c). These maps illustrate the considerable spatial variability of ex-

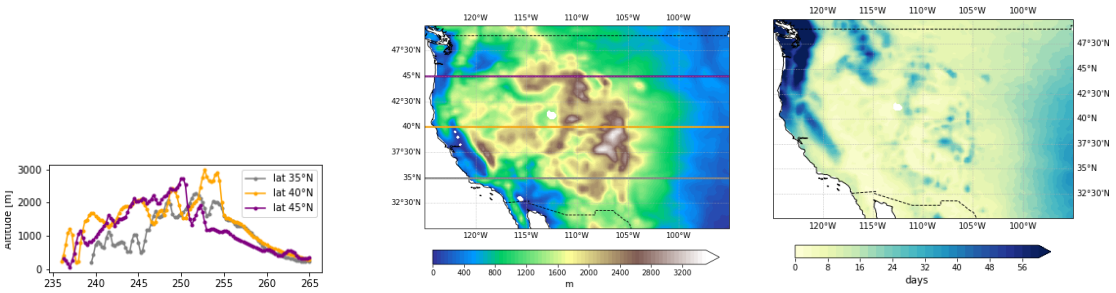


(a) (b) (c)

**Figure 3.4:** Orography [m] of the US Rockies Mountains (a) with the elevation along three reference transects (b) and a map of the geographical distribution of extreme precipitation (R10mm index, *days*) evaluated over the 1951-2020 period (c)

treme precipitation in the area. The highest R10mm values are observed in the northern coastal area, influenced by the influx of cool and moist air from the northern Pacific Ocean. Moreover, comparing panels (b) and (c), it becomes evident that the distribution of precipitation in the region is significantly influenced by its mountainous terrain. The orography gives rise to a classic orographic precipitation pattern, characterized by enhanced rainfall on the windward side and a rain shadow on the lee side (Kittel et al., 2002). This effect is maximised in the winter seasons, showing very similar pattern to the one shown by annual R10mm (compare Figures 3.4c and Figure B.3 in Appendix B). On the eastern side of the area, precipitation is caused by the collision of continental polar air masses and warmer maritime tropical moist air. During summer, the northern coastal areas continue to be influenced by moist Pacific air, showing a second peak of intense precipitation, whereas the south-west of the RO experiences dry condition due to the impact of dry continental air and monsoonal flows from the Gulf of Mexico and California (Kittel et al., 2002), as observable in Figure B.3.

## Andes

Figure 3.5 presents the orography of the Andes (AN) (panel a), together with the map of the geographical distribution of R10mm (panel b). The AN represents the predominant topographical feature of

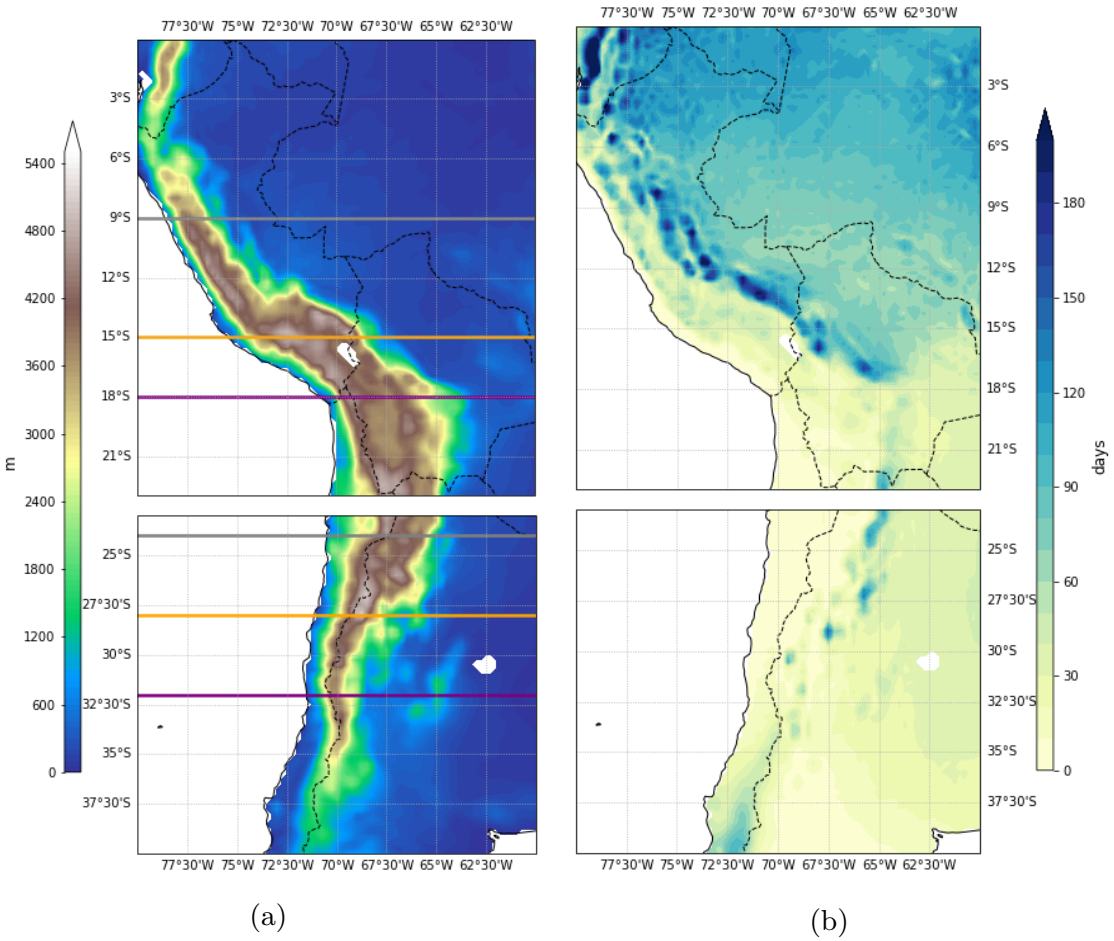


**Figure 3.5:** Orography [m] of the Andes both Tropical and Sub-tropical (a) and a map of the geographical distribution of extreme precipitation (R10mm index, *days*) evaluated over the 1951-2020 period (b)

South America, stretching 7000 kilometers, from the Tropics to mid-latitudes. Precipitation exhibits high spatial variability; consequently, the region has been divided into two distinct areas: the Tropical Andes (ANN), characterized by higher precipitation, and the Subtropical Andes (ANS), marked by drier conditions, as done in Toledo et al. (2022). The ANN serve as a natural barrier separating the persistently humid Amazon Basin to the east from the arid Pacific coast to the west. This distinction can be noticed also in extreme precipitation patterns,

as shown in Figure 3.5c. Climate in this region can be characterized by relatively dry conditions in austral winter season (JJAS), and wet conditions during the austral summer (DJFM) (see Figure 3.1 for Pm, and Figure B.4 in Appendix B, for R10mm). During the central austral winter months (June-August) in fact, the subtropical jet stream reaches its northernmost position, creating a block for the moisture transport from the Amazon region, leading to a dry climate (Potter et al., 2023). During austral summer, the jet stream weakens and shifts southward allowing the eastern side of the Cordillera to serve as a convergence point for atmospheric moisture originating from both the Intertropical Convergence Zone (ITCZ) and the South American Monsoon System (SAMS), causing extremely wet conditions, with the most intense rainfall concentrated near the summit of the chain (Caicedo et al., 2020), as can be notice in Figure 3.5c.
The ANS exhibits a distinct seasonal geographical pattern. Specifically, during the local winter season, the ANS (below 30°S) features a dry east side and a wet west side of the chain. This is attributed to a predominant atmospheric moisture source originating from the evaporation over the Pacific Ocean (refer to Figure B.4 in Appendix B). In contrast, during the local summer (DJFM), precipitation in the ANS concentrates on the eastern side of the chain, while the western side experiences minimal rainfall.

## 3.3 Results

### 3.3.1 Elevational dependency

The elevational dependency of trends in mean precipitation and extreme precipitation indices has been evaluated with the two complementary methods described in section 3.1. Table 3.1 summarises the results obtained evaluating the value of the altitudinal gradient, computed as the linear regression of the distribution of elevations versus trend values of all grid points in the study regions. In the TP, the GAR and the ANS, a significant positive altitudinal gradient is observed in both the mean and extreme precipitation trends. On the contrary, the RO exhibit an opposing sign, with consistent negative vertical gradients in the trends of all indices but CDD. The ANN shows no clear pattern. The chi-squared analysis suggests that for TP and ANS, a simple linear regression may not be the most appropriate method to describe the altitudinal stratification, as a more complex pattern may

**Table 3.1:** Summary of the elevational dependency of ERA5 precipitation indices over the 5 target regions Tibetan Plateau (TP), Greater Alpine Region (GAR), Rockies (RO) and Andes split in Northern part (ANN) and Southern part (ANS). Orange (blue) colour refers to 95% significance positive (negative) altitudinal gradient. Asterisk means acceptable reduced chi squared analysis. Empty cells indicate no clear and significant behaviour.

| | Pm | R10mm | R20mm | Rx1day | R95p | CWD | CDD |
|---|---|---|---|---|---|---|---|
| TP | | | | | | | |
| GAR | * | * | | | | * | |
| RO | * | * | * | * | * | * | * |
| ANN | | | | | | | |
| ANS | | | | * | | | |

be hidden. Remarkably, each mountain region consistently shows similar behavior in terms of the vertical gradient of changes in all indices, except for consecutive dry days (CDD), which switches to the opposite gradient in both the ANS and RO. Another exception is represented by the GAR, where only mean precipitation (Pm), extreme precipitation (R10mm), and the maximum yearly duration of consecutive wet days (CWD) exhibit the same EDPC signal.

It is important to acknowledge that the information derived from this analytical method has limitations. In fact, a positive (or negative) gradient can be the result of various phenomena occurring at both high and low elevations. For example, a positive altitudinal gradient in precipitation indices can be attributed to one of several scenarios: a more pronounced increase in precipitation trends (wetting) at higher elevations compared to lower ones, a more significant reduction in precipitation trends (drying) at lower elevation compared to higher ones, or a contrast between wetter conditions at higher altitudes and drier conditions at lower altitudes. Therefore, the adoption of an additional methodology becomes essential. The study areas were therefore subdivided into altitudinal bins of 500 meters, and temporal trends computed, considering also their related errors and the statistical significance (p-value) to construct a comprehensive vertical profile. Additional insights into the unique characteristics of each mountain region are detailed in subsequent sections.

For completeness, Table 3.2 represents the altitudinal gradient of long-term climatological mean and extreme precipitation indices, analogous to Table 3.1. It is evident that all regions, except for the GAR, exhibit a significant negative gradient with elevation, indicating a decrease in

precipitation with increasing altitudes. The chi-squared test reveals that these elevational gradients can not be represented by a simple linear regression, suggesting a high spatial variability as well as the importance of examining the binned vertical profile, as explained for the altitudinal gradient of indices temporal trends. On the contrary, the GAR shows an enhancement of precipitation with the elevation, well represented by a significant linear regression for many indices. A more detailed description of the vertical profile of climatological mean and extreme precipitation indices is reported in Appendix B.2.

**Table 3.2:** Summary of the elevational dependency of the climatological mean of ERA5 precipitation indices for the reference period 1951–2020 over the 5 target regions Tibetan Plateau (TP), Greater Alpine Region (GAR), Rockies (RO) and Andes split in Northern part (ANN) and Southern part (ANS). Orange (blue) colour refers to 95% significance positive (negative) altitudinal gradient. Asterisk means acceptable reduced chi squared analysis. Empty cells indicate no clear and significant behaviour.

| | Pm | R10mm | R20mm | Rx1day | R95p | CWD | CDD |
|---|---|---|---|---|---|---|---|
| TP | | | | | | | |
| GAR | | | | * | * | * | * |
| RO | | | * | * | * | * | |
| ANN | | | | | | | |
| ANS | | | | | | | |

## Tibetan Plateau

Figure 3.6 reports the details of the vertical profile of temporal trends of spatially averaged binned data superimposed to the distribution of trends of individual grid points over the region. Most individual trends tend to cluster, leading to largely compact distributions, especially at high altitude where the number of points is smaller, and the influence of the ground is damped. Deviations from the core of the distribution occur more pronouncedly towards smaller values of the indices below 2000 meters and towards higher values above, contributing to increasing the steepness of the vertical gradient and a larger positive change in extreme precipitation at higher elevation. As summarized in Table 3.1, all indices in the Tibetan Plateau show an overall positive vertical gradient of temporal trends over the 1951–2020 period, except for CDD. Pm (panel a), R10 (panel b), and CWD (panel c) exhibit a consistent behavior: profiles shows a positive gradient up to

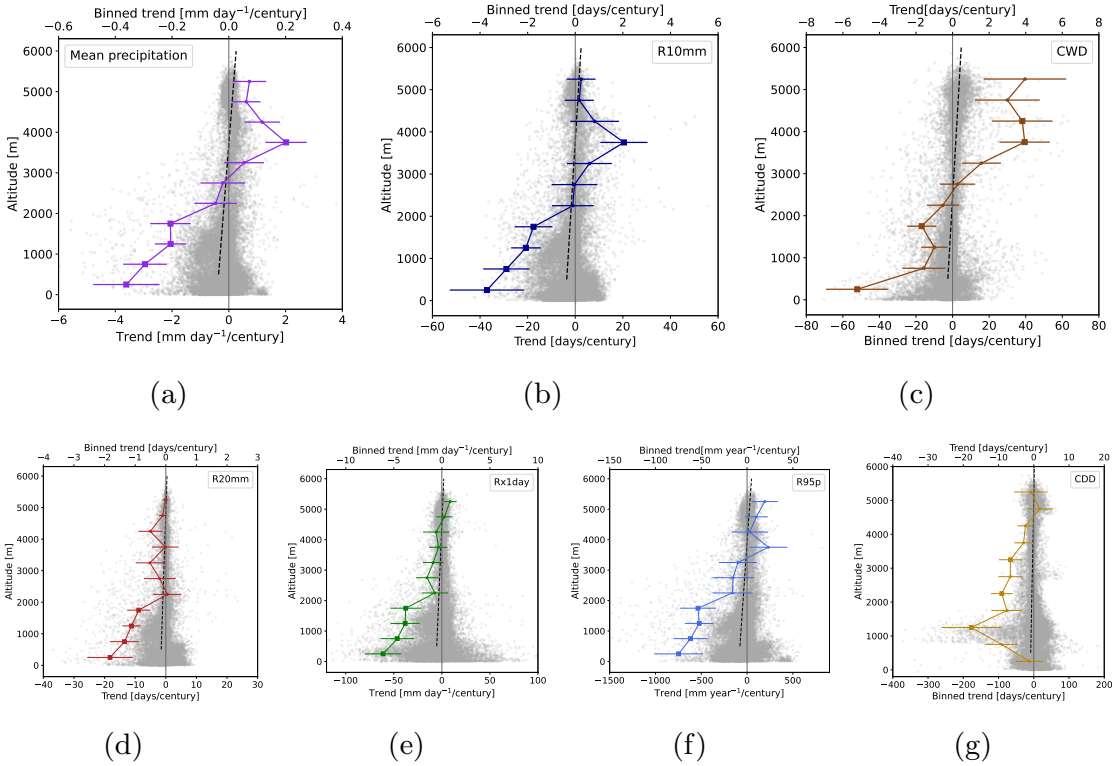


**Figure 3.6:** Elevational dependence of temporal trends of precipitation indices (see labels). Each panel shows the vertical profile of spatially averaged binned data (top scale) superimposed to the distribution of trends of individual grid points (grey, bottom scale) over the Tibetan Plateau. Vertical profiles include errors on the trend and the significance of the trend (filled squares when $\geq$95%). Point distributions are accompanied by their linear regression (dashed line). Note that the scale for vertical profiles is magnified by a factor 10.

4000 meters, where an inversion occurs. Significantly negative trend values at altitudes below 2000 meters indicate a drying effect that diminishes with the elevation. On the contrary, the significant positive trend around 4000 meters indicates increased wetting effects at very high altitudes. R20mm (panel d), Rx1day (panel e), and R95p (panel f) show an overall positive gradient with altitude, with a change in the slope around 2000 meters. As described for the other indices, the significant negative trends below this threshold indicate a drying signal at low elevations, which decreases with altitude. CDD has a broad distribution between 500 and 2000 meters due to the presence of microclimatic areas (e.g. the Taklamakan Desert). Above this altitudinal threshold, CDD is characterized by an overall positive gradient with the altitude and significant negative trends around mid-altitudes, indicating a lower persistence of drought conditions. The

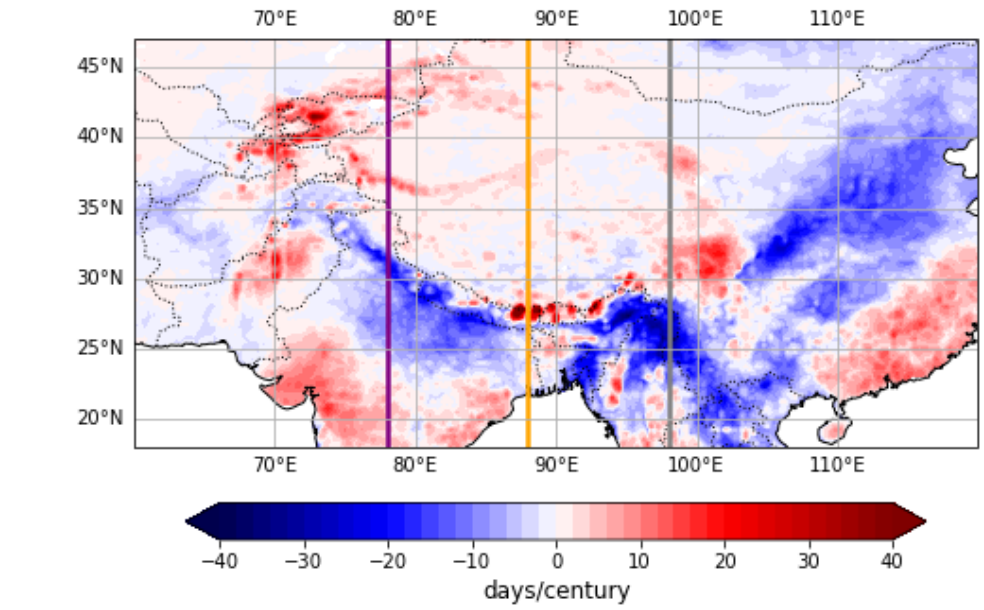


(a)

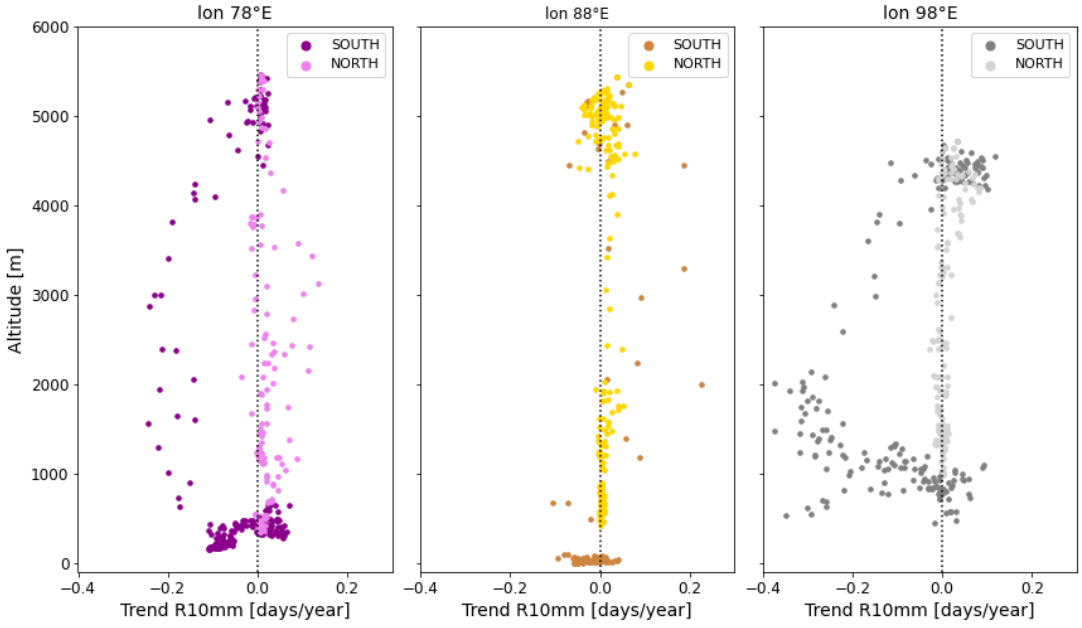


(b)

**Figure 3.7:** Geographical distribution of trends in extreme precipitation (R10mm) over the 1951-2020 period (left) and their elevational distribution (right) along the three meridional transects defined in Figure 3.2 and reported on the map as colour-coded vertical lines. Grid points were separated in Northern and Southern parts assuming the maximum altitude along the transect as separator.

impact of geographical variability was investigated by inspecting maps of trends and the elevational dependency (see Figure 3.7) along the three meridional transects already described in Figure 3.2. Transects clearly reveal how geographical differences impact on the vertical distributions: the northern region demonstrates limited altitudinal stratification, whereas the southern area displays a knee-shaped gradient. Precipitation decreases progressively up to 2000 meters; at this level an inversion occurs and negative trends increases toward zero. Furthermore, the 98° latitude transect highlights the high-altitude wetting effect also found in the vertical profile of binned data (Figure 3.6).

## Greater Alpine Region

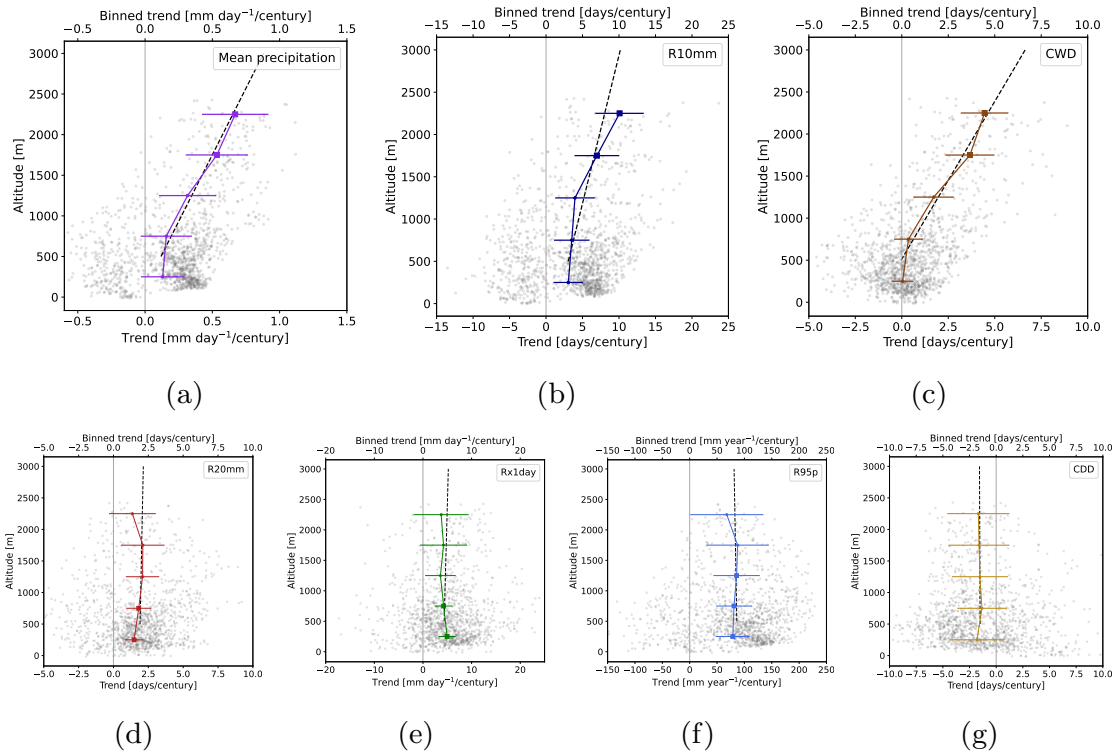


**Figure 3.8:** As in Figure 3.6 but for the GAR.

Figure 3.8 describes the vertical profile of indices trend over the GAR, in terms of both binned data and the overall grid-points distribution. Pm (panel a) R10mm (panel b) and CWD (panel c) show distinct linear positive vertical gradients, both in the distributions and in the vertical profiles. They indicate an enhancement of precipitation trend with altitude and consequently a significant wetting signal

at high altitudes (above 1000 meters). The other indices show no altitudinal stratification. An investigation of the R10mm trend map and

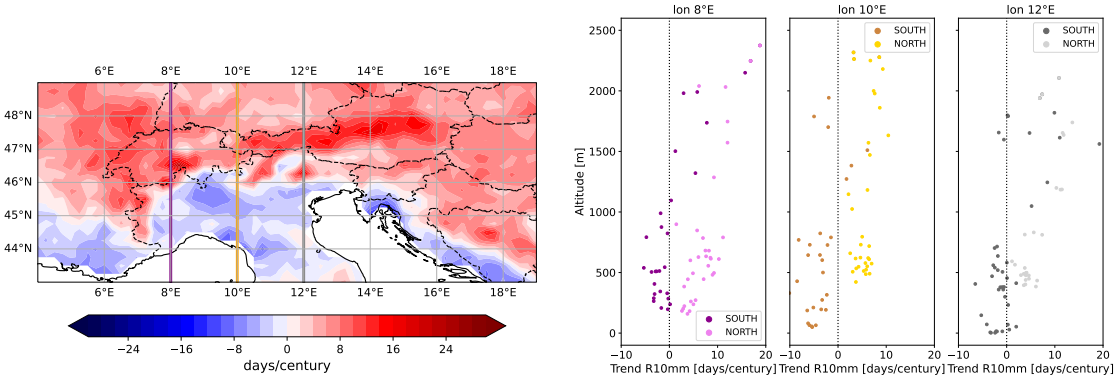


(a) (b)

**Figure 3.9:** Geographical distribution of trends in extreme precipitation (R10mm) over the 1951-2020 period (a) and their elevational distribution (b) along the three meridional transects reported on the map as colour-coded vertical lines. Grid points were separated in Northern and Southern parts assuming the maximum altitude along the transect as separator.

the vertical profile of the three meridional transects was performed (Figure 3.9). An evident discontinuity can be seen between positive trends in the northern side and negative trends in the southern side of the region. Even though this difference leads to a bias between the southern and northern branches of the distribution of trends along the transects, the altitudinal-gradient of the two distribution exhibit the same sign. The positive elevation dependency in the GAR seems to be therefore independent on geographical variations.

## US Rockies

The RO mountains show an opposite sign of the vertical gradient, both in the distributions and in the vertical profiles (Figure 3.10). Once again, Pm (panel a), R10mm (panel b) and CWD (panel c) show the most convincing elevational dependency, with increasingly larger reductions at higher elevation, confirming the enhanced drying at higher altitudes obtained with first method. The same pattern is observed in the other indices, with the exception of CDD which exhibits an opposing gradient, even though no significant trends can be observed in the binned data. All indices (except CWD) are characterized by a broad and inhomogeneous distribution, presenting a negative

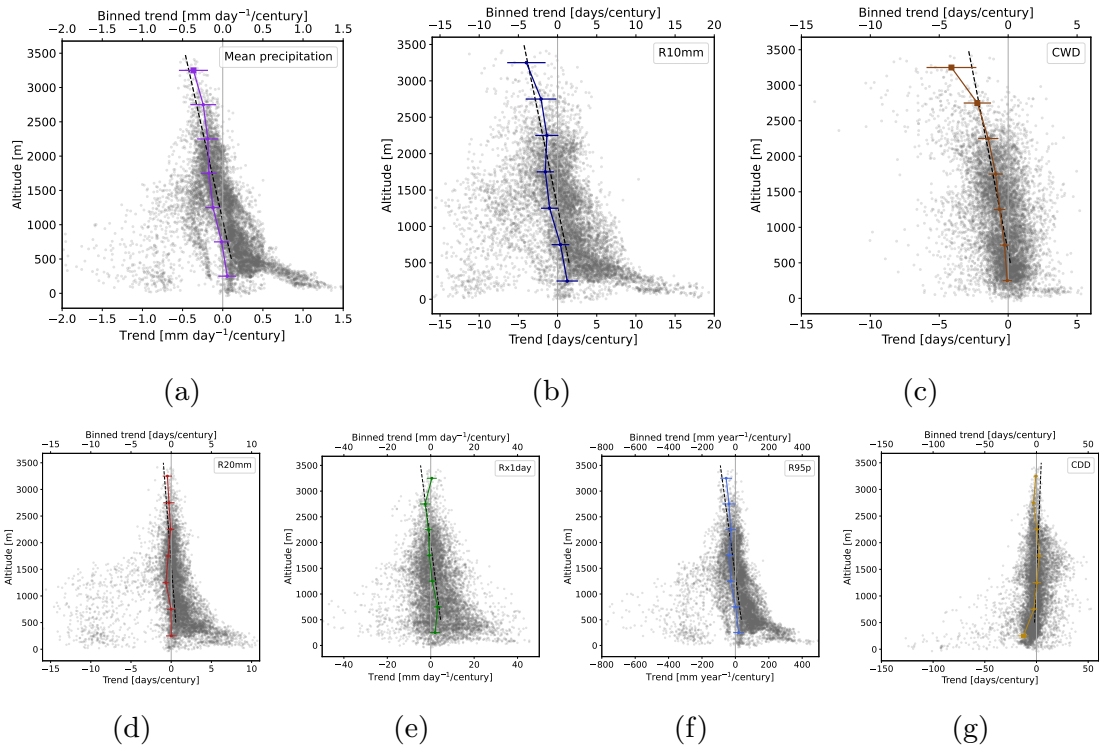


**Figure 3.10:** As in Figure 3.6 but for the RO.

tail below 2000 meters. This deviation from the compact bulk of the distributions was interpreted by inspecting the geographical variability of the region (Figure 3.11, transect at 45°N). In fact, the northern coastal area, characterized by low altitudes, has experimented a strong reduction in both mean and extreme precipitation, leading to such broadness of the distribution. Figure 3.11 also shows the vertical

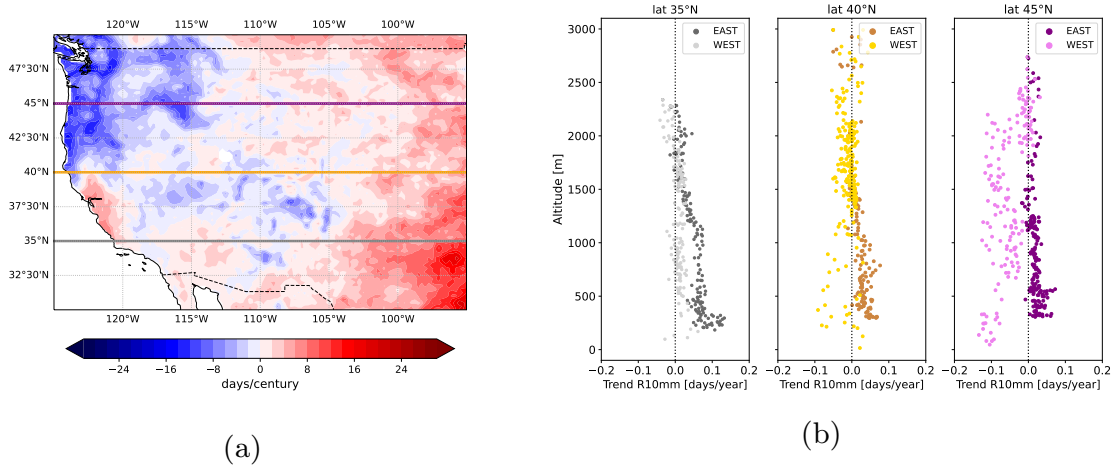


**Figure 3.11:** As in Figure 3.9 but for the RO.

profile of the three zonal transects described in section 3.2. They exhibit two very distinct patterns up to 1500 to 2500 meters depending on latitude, with much lower values in the western slopes. Such biases affect vertical gradients together with a large contribution to the variance and branching in the overall distributions. The elevational distribution shows a clearly different behavior separating the western and the eastern side of the chain, especially at low and mid-elevation. The two sides reconcile shifting to higher elevation.

## Andes

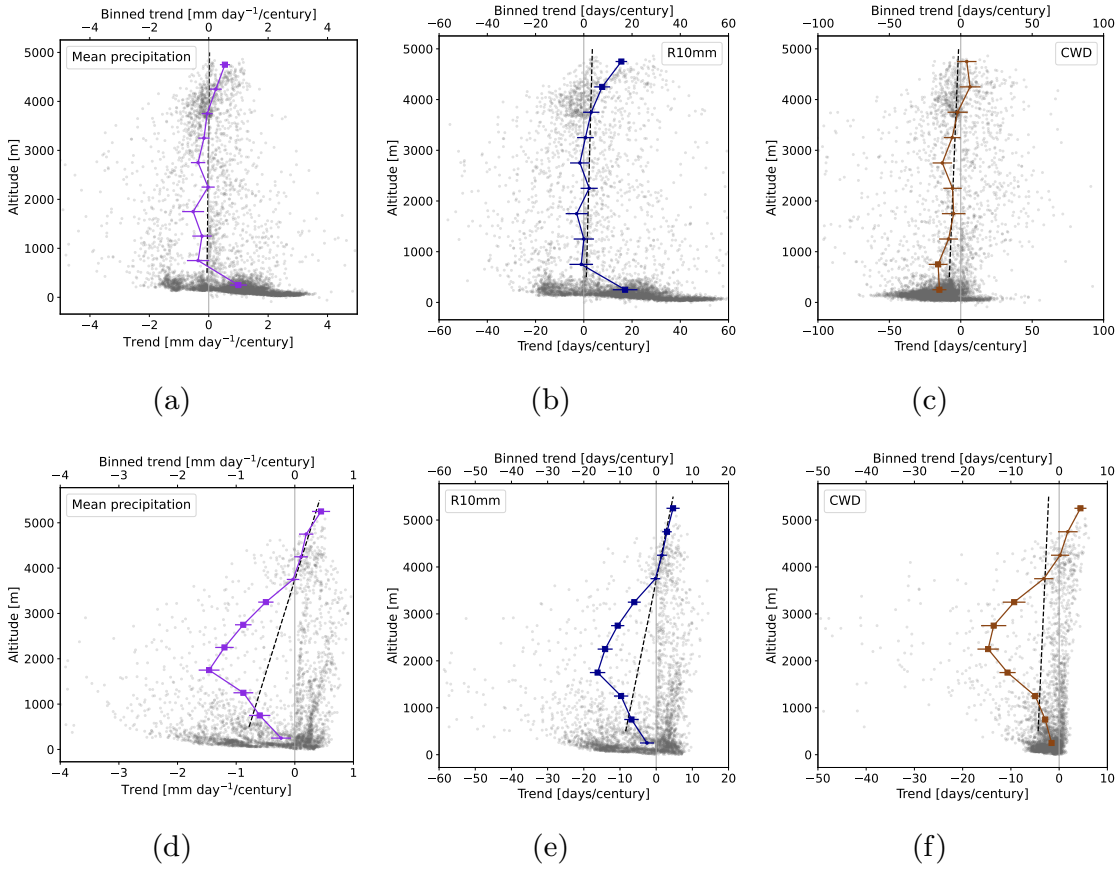


**Figure 3.12:** As in Figure 3.6 but for the Andes tropical (ANN) (above) and sub-tropical (ANS) (below).

Figure 3.12 shows the vertical profile of the binned data analysis over the Andes, both tropical and subtropical, for Pm (panel a,d), R10mm (panel b,e) and CWD (panel c,f). As for the other mountain areas, Pm, R10mm and CWD consistently exhibit similar patterns among themselves and align with the other indices shown in Figures

B.10 and B.11 in Appendix B. Two clearly distinct behaviors can be observed in the Tropical and sub-tropical regions. Generally, the ANN seem to have no altitudinal stratification while the ANS profile shows a more complex dependency with the elevation. The latter is characterized by two different gradients with opposite sign, showing a knee-type curve with an inversion around 2000 meters. Below 4000 meters, the ANS profile is characterized by negative trends, revealing a drying effect in both mean and extreme precipitation. This confirms the first method analysis: a simple linear regression might not be sufficient to describe the real altitudinal dependency. Nevertheless, the ANN and the ANS share certain common characteristics. Primarily, above 4000 meters, both regions exhibit a positive altitudinal gradient with positive trends, highlighting a wetting phenomenon occurring at very high altitudes, similarly to what has been observed in the TP and GAR regions. Furthermore, both distributions are notably broad, particularly at mid and low altitudes, making necessary an examination of trend geographical variability within the area. Taking into account the driving mechanisms of rainfall, it is crucial to examine the western and eastern sides of the mountain chain separately. In this case, performing a zonal transect analysis is not convenient owing to the narrow width of the Andes mountain chain resulting in a limited number of grid points within a single transect. Consequently, the entire area has been considered averaging the eastern and western side of the chain separately.

In Figure 3.13, the vertical profile of binned data of R10mm is shown, dividing the western and the eastern side of the chain. The broadness of the overall distribution, shown in Figure 3.12 (panel a and e), can be ascribed to the significant disparities in altitudinal profiles of trends between the eastern and western side of the mountain chain. The west side has a similar profile in both tropical and sub-tropical Andes: trends are positive, showing significant enhanced precipitation changes at high altitudes. The overall profiles show a positive altitudinal gradient for the ANN while no significant signal can be assessed in the ANS. On the contrary, the eastern side of the ANN has no significant vertical gradient and above 4000 meters its behaviour become consistent with the eastern side. In the ANS, the overall profile is driven by the eastern side, which shows the peculiar knee-shape at mid-altitude shown in Figure 3.12 (panel d, e and f).

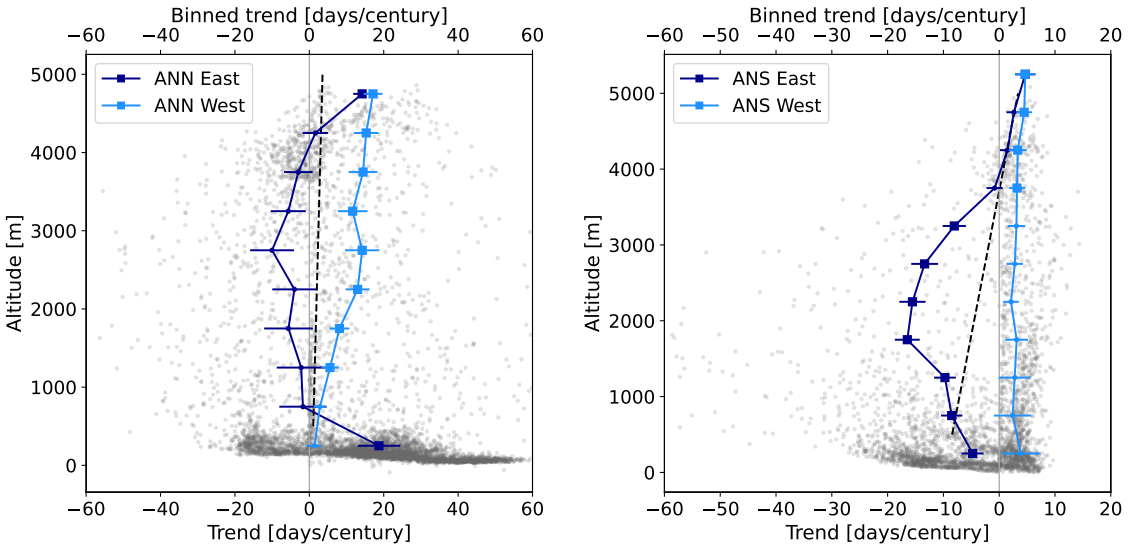


(a) (b)

**Figure 3.13:** Elevational dependence of temporal trends of R10mm for tropical (a) and subtropical (b) Andes dividing eastern and western side of the mountain chain. The plot shows the vertical profile of spatially averaged binned data (top scale) of East (blue) and West (light blue) side of the chain superimposed to the distribution of trends of individual grid points (grey, bottom scale). Vertical profiles include errors on the trend and the significance of the trend (filled squares when $\geq$95%).

### 3.3.2 Seasonal analysis

The objective of this section was to further investigate the Elevation-Dependent Precipitation Change (EDPC), analysing the seasonality of the mountainous regions considered in this study. The primary focus of this work has been on the Tibetan Plateau due to its large size, existing research literature, and the presence of various dynamic patterns. The methodology developed was subsequently applied to the other areas as an initial investigation, further techniques still need to be improved and refined. Indeed, the seasons that have been selected for this analysis are crucial for understanding precipitation patterns and extremes in the Tibetan Plateau area, but may not sufficient for the other regions. For instance, for the GAR, autumn and spring also play an important role in precipitation dynamics, suggesting the importance analysing them in further researches.

The following analysis have been performed with all extreme precipitation indices, but, for conciseness, results are presented only for the representative R10mm index.

## Tibetan Plateau

As explained in section 3.1, precipitation in the area of Tibetan Plateau is characterised by large spatial and seasonal variability. In fact, precipitation formation mechanisms and processes largely change depending on season: summer rainfall is due to the Indian monsoon pattern while winter precipitation can be caused by westerlies dynamics (see Figure B.1). In the following table (3.3), we summarize the results obtained evaluating the altitudinal gradient for individual seasons, computed as the linear regression of the distribution of elevations versus trend values of all grid points. No differences can be seen between the two season, confirming the analysis performed on the whole year. Nevertheless, considering the ineffectiveness of a simple linear regression approach among the TP region, we performed also the binned profile analysis.

**Table 3.3:** Summary of the elevational dependency of ERA5 precipitation indices considering summer season (JJAS) and winter season (DJFM) in the area of the Tibetan Plateau. Orange (blue) colour refers to 95% significance positive (negative) altitudinal gradient. Empty cells indicate no clear and significant behaviour.

| | Pm | R10mm | R20mm | Rx1day | R95p | CWD | CDD |
|---|---|---|---|---|---|---|---|
| Year | | | | | | | |
| Summer (JJAS) | | | | | | | |
| Winter (DJFM) | | | | | | | |

Figure 3.14 shows the same plot as in Figure 3.6a, computing summer and winter vertical profile separately. Although both seasons lead to an overall positive vertical gradient, the summer profile clearly dominates the annual pattern: both the features (drying at low altitude and wetting at high altitude) highlighted in the yearly analysis are consistently found in the summer profile and not discernible in winter. Interestingly, the positive trends observed at 3500-4000 meters, migrate to higher elevations (4000-4500m) considering period 1981-2020 (see Figure B.14 in Appendix B). On the contrary, winter profile shows only a weak deviation from an absent stratification, driving to an overall weak positive vertical gradient.
A source of uncertainties derives from the selection of the TP area, which is large and includes very climatically diverse areas. Because of that, the TP area has been divided into four sectors, maintaining the same number of pixels for each area: north-west (NW [75-90°E; 32.5-

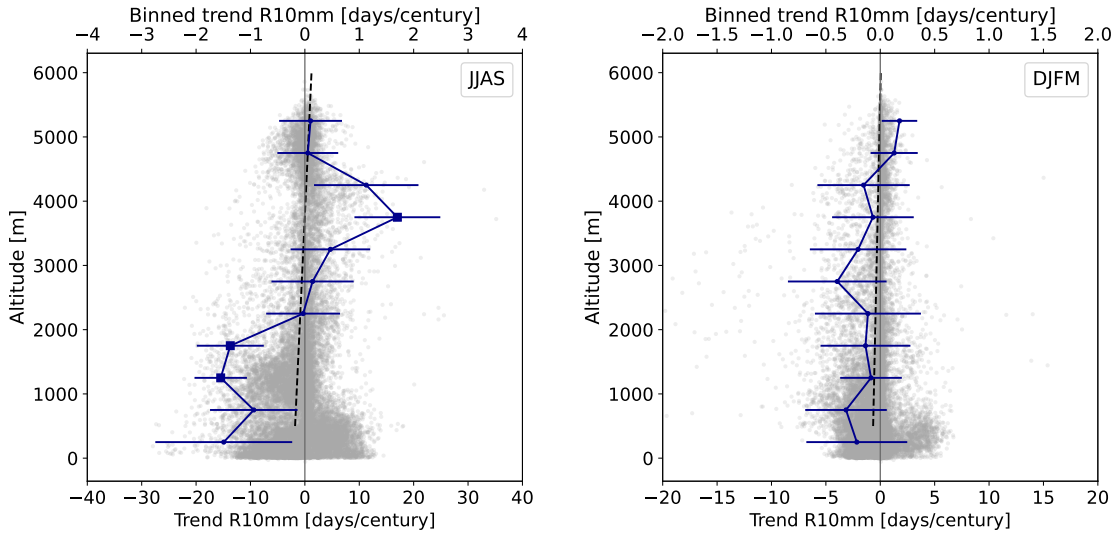


(a) (b)

**Figure 3.14:** Elevational dependence of temporal trends of R10mm for summer season (JJAS) (a) and winter (DJFM) (b) seasons for the TP area. The plot shows the vertical profile of spatially averaged binned data (top scale) of R10mm trend superimposed to the distribution of trends of individual grid points (grey, bottom scale). Vertical profiles include errors on the trend and the significance of the trend (filled squares when >95%).

40 °N]) where we expect a predominant influence of precipitation from the westerlies; north-east (NE [90-105°E; 32.5-40 °N]), dominated by East Monsoon; south-west (SW [75-90°E; 25-32.5 °N]), dominated by Indian Monsoon; and south-east (SE [90-105°E; 25-32.5 °N]), where both south and east monsoons play a role. Table 3.4 presents a summary of both the drying (negative trend) and wetting (positive trend) effects occurring across all four sectors of the TP area. The objective is to provide a more immediate visual representation to discern at which altitudes these phenomena occur, during which seasons, and to determine whether the shape of the overall profile depends on features found consistently within each sub-region. The annual signal is confirmed to be dominated by the summer season, while notably, there is no discernible significant EDPC signal observed in winter. To specify further, the following observation can be made:

**NW** The positive EDPC signal found also in the TP general profile can be localised in this sector and it occurs in the summer season. The larger wetting signal can be found at 4000-4500m.

**NE** No significant elevation dependency can be noticed in this area, both in yearly and seasonal analysis.

**Table 3.4:** The table summarize the temporal trends of averaged binned profiles for the four sectors and the whole new TP area, encompassing both the summer (JJAS) and winter (DJFM) rainfall seasons. The orange (blue) color designates a positive (negative) trend with 95% significance, while a lighter color indicates 90% significance level.

| | **Full Year** | | | | |
|---|---|---|---|---|---|
| | NW | NE | SW | SE | Whole |
| ≥5000m | | | | | |
| 4500-5000m | | | | | |
| 4000-4500m | | | | | |
| 3500-4000m | | | | | |
| 3000-3500m | | | | | |
| 2500-3000m | | | | | |
| 2000-2500m | | | | | |
| 1500-2000m | | | | | |
| 1000-1500m | | | | | |
| 500-1000m | | | | | |
| 0-500m | – | – | | | |

| | **Summer JJAS** | | | | |
|---|---|---|---|---|---|
| | NW | NE | SW | SE | Whole |
| ≥5000m | | | | | |
| 4500-5000m | | | | | |
| 4000-4500m | | | | | |
| 3500-4000m | | | | | |
| 3000-3500m | | | | | |
| 2500-3000m | | | | | |
| 2000-2500m | | | | | |
| 1500-2000m | | | | | |
| 1000-1500m | | | | | |
| 500-1000m | | | | | |
| 0-500m | – | – | | | |

| | **Winter DJFM** | | | | |
|---|---|---|---|---|---|
| | NW | NE | SW | SE | Whole |
| ≥5000m | | | | | |
| 4500-5000m | | | | | |
| 4000-4500m | | | | | |
| 3500-4000m | | | | | |
| 3000-3500m | | | | | |
| 2500-3000m | | | | | |
| 2000-2500m | | | | | |
| 1500-2000m | | | | | |
| 1000-1500m | | | | | |
| 500-1000m | | | | | |
| 0-500m | – | – | | | |

**SW** SW sector is undergoing a strong drying signal at low and mid-altitudes, driven by summer changes. We might relate this evidence to changes in the South Asian monsoon. Further details are given in the discussion (Section 3.4).

**SE** The results are consistent with the SW sub-region.

### US Rockies and Greater Alpine Region

Figure 3.15 shows identical plots as in Figures 3.10a for the RO and 3.8a for the GAR, focusing on the summer season. The high-altitude effect, leading to a drying signal in the RO and a wetting signal in the GAR, is attributed to the summer season, whereas during winter (Figure B.12, Appendix B), no distinctive altitudinal stratification is observed. Furthermore, in both areas, the division between the western-eastern and northern-southern sides of the chain displays no discernible differences (see Figure B.13 in Appendix B). In the GAR, the coherent behaviour of the two sides of the chain was also emphasized in the annual analysis (see Figure 3.9). For the RO, the most prominent difference is noticeable at lower elevations due to the coastal area described in the previous section (Figure 3.11).

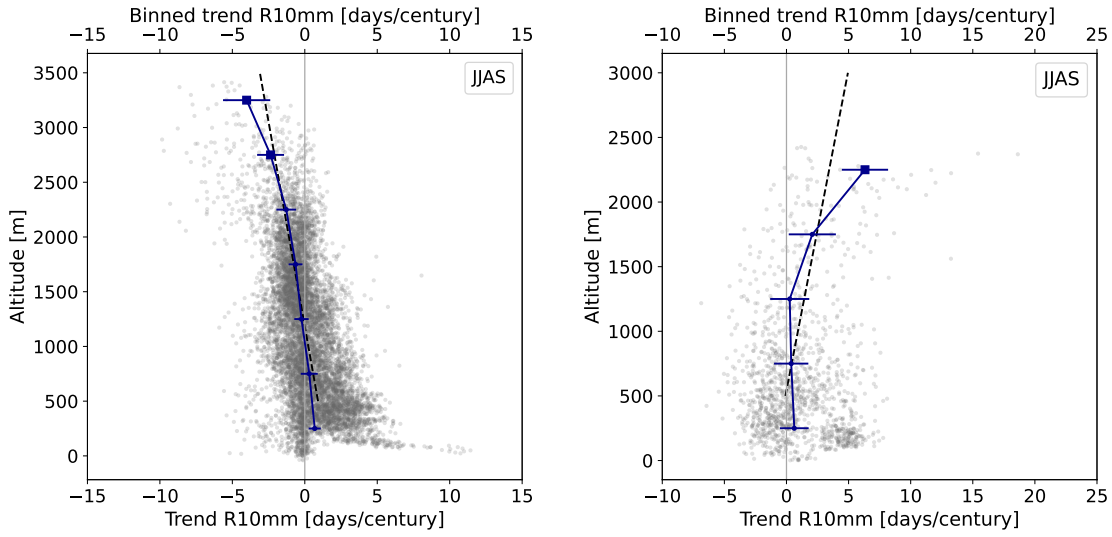


(a) US Rockies

(b) Great Alpine Region

**Figure 3.15:** Same as Figure 3.14 for RO and GAR in summer season (JJAS).

## Andes

Figure 3.16 reports the same analysis shown in Figure 3.13, considering separately austral summer (DJFM - panels b and d) and austral winter (JJAS - panels a and c). In the austral winter season (JJAS)

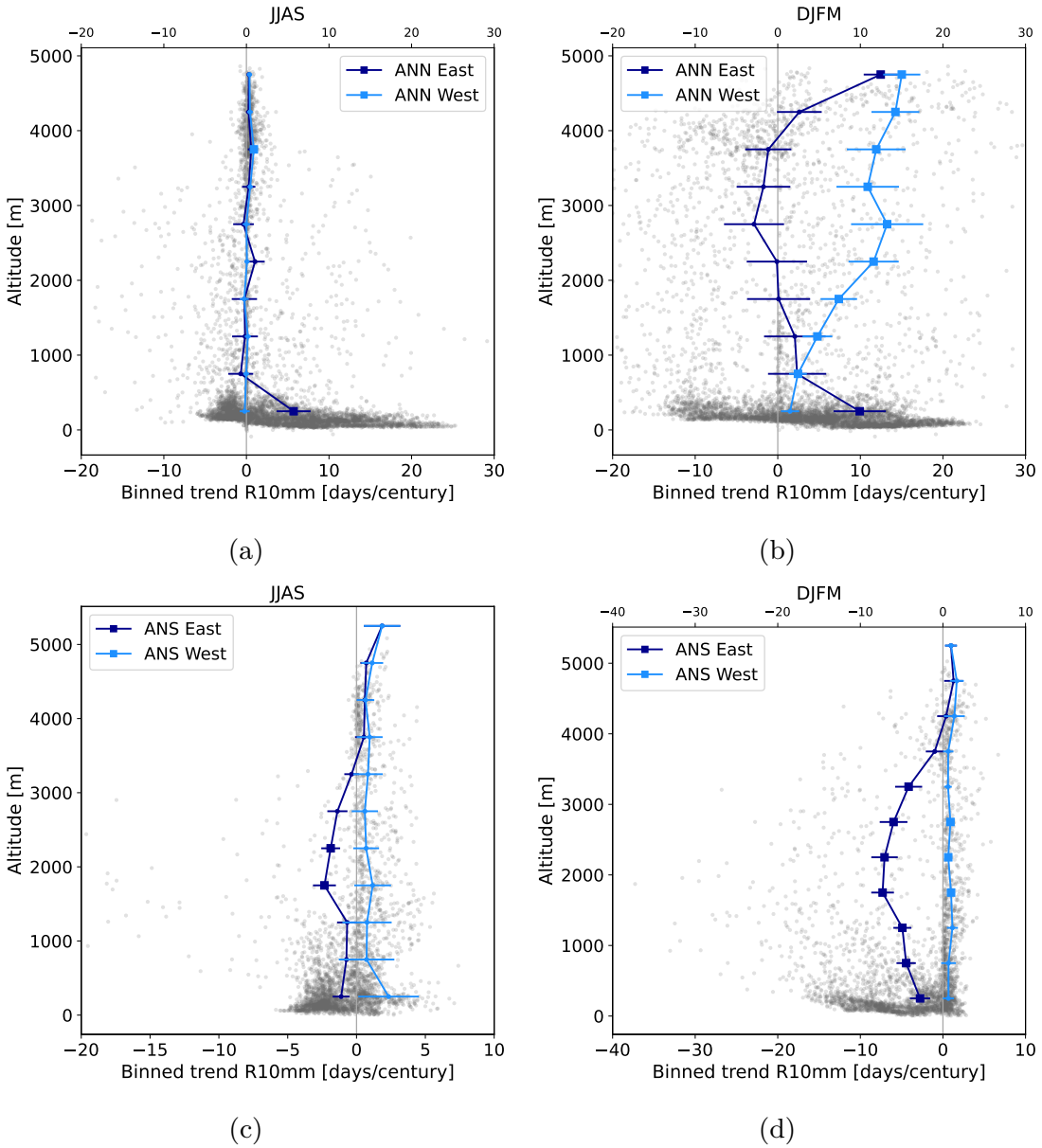


**Figure 3.16:** Same as Figure 3.14 for tropical and sub-tropical Andes dividing eastern (blue) and western (light blue) side of the chain. Panel (a) and (c) represent austral winter season (JJAS) while panels (b) and (d) austral summer season (DJFM) of respectively north and south Andes. Please note that the same scale has been used for binned profile and trend distribution.

no altitudinal stratification can be assessed, while in local summer (DJFM) there is a positive and significant altitudinal gradient considering the overall distribution. In the tropical Andes, the binned profile of the western side of the chain outlines a linear increasing wetting effect with altitude with a strongly enhanced signal at very high altitude, similarly to what happens during the summer season in the GAR and in the north-west sector of TP area. An intriguing aspect to note here is that the western side is the drier region of the Andes, whereas the bulk of precipitation occurs on the eastern side, which does not exhibit any altitudinal dependency. In the subtropical Andes, a non-significant wetting effect is visible at very high altitudes, while a distinct drying signal is evident at mid-altitudes, below 4000 meters. The knee-shaped pattern observed in Figure 3.13b is notably influenced by the local summer, although it is also observable in the local winter.

## 3.4 Discussion

In our study, we conducted a comparative analysis of altitudinal patterns in mean precipitation and extreme precipitation indices trends spanning from 1951 to 2020, encompassing various global mountain regions: the Tibetan Plateau, the Greater Alpine Region, the US Rocky Mountains, and both the tropical and subtropical Andes. Our primary objective was to explore whether, analogously to temperature trends (EDW), precipitation trends also exhibit a dependency with elevation. We evaluated altitudinal stratification through two methods: firstly, by assessing the linear regression of the overall distribution of temporal trends against altitude calculated over each grid point in every area. Secondly, EDPC was assessed by examining the vertical profile of 500 meters-binned spatially averaged trends, which allow to identify which effect (drying or wetting) is causing the altitudinal gradient.

In the Tibetan Plateau, all indices indicate a positive altitudinal gradient, which however was rejected by a simple chi-squared analysis. Evaluating the binned profile, all indices consistently indicate a drying effect occurring at low elevations, particularly below 2000 meters, and driven by the southern part of the Tibetan Plateau during the summer season, as highlighted both by the transect, the seasonal and the sub-regional analysis. Moreover, Pm, R10mm and CWD show a significant wetting signal above 4000 meters, observable in both sides of

the chain. As happens for the drying, also the wetting is due to summer rainfall, concentrated in north-west sector of the Plateau. The study conducted by Hu et al. (2021) has performed a similar analysis over the Tibetan Plateau, using data from 113 meteorological stations along the period spanning from 1971 to 2017. Their investigation focused on the elevational dependency of temporal trends of ETCCDI extreme precipitation indices, revealing a positive stratification with the altitude for total precipitation, CWD, and R10mm, identifying this phenomenon as Elevation Dependent Wetting (EDWE). The concept of EDWE was previously assessed using *in-situ* observation also in the central arid region of China (Yao et al., 2016) and during the summer season over the Tibetan Plateau (Li et al., 2017b). These studies confirm what we have highlighted with our analysis, suggesting that precipitation changes are enhanced at high elevations. About the observed drying effect at low altitudes, we suppose it might be attributed to prevailing changes in atmospheric circulation patterns, possibly influenced by both regional and local factors. The decrease in rainfall could be linked to the recent weakening of the Indian summer monsoon due to the warming of the environment discussed by Kumar et al. (2020). The IPCC's Sixth Assessment Report (AR6, Masson-Delmotte et al., 2021) highlights how the weakening of the South Asian monsoon circulation has led to a decline in seasonal average rainfall over North India and Southwest China from the 1950s to the early 2000s. This decline has been associated with the impact of local aerosol emissions, which saw a dramatic increase due to the rapid industrialization of the region.

In the Greater Alpine Region, only Pm, R10mm, and CWD exhibit a positive gradient with the altitude, almost entirely confined within the summer season as identifiable in both the overall distribution and binned profile. This stratification highlights a wetting signal at high altitudes, above 1500 meters. On the contrary, all other indices do not exhibit any elevational dependency. Additionally, the transect analysis indicates a bias between the northern and southern sides of the mountain chain, even though both show a positive gradient, suggesting that the drivers might be consistent on both sides of the chain. Elevational patterns in the GAR were examined in terms of future projections of both mean and extreme precipitation changes (Kotlarski et al., 2012; Gobiet et al., 2014; Napoli et al., 2023). These studies have revealed that changes in GAR summer precipitation are signifi-

cantly influenced by elevation, showing a positive gradient primarily due to a notable drying effect at lower elevations. Moreover, another study (Giorgi et al., 2016) found out that high-resolution regional climate models (around 12km of spatial resolution) show an increase in mean and extreme precipitation trends over the high-altitude Alpine areas, a signal not seen by global and coarser simulations. This effect has found to be associated with increased summer convective rainfall due to enhanced potential instability by high-elevation surface heating and moistening. In the historical period considered in this study and in the GAR, ERA5 seems to capture the convective signal associated with the summer precipitation pattern, although other studies analysing convective precipitation globally suggest the importance of using higher resolution datasets to capture small-scale processes such as summer convection (Capecchi et al., 2022; Lavers et al., 2022).
In contrast, Gobiet et al. (2014) identified a negative altitudinal gradient in total winter precipitation. They attributed these alterations to changes in convection, possibly resulting from thermodynamic processes, and the influence of the the positive (or warm) phase of the North Atlantic Oscillation (NAO) on winter precipitation changes.

The US Rocky Mountains exhibit an opposite behavior compared to the other regions: all precipitation indices demonstrate a consistent significant negative linear gradient, primarily due to a pronounced drying effect at high altitudes, particularly above 2500 meters. As in the other regions, this signal is concentrated within the summer, while no stratification can be seen during winter. At lower altitudes, the western and eastern sides of the mountain chain exhibit an opposite gradient. This effect can be attributed to the strong precipitation decrease that characterised the coastal zone localised in the northwest of the area, as can be noticed from the transect analysis. In their study, Pepin et al. (2022) computed a comparisons of regional mountain precipitation changes considering different time periods and different datasets (CRU, GPCC, ERA5 and historical experiment from CMIP5 model ensemble). They found that the US Rockies show a decreasing orographic effect in mean precipitation, due to an enhanced drying signal at high elevation (ERA5 1980-2020 not significant, CMIP5 1940-2018 and 1960-2018 significant).

In both the tropical and subtropical Andes, the altitudinal stratification can not be described by a simple linear regression. Within the

tropical zone, no discernible elevational dependency has been identified, while the subtropical zone displays a more complex pattern. Throughout the entire Andes, the annual profile on both sides of the chain is predominantly influenced by the local summer signal (DJFM). Particularly, in the ANN, the western side manifests a positive linear relationship with altitude. Notably, at high altitudes, positive and significant trends result in a wetting effect, aligning coherently with the TP and the GAR. No significant vertical stratification has been observed on the eastern side of the ANN. In contrast, within the ANS, the overall profile is dictated by the eastern side, exhibiting a distinctive knee-shaped profile. This characteristic is evident during the summer but discernible even in the local winter season.

As the primarily objective of our work was to draw overarching conclusions by extrapolating the shared characteristics observed across all different regions that have been considered, the following observations can be made:

1. In all areas mean precipitation (Pm), extreme precipitation (R10mm), and the persistency of rainy condition (CWD) show consist altidudinal profiles of trends.

2. In the RO, in the GAR, and in the western side of the ANN a simple linear regression can efficaciously describe the EDPC while for the ANS and the TP a more complex altitudinal profile has been found.

3. During the local summer season, in the TP, in the GAR and in the western side of the Andes, a significant wetting signal (positive trend) can be identified at high altitude.

4. In all regions, the altitudinal stratification predominantly arises during the summer season.

As briefly described in the introduction, the EDPC results from a combination of various physical processes that can be influenced by both local factor, the general atmospherical circulation dynamics (dynamic drivers) or by thermodynamic relationships between different climate variable changes involved in precipitation formation processes (thermodynamic drivers). The drivers behind the high-altitude wetting effect, which impact all mountain chains except for the RO, might fall into the latter category. Primarily, the intensification of warming at higher altitudes and its interconnected processes, such the snow-ice

albedo feedback, may contribute to the increase in local atmospheric water vapor and air humidity. According to the Clausius–Clapeyron relationship, these alterations can lead to an enhancement of precipitation and more pronounced precipitation extremes at higher altitudes (Hu et al., 2021). Additionally, as noted by Guo et al. (2017), in the Tibetan Plateau region, a reduction of near-surface wind speed has been observed to be more pronounced at high altitudes. Changes in surface wind speed, the so called "stilling" phenomenon, might impact the local convection, potentially resulting in an increase in extreme precipitation at high elevations.

Concerning the RO, it is plausible that dynamic drivers might supersede the thermodynamic effects, particularly given its complex topography and the diversity of the atmospheric patterns impacting the area. In fact, in this area precipitation is influenced by a wide range of atmospheric phenomena, as discussed in section 3.2, notably distinguished between the coastal and interior side of the mountain chain. Future research efforts should focus on examining shifts in the Jet stream and the persistency of storms influenced by westerly winds, similarly to what have been discussed around the Tibetan Plateau's drying impact resulting from modifications in the monsoon.

Chapter 4

# Elevation dependent precipitation change in CMIP6 models

As the mean state of climate is undergoing rapid and severe changes, also its extreme are subject to intensification. Globally, both the frequency and the intensity of precipitation extremes are increasing, influenced by alterations in regional and local weather patterns. This phenomenon is particularly interesting in mountainous regions, where the interlace and overlap of several factors, such as the increase in atmospheric amount of water vapour (Allen and Ingram, 2002), the orographic uplift mechanism (Johnson and Hanson, 1995), and the transition from solid to liquid-phase precipitation (O'Gorman, 2014), contribute to a substantial increase in total and extreme precipitation. Recent assessments have revealed that the long-term variability of distinct climate variables, such as precipitation and temperature, exhibits elevational-dependency, leading to so called Elevation-Dependent Precipitation Change (EDPC) and Elevation-Dependent Warming (EDW) (Pepin et al., 2022).

Global climate models (GCMs) represent a fundamental tool for analysing historical and future climate shifts, variability and trends in global climate. Recently, a new phase of the CMIP project (CMIP6, Eyring et al., 2016) has been released, providing a new generation of models, representing an advancement from traditional GCMs to Earth System Models (Kim et al., 2020). As described in Chapter 1, these models are affected by uncertainties and precipitation stands out as one of the most challenging variables to simulate. This may be largely attributed to the need for parameterizations, particularly in high-altitude areas

where sub-grid scale processes play a leading role influencing precipitation formation mechanisms and the entire hydrological cycle (e.g. orographic lifting of air masses or climate feedbacks). The use of climate models, both global and regional, offers notable advantages in exploring EDPC, as already highlighted for EDW. Firstly, they can aid in identifying the principal mechanisms underlying elevational-dependencies by providing outputs for multiple variables (drivers) potentially responsible for or linked to this phenomenon (Palazzi et al., 2019). Secondly, long-term simulations allow for both the reproduction of the past and the exploration of future projections. A comprehensive evaluation of climate models' performance is crucial for the precise interpretation of the phenomenon and to elaborate accurate discussions of the simulated results. Historical climate model simulations can be evaluated to assess the models' capabilities in reproducing both average and extreme precipitation in the recent past, enabling comparisons with other datasets (e.g., reanalyses, in-situ stations, or satellite products) and models verification and validation. Additionally, understanding the impact of distinct model characteristics, such as the resolution, in simulating EDPC is a fundamental step that has not been investigated in detail yet and requires further specific studies. To our knowledge, these aspects have not been extensively explored, as the only existing studies are focused on EDW (e.g. Im and Ahn, 2011; Rangwala and Miller, 2012). For instance, Palazzi et al. (2019) have highlighted the crucial role of the model spatial resolution in capturing specific EDW characteristics, such as the strength and the relative role of distinct driving mechanisms, particularly in small mountain areas, such as the Alps, compared to wider ones, such as the Tibetan Plateau-Himalayas.

The objective of this section is to evaluate the capability of CMIP6 model historical simulations in assessing EDPC in different mountain regions, exploring both the model ensemble-mean and the inter-model variability. The selected regions are the Tibetan Plateau (TP), the Greater Alpine Region (GAR), the US Rockies (RO) and the Andes, both tropical (ANN) and sub-tropical (ANS) and a description of their climatological precipitation is provided in section 3.2. In addition, a validation of these outputs has been performed through a comparison with ERA5 reanalysis, whose results have already been discussed in Chapter 3.

## 4.1 Data and methods

Two types of precipitation data have been used in this chapter, the ERA5 reanalysis and CMIP6 climate models outputs. ERA5 daily precipitation data are provided by the fifth generation of the ECMWF reanalysis, downloaded in October 2022 from the Copernicus Climate Change Service Climate Data Store (CDS), as explained in chapter 3.1. We recall that ERA5 is characterized by high temporal frequency (hourly records) at 31 km horizontal resolution. The dataset has been modified to obtain daily precipitation totals and then interpolated on to a 0.25°x0.25° latitude-longitude regular grid. More information are provided in Hersbach et al. (2023). In this study, the ERA5 reanalysis has been used as the primary reference dataset for the evaluation of historical CMIP6 model outputs. 29 GCMs from CMIP6, listed in table 4.1, have been analysed. We selected the models for which daily precipitation data were available at the time when we downloaded the data (June 2023). A single member for each model (r1i1p1f1) has been used for fair comparisons. Models have been used both at their original spatial resolution (section 4.2.3) and interpolated onto a regular grid of 1°x1° lat-lon (section 4.2.1). A sub-set of twelve high-resolution CMIP6 models has been identified, selecting the ones with latitude resolution below 1°.
To characterize the variability and changes in precipitation extremes, we used a set of ETCCDI indices. We briefly list them here, with a more detailed description available in chapter 3.1: R10mm [*days*], R20mm [*days*], Rx1day [*mm/day*], R95p [*mm/year*], CWD [*days*] and CDD [*days*].

The elevational-dependency of precipitation changes was studied using the two complementary methodologies described in chapter 3.1. The differences with the previous analysis are that precipitation indices trends have been computed over the period 1950–2014, in order to have the largest period in common between ERA5 and CMIP6 historical models. Moreover, we chose altitudinal bins of 1000 meters width instead of 500 meters, ensuring at least 10 pixel into each bin.

The first part of the analysis presented in this chapter uses the CMIP6 model ensemble-mean (MEM). Precipitation extreme indices have been calculated for each model at their original spatial resolution, they have been interpolated over a regular grid of 1°x1° lat-lon and then the MEM has been computed; finally, we applied both definitions of

**Table 4.1:** List of 29 CMIP6 models considered in this study, accompanied by a key reference, their spatial resolution (latitudexlongitude) and the name of the atmospheric module. Only one ensemble member (r1i1p1f1) of each CMIP6 model has been considered. The sub-set of high-resolution models is highlighted in yellow.

| CMIP6 | | | | |
|---|---|---|---|---|
| Model name | Institution name | Spatial resolution | Atmospheric module | Reference |
| ACCESS-ESM1-5 | CSIRO | 1.25°x1.88° | MetUM-HadGEM3-GA7.1 | Ziehn et al. (2020) |
| ACCESS-CM2 | CSIRO-ARCCSS | 1.25°x1.88° | HadGAM2 | Bi et al. (2013) |
| BCC-CSM2-MR | BCC | 1.42°x1.13° | BCC_AGCM3_MR | Wu et al. (2022) |
| CanESM5 | CCCma | 3.42°x2.81° | CanAM5 | Swart et al. (2019) |
| CESM2 | NCAR | 0.94°x1.25° | CAM6 | Danabasoglu et al. (2020) |
| CESM2-WACCM | NCAR | 0.94°x1.25° | WACCM6 | Gettelman et al. (2019) |
| CMCC-CM2-SR5 | CMCC | 0.94°x1.25° | CAM5.3 | Cherchi et al. (2019) |
| CMCC-ESM2 | CMCC | 0.94°x1.25° | CAM5.3 | Cherchi et al. (2019) |
| CNRM-CM6-1 | CNRM | 1.4°x1.4° | Arpege 6.3 | Voldoire et al. (2019) |
| EC-Earth3 | EC-Earth-Cons | 0.9°x0.7° | IFS cy36r4 | Döscher et al. (2022) |
| EC-Earth3-CC | EC-Earth Cons | 0.9°x0.7° | IFS cy36r4 | Döscher et al. (2022) |
| EC-Earth3-Veg | EC-Earth Cons | 0.9°x0.7° | IFS cy36r4 | Döscher et al. (2022) |
| EC-Earth3-Veg-LR | EC-Earth Cons | 1.4°x1.25° | IFS cy36r4 | Döscher et al. (2022) |
| FGOALS-g3 | CAS | 2.8°x2° | GAMIL3 | Li et al. (2020) |
| GFDL-ESM4 | NOAA-GFDL | 1°x1.25° | GFDL-AM4.0.1 | Dunne et al. (2020) |
| GFDL-CM4 | NOAA-GFDL | 1°x1.25° | GFDL-AM4.1 | Adcroft et al. (2019) |
| IITM-ESM | CCCR-IITM | 2.3°x1.8° | IITM-GFSv1 | Krishnan et al. (2019) |
| INM-CM4-8 | INM | 2°x1.5° | INM-AM4-8 | Volodin et al. (2017b) |
| INM-CM5-0 | INM | 2°x1.5° | INM-AM5-0 | Volodin et al. (2017a) |
| IPSL-CM6A-LR | IPSL | 1.27°x2.5° | LMDZ | Boucher et al. (2020) |
| KIOST-ESM | KIOST | 1.88°x1.88° | GFDL-AM2.0 | Pak et al. (2021) |
| MIROC6 | MIROC | 1.72°x1.41° | CCSR AGCM | Tatebe et al. (2019) |
| MPI-ESM1-2-LR | MPI | 1.85°x1.88° | ECHAM6.3 | Mauritsen et al. (2019) |
| MPI-ESM1-2-HR | MPI | 0.93°x0.94° | ECHAM6.3 | Müller et al. (2018) |
| MRI-ESM2-0 | MRI | 1.4°x1.13° | MRI-AGCM3.5 | Yukimoto et al. (2019) |
| NESM3 | NUIST | 1.88°x1.88° | ECHAM v6.3 | Cao et al. (2018) |
| NorESM2-LM | NCC | 0.95°x2.5° | CAM-OSLO | Seland et al. (2020) |
| NorESM2-MM | NCC | 0.9°x1.25° | CAM-OSLO | Seland et al. (2020) |
| TaiESM | AS-RCEC | 0.9°x1.25° | TaiAM1 | Lee et al. (2020) |

EDPC signal, as explained in section 3.1.

In the second section, we have performed a comparison between CMIP6 model simulation of EDPC with ERA5 signal, over the common reference period 1950–2014. ERA5 have been interpolated on a regular grid of 1°x1° latitude-longitude and the altitudinal bins have been enlarged from 500 to 1000 meters, fisrtly to assess that the results obtained in chapter 3 were still verified with a coarser resolution, then to perform the comparison.

To gather CMIP6 models that shares similar EDPC signals, a clustering method was employed. The non-hierarchical k-means clustering algorithm, as introduced by Hartigan and Wong (1979), was applied to the altitudinal binned profiles of the R10mm index simulated by twelve high-resolution CMIP6 models, dividing them into k clusters,

minimize the total intra-cluster variance, as a measure of how spread the data points are from the center of the cluster. The algorithm's outcome depends on the initially prescribed number of clusters, hence it is typically run multiple times with varying k values. Different numbers of clusters were identified for each study area, introducing some subjectivity into the final decision on the cluster number. This was done to strike a balance between achieving good homogeneity within elements of the same cluster and avoiding excessive partitioning of regions, which could result in a reduced number of elements in each cluster (Cattani et al., 2021). Furthermore, an additional test was conducted to determine the appropriate number of clusters using the Elbow method (Humaira and Rasyidah, 2020). This method consists of plotting the sum of squared errors (SSE) against the number of clusters and selecting the point where the rate of SSE decrease noticeably decelerates, indicating the optimal clustering configuration for the dataset. Unless otherwise specified, the number of clusters selected is confirmed by this analysis.

## 4.2 Results

### 4.2.1 CMIP6 model ensemble mean (MEM)

We first conducted an analysis of the altitudinal stratification of both mean and extreme precipitation in the reference period 1950–2014 of the historical experiment, using the model ensemble-mean (MEM) of CMIP6 models, as detailed in Section 4.1. The MEM serves as a representation of shared features in the simulated climate change, surviving the process of ensemble averaging and reflecting the consensus across the all group of models.
EDPC can be evaluated with two complementary approaches: firstly, as the altitudinal gradient of the overall trend distribution of individual grid points within each study area, computed as a linear regression with the elevation. Secondly, it can be evaluated as the vertical profile of 1000 meters-binned averaged temporal trends. Similarly to what have been done in table 3.1 (chapter 3) with ERA5 dataset, table 4.2 summarises the results obtained with the first methodology. In the TP, RO, and ANN areas, the majority of the selected indices exhibits a positive altitudinal gradient. However, only in the RO the distribution appears adequately represented by a simple linear regression, as indicated by the chi-squared analysis. In the GAR, all indices show

**Table 4.2:** Summary of the elevational dependency of CMIP6 MEM precipitation indices over the 5 target regions Tibetan Plateau (TP), Greater Alpine Region (GAR), Rockies (RO) and Andes split in Northern part (ANN) and Southern part (ANS). Orange (blue) colour refers to 95% significance positive (negative) altitudinal gradient. Asterisk means acceptable reduced chi squared analysis. Empty cells indicate no clear and significant behaviour.

| | Pm | R10mm | R20mm | Rx1day | R95p | CWD | CDD |
|---|---|---|---|---|---|---|---|
| TP | | | | | | | |
| GAR | | | | | | * | |
| RO | * | * | | * | * | * | |
| ANN | | | | | | | |
| ANS | | | | | | | |

no significant altitudinal gradient, except for a positive and significant value in CWD, reflecting the persistence of rainy conditions. Finally, the ANS demonstrates a significant negative elevational gradient for the Rx1day and R95p indices.

As explained in chapter 3, it is fundamental to evaluate the EDPC mechanism also analysing the altitudinal binned profile of the temporal trends of the chosen indices, as the overall gradient value can be the result of various phenomena occurring at both high and low elevations. Figure 4.1 shows the details of the altitudinal binned profiles superimposed to the distribution of trends of individual grid points over the five mountain areas considered. We decide to show here only two indices, R10mm and Rx1day, as for the other indices similar considerations can be drawn. For completeness, the indices not shown here are reported in Appendix C. For the GAR, however, the CWD profile has been shown instead of Rx1day as this index show a slightly different profile compared to the others.

***Tibetan Plateau*** R10mm (panel a) exhibits a widespread distribution below 5000 meters, with a central core where trends tend to concentrate around positive values. The vertical profile reveals a positive linear dependency, showing a significant drying effect at low altitudes, below 1000 meters, and a wetting effect at high altitudes, above 4000 meters. As for Rx1day (panel b), the trend distribution is sufficiently compact, displaying no altitudinal dependency. The binned profile confirms this behavior: trends are positive and significant but they show no clear relationship with elevation.

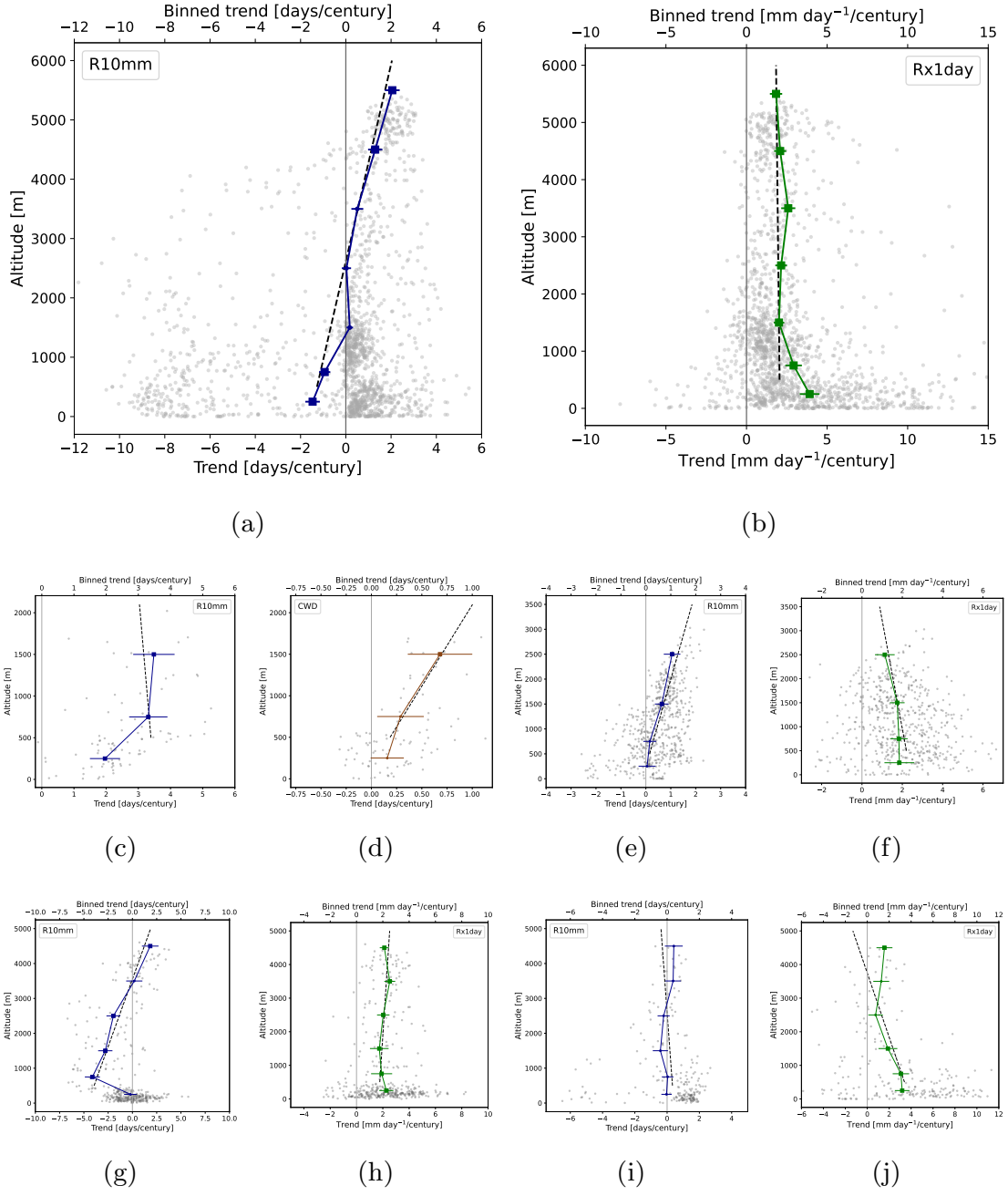


**Figure 4.1:** Elevational-dependence of temporal trends of precipitation indices (see labels) for all mountain areas taken into account: TP panels (a) and (b); GAR (c) and (d); RO (e) and (f); ANN (g) and (h); ANS (i) and (j). Each panel shows the vertical profile of spatially averaged binned data (top scale) superimposed to the distribution of trends of individual grid points (grey, bottom scale). Vertical profiles include errors on the trend and the significance of the trend (filled squares when >95%). Point distributions are accompanied by their linear regression (dashed line).

***Greater Alpine Region*** R10mm (panel c) and CWD (panel d) profiles show positive and significant binned trends, with a visible increase with the altitude for CWD and no discernible altitudinal stratification for R10mm. The distribution in both cases is broad and characterised by a relatively low number of pixels, underscoring how the coarse resolution of CMIP6 models, compared with the GAR extent, can strongly impact the representation of the EDPC.

***US Rockies*** The distribution of R10mm (panel e) is compact and exhibits a clear positive dependency with altitude, as confirmed by the binned profile. It also shows a significant wetting effect above 1500 meters. Rx1day (panel f) presents a broader distribution, and displays a significant linear negative EDPC. The inspection of the binned profile reveals significant and positive trends whose values diminish with the elevation.

***Andes North*** R10mm (panel g) shows a linear and positive EDPC considering both methods, caused by a drying effect below 3000 meters, that decreases with the elevation, and a significant wetting effect above 4000 meters. Concerning Rx1day (panel h), significant positive trends have been evaluated in the overall profile but no altitudinal stratification can be observed.

***Andes South*** R10mm (panel i) reveals no altitudinal stratification with both methods. Rx1day (panel j) is characterised by a broad distribution, particularly below 2000 meters. Its binned profile exhibits a more complex pattern, featuring a weak knee-shape with an inversion in the gradient between 2000 and 3000 meters.

### 4.2.2 Comparison between the CMIP6 MEM and the ERA5 reanalysis

The CMIP6 MEM from historical simulations was compared to ERA5 reanalysis. ERA5 resolution has been degradated from 0.25° to 1° latitude-longitude (ERA5deg), and subsequently, the amplitude of the altitudinal bins has been modified from 500 to 1000 meters.

Figure 4.2 shows the overall distribution and the altitudinal binned profile of the R10mm trends computed with ERA5 at its original resolution with 500 meters-bins and with ERA5deg, considering 1000 meter-bins, for each study area. Comparing panels (a) to (b), (e) to

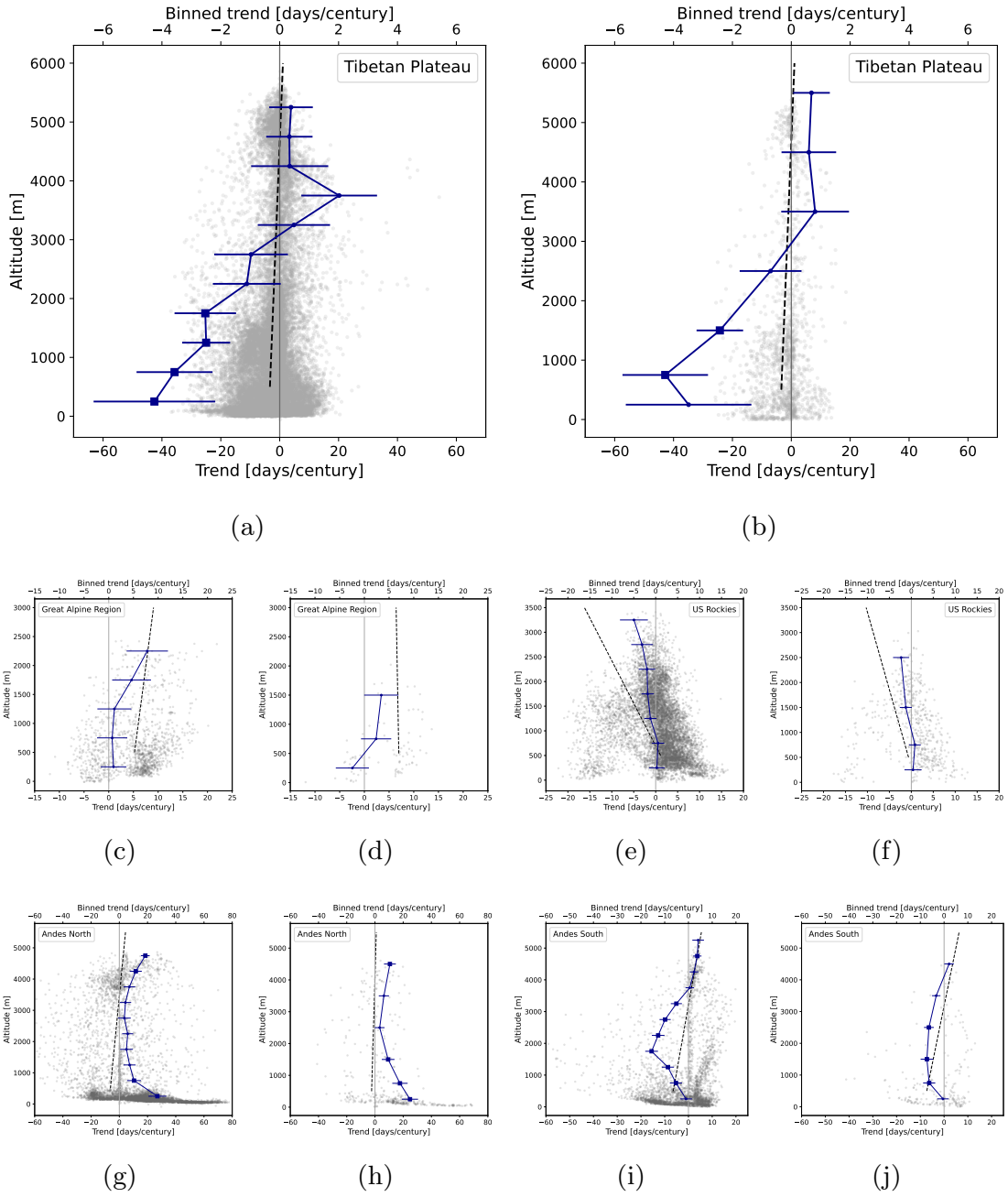


**Figure 4.2:** Elevational-dependence of temporal trends of R10mm for all mountain areas taken into account: TP panels (a) and (b); GAR (c) and (d); RO (e) and (f); ANN (g) and (h); ANS (i) and (j). Right hand panels represent ERA5 R10mm trends for the period 1950–2014 with 0.25° spatial resolution and 500 meter-bins. Left hand panels 1° spatial resolution and 1000 meter-bins.

(f) and (g) to (h), the difference in the resolution for the TP, the RO and the ANN does not substantially alter the altitudinal stratification shown by the profiles. The primary characteristics highlighted in

chapter 3 are also discernible with coarser resolution and wider altitudinal bins. Specifically, for the TP, both the drying effect at low altitudes and the wetting effect at high elevations are clearly evident, and an overall positive and significant EDPC emerges from the linear regression. Considering the RO, a negative EDPC caused by an increasing drying effect with elevations is observable in both panels, although with ERA5deg, the EDPC signal becomes non significant. In the ANN no significant altitudinal gradient is found with both resolutions, however the significant positive trend shown at very high altitudes, also highlighted in chapter 3.3.1, persists.
In contrast, in the GAR (panel (c) and (d)) and in the ANS ((i) and (j)), the different resolution leads to substantial discrepancies in the altitudinal stratification of the R10mm index trend. In both regions, the linear regression describing the EDPC signal becomes non-significant. In the GAR, ERA5deg profile consists of only two bins above 500 meters and they exhibit no distinct altitudinal stratification. In the ANS, the wetting effect at very high altitudes becomes non-significant, and the characteristic knee-shape of the profile, which describes a drying effect with two distinct gradients, becomes less pronounced.

The juxtaposition of the right panels in Figure 4.2 - ERA5deg - with the corresponding left-hand panels of Figure 4.1 - CMIP6 MEM - describes a comprehensive comparison and validation of the MEM results. To facilitate the visualization, another plot has been created, where the altitudinal profiles obtained with the two datasets have been superimposed (Figure 4.3). In the TP and in the GAR, the EDPC identified through the CMIP6 MEM analysis - positive for the TP and non-significant for the GAR - seems to be corroborated by ERA5deg. Concerning the GAR, trends exhibit compatibility within the error bars, whereas in the TP, the profile shape remains consistent but there is a positive BIAS (MEM minus ERA5deg is positive). In the RO and the AN, MEM profiles notably deviate from those evaluated with ERA5deg: in the RO, above 1000 meters, the two datasets display opposite profiles: a negative (positive) gradient is shown by ERA5deg (CMIP6). A similar pattern can be observed in the ANN, where below 3000 meters ERA5deg shows a negative gradient while the CMIP6 MEM a positive one. In general, in the overall Andes, the ERA5deg R10mm temporal trends seems to be amplified with respect to the CMIP6 MEM values; this is particularly evident in the ANS where ERA5deg profile show an elevational-dependency much more

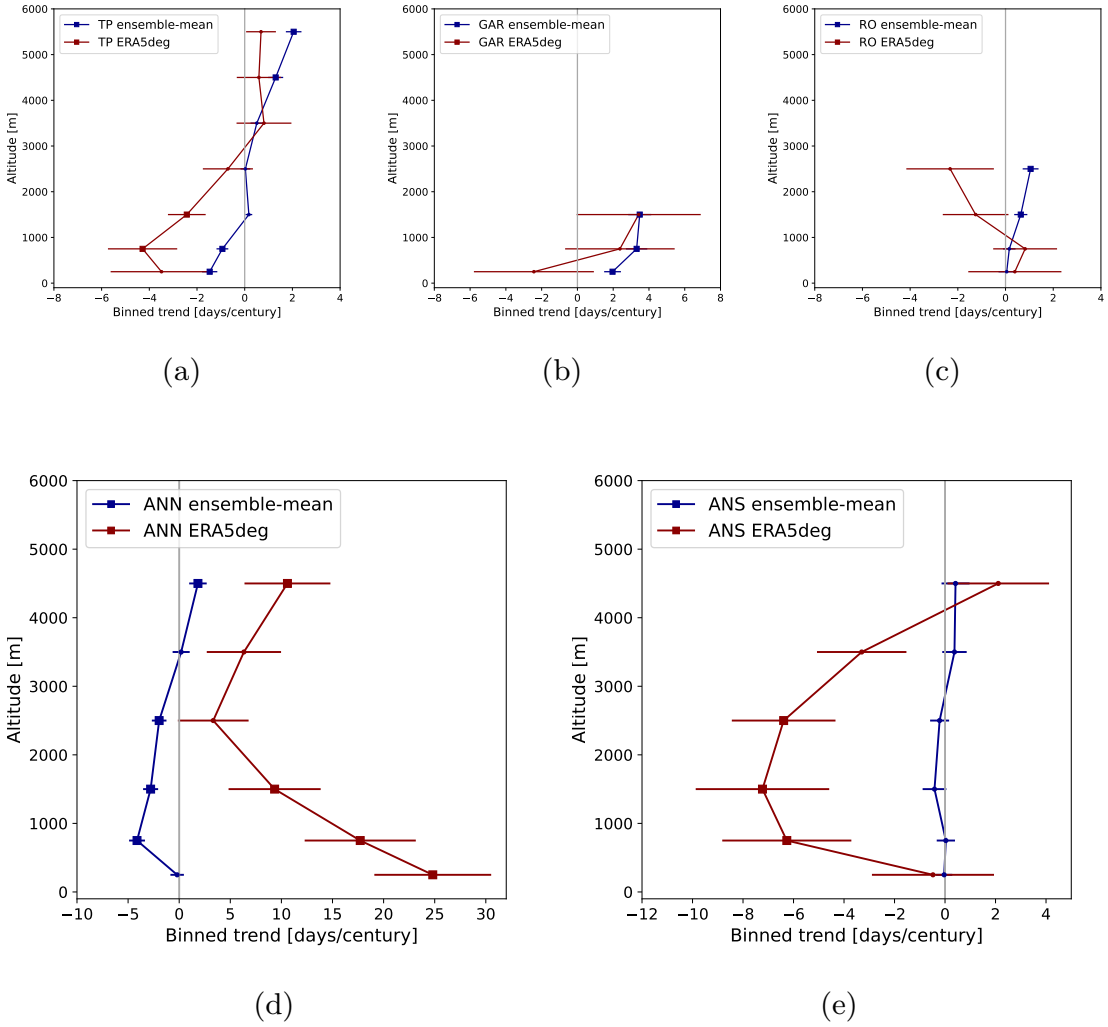


**Figure 4.3:** Juxtaposition of the altitudinal binned profiles of R10mm trends obtained with the ERA5deg (red profile) and CMIP6 MEM (blue profile).

amplified, with trends around ten times more negative then MEM trends.

### 4.2.3 CMIP6 models validation

As previously discussed in section 4.2.1, the analysis of how the CMIP6 MEM represents EDPC is crucial for mitigating the impact of model specific biases. However, the ensemble-mean can be significantly misleading in representing phenomena largely affected by inter-model spread. Therefore, each individual model outcome, as well as their capability to represent EDPC, has been further investigated, in order to develop a better understanding of their uncertainties.

In this section, we evaluate whether the CMIP6 models listed in Table 4.1 are able to capture the geographical variability of the R10mm long-term average (mean value in the period 1950–2014). To achieve this, the spatial distribution of extreme precipitation climatology from ERA5 and CMIP6 models has been compared using a Taylor diagram. A Taylor diagram is a concise way to show how well spatial patterns of the same variable simulated by different datasets match with each other, after identifying a reference dataset, in this case ERA5. This kind of representation manages to investigate together the spatial correlation, the root-mean-square error, and variance ratio between different fields (Taylor, 2001).

In the Tibetan Plateau (TP), the correlation coefficient between the spatial distribution evaluated with CMIP6 models and ERA5 ranges from 0.7 to 0.95, indicating a generally good correlation, with the exception of the FGOALS-g3 model, which exhibits a correlation lower than 0.5. Additionally, the all models fall below the reference standard deviation, implying that they generate narrower variations compared to the observed data, underestimating the spatial variability.
In the GAR, most models exhibit correlations ranging between 0.5 and 0.8, with a fairly even distribution between higher and lower values of variability, independently in high and low resolution models. Notably, the group of models characterised by higher correlation values (above 0.7) is predominantly composed of high-resolution models, such as EC-Earth3 (around 0.85) and the GFDL models (around 0.8), along with some lower resolution models, including EC-Earth3-Veg-LR, MRI-ESM2-0, and INM models. All other high-resolution models exhibit low correlation (between 0.4 and 0.6).
In the RO, all models show lower spatial variability compared to the reference, except for FGOALS-g3. The correlation coefficient is generally high, with most models falling within the range of 0.8 to 0.95 (notably, all high-resolution models exceed 0.9); however, certain models, like FGOALS-g3 or IITM-ESM, significantly deviate from the others.
In the ANN, most models exhibit poor performance in simulating extreme precipitation. Generally, high-resolution models perform better in terms of the correlation coefficient, although with some exceptions. Specifically, several models, including some high-resolution ones like the CMCC models and TaiESM, display very low correlations (below 0.4). Another subset of models falls within the correlation range 0.6–0.8, encompassing both high and low resolution models.

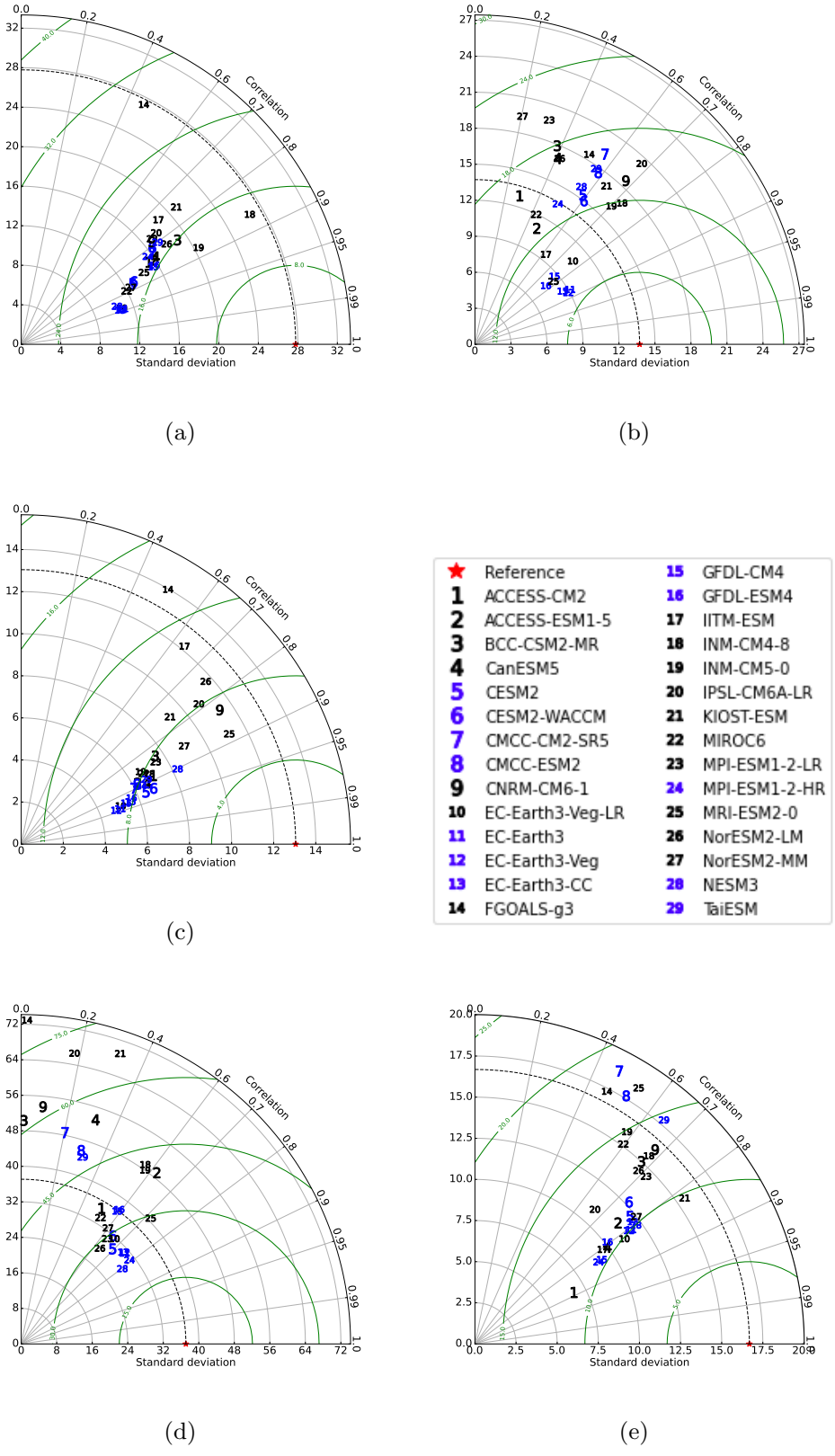


**Figure 4.4:** Taylor diagrams for long-term mean R10mm index over all mountain areas [TP (panel a), GAR (panel b), RO (panel c), ANN (panel d) and ANS (panel e)] comparing each of the CMIP6 models with ERA5 reference dataset (red star marker) for the period 1950–2014. The high-resolution CMIP6 models are highlighted in a different color (blue). Please note that different radial scale have been used for the different areas.

In the ANS, models align more closely with ERA5 compared to the ANN. The majority of models exhibits lower standard deviation values but maintains correlations above 0.7, with none of them falling below 0.4. Notably, three high-resolution models — namely CMCC-CM2, CMCC-ESM2, and TaiESM - display worse performance than the other, as observed in ANN.

In general, the majority of high-resolution CMIP6 models successfully capture the spatial distribution characteristics of long-term averaged R10mm. However, in the Andes region, even some high-resolution models exhibit significant deviations compared to ERA5. The performance of low-resolution models is generally inferior, with FGOALS-g3 being the least accurate across most areas. Taking these observations into account, we chose to focus our next analysis on the subset of CMIP6 models characterized by the highest resolution.

### 4.2.4 K-mean cluster analysis

The k–mean clustering method (details in section 4.1) was applied to the binned altitudinal profile of the R10mm temporal trends simulated by the high-resolution subset of CMIP6 models, regridded over a regular 1° latitude-longitude grid. The aim is to identify common characteristics between model simulations and see if one or more clusters resemble ERA5deg profile in all study areas (right-hand panels of Figure 4.2). Figure 4.5 illustrates the four clusters' altitudinal binned profiles selected for the TP. Although the Elbow Method highlights three as the optimal number of clusters for this area (see Figure C.6 in Appendix C.2), we decided to select four clusters. Even though, one cluster consists of only one model (cluster #3), its profile diverges significantly from the others, and treating it separately has proven to be more effective to analyse the characteristics of altitudinal profiles. Cluster #2 exhibits a profile that closely resembles the ERA5deg one, albeit affected by a positive bias (model minus ERA5deg) and a difference in the 500-1000 meters bin. Cluster #1 is also noteworthy: while its profile shape differs, it exhibits the two signals that caused an overall positive EDPC, highlighted in Chapter 3 for this area — a drying signal at low altitude and a wet signal at high altitude - and the trend values are compatibles within the error bars. Lastly, cluster #4 does not share common characteristics with the ERA5deg profile.

Figure 4.6 shows the binned vertical profiles of the three selected clus-

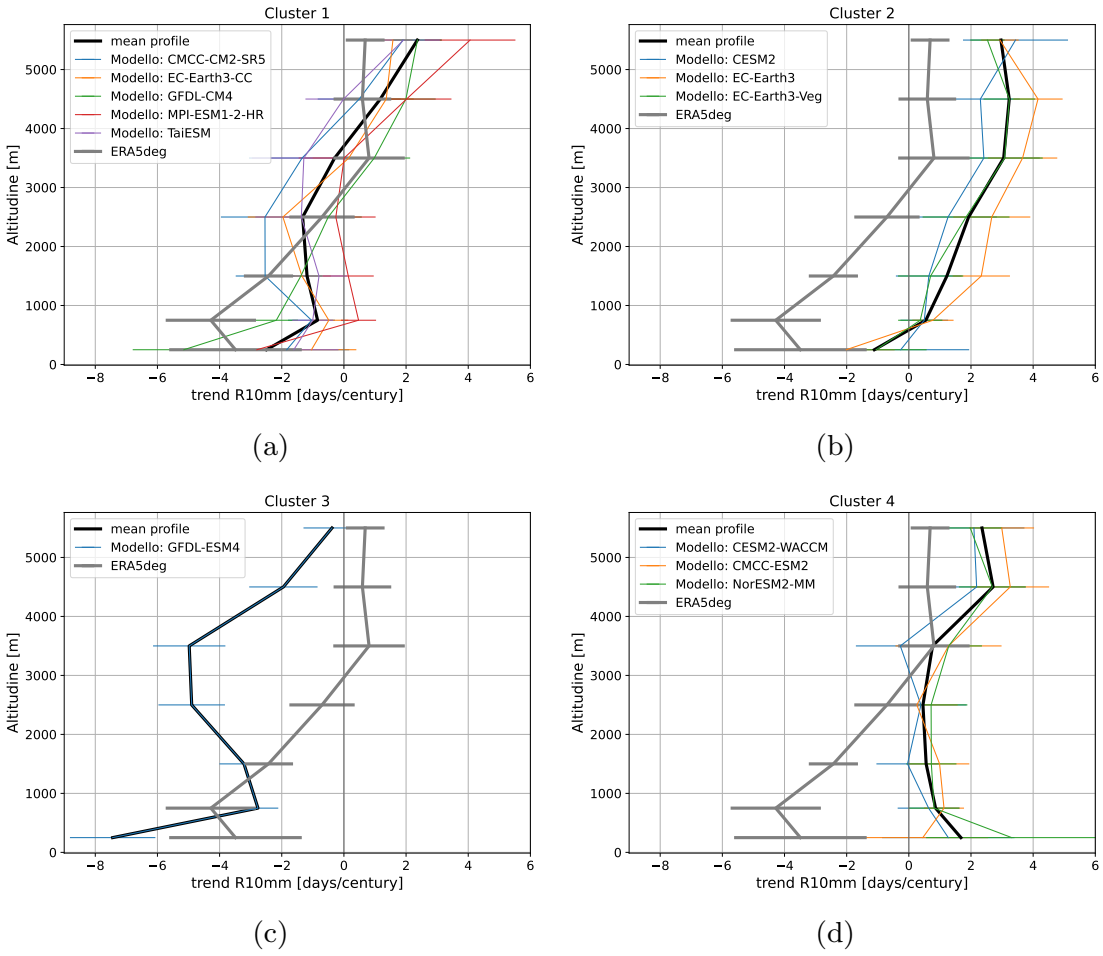


**Figure 4.5:** Tibetan Plateau. Altitudinal binned profile of R10mm temporal trends of each high-resolution CMIP6 models, divided into four clusters with the k-mean method. In each panel is also shown the mean profile for each cluster (black line) and ERAdeg profile (gray line).

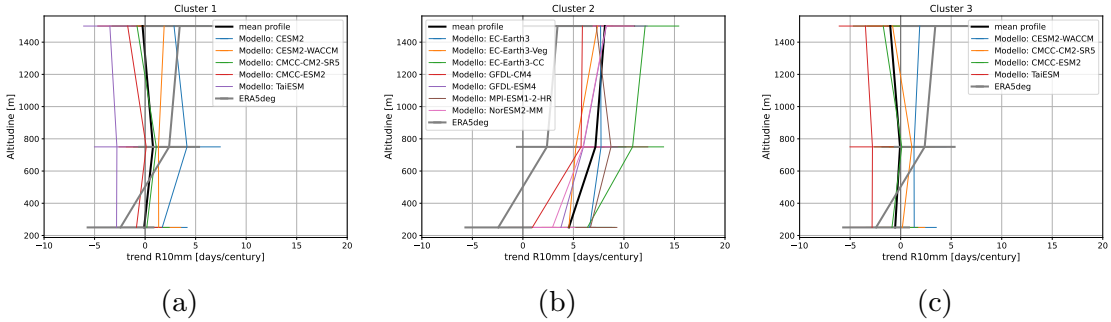


**Figure 4.6:** Same as Figure 4.5 but for the Greater Alpine Region.

ters for the GAR. Firstly, above 500 meters, the profile consists of only two bins, so it should be interpreted with caution. Secondly, all

three clusters profiles are consistent with ERAdeg within the error bars. However, Cluster #1 (panel a) and Cluster #3 (panel c) exhibit values of trend closer to those assessed with ERA5deg, while Cluster #2 (panel b) shares a similar profile shape, albeit affected by a bias.

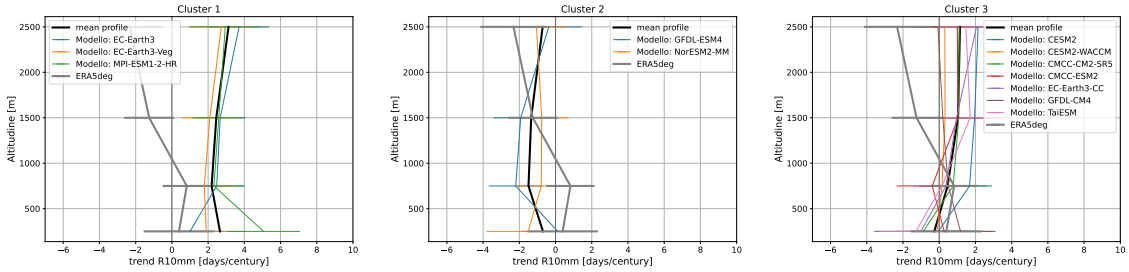


(a) (b) (c)

**Figure 4.7:** Same as Figure 4.5 but for US Rockies.

In the RO, three clusters have been identified and shown in Figure 4.7. Cluster #1 and #3 exhibit a positive EDPC with increasing trends at higher altitudes, while cluster #2 shows no discernible altitudinal stratification. None of them closely resembles the ERA5deg profile, although trend values below 1000 meters for cluster #3 are within the margin of error.

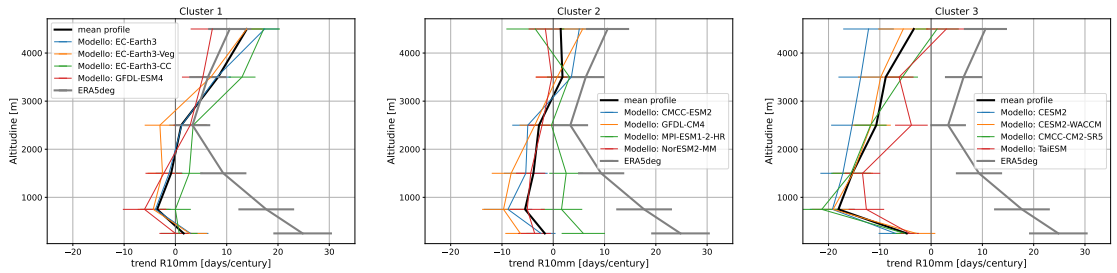


(a) (b) (c)

**Figure 4.8:** Same as Figure 4.5 but for tropical Andes.

Also in the ANN, three clusters have been evaluated and their profile presented in Figure 4.8. The first cluster (panel a) is characterized by a positive and linear altitudinal stratification, with negative trends at low altitudes, that diminish with elevation, and positive trends at high altitudes. Cluster #2 (panel b) shows a similar profile with a smaller gradient, while cluster #3 (panel c) resembles #1 but it is displaced

toward negative values. When comparing these profiles to ERA5deg, none of them precisely replicates the entire profile, but cluster #1 shows compatible trend values at high altitudes (above 2000 meters).

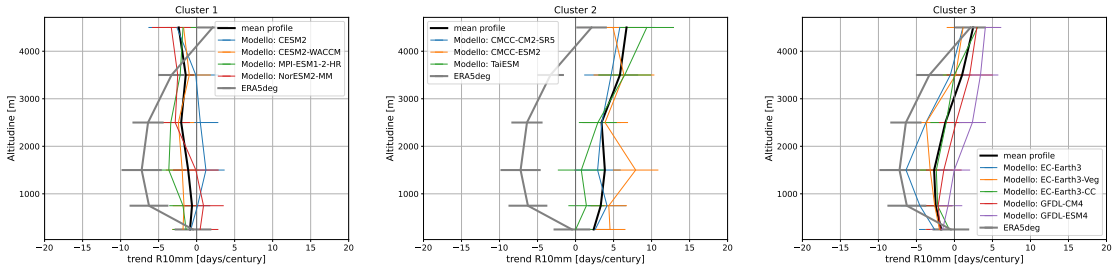


(a) (b) (c)

**Figure 4.9:** Same as Figure 4.5 but for sub-tropical Andes.

Figure 4.9 shows the binned altitudinal profiles of the three selected clusters for the sub-tropical Andes. Cluster #1 shows no stratification with altitude, while clusters #2 (panel b) and #3 (panel c) display a positive EDPC. Cluster #2 exhibits a wetting signal that almost linearly increases with elevation, while cluster #3 shows a C-shape profile with negative trends at low altitudes and positive trends at high altitudes. The ERA5deg profile has a similar shape to the one shown by cluster #3, albeit with larger values.

## 4.3 Discussion

Analyzing changes in extreme precipitation in high-elevation areas is a matter of great importance as intense rainfall might represent a trigger for geo-hydrological hazards. In fact, the complex topography of these regions has the potential to amplify the consequences of extreme precipitation events, such as landslides, flash floods, or debris flows, resulting in significant socio-economic impacts on global population. Consequently, it is crucial to develop an extensive investigation to discern whether the elevational-dependency of changes in precipitation and its extremes can be assessed, locally and globally, focusing especially on future projections. Hence, the use of climate models becomes indispensable for projecting future scenarios, facilitating the adaptation and mitigation efforts and developing risk management strategies.

The assessment of a model's capability in accurately replicating the

recent past climate stands as a preliminary and critical step of model validation, before using the model for future projections. The analysis conducted in chapter 3 has been replicated to assess Elevation-Dependent Precipitation Change (EDPC) using the historical experiment of CMIP6 models across five distinct key mountain regions (Tibetan Plateau, Greater Alpine Region, US Rockies, and Andes - both tropical and subtropical), analyzing various ETCCDI precipitation indices spanning the period from 1950 to 2014. Initially, the analysis has been performed using the CMIP6 model ensemble-mean (MEM) to examine the representation of shared features across all models. Then, selecting the R10mm index as a reference, a comparison between the CMIP6 models, their ensemble-mean and ERA5 has been performed. Finally, to assess the capability of each model in reproducing the elevation-dependency of extreme precipitation changes, a k-mean cluster analysis has been computed on the binned altitudinal profiles of the R10mm trend, in order to identify which models better performs compared to ERA5 reanalysis.

In the Tibetan Plateau, the CMIP6 MEM reveals a positive stratification of extreme precipitation changes with the altitude. This overall gradient results from a drying effect (negative trends) at low altitudes and a wetting signal (positive trends) at high altitudes. These findings are supported by the analyses conducted with ERA5 (Chapter 3), ERA5deg, as well as existing literature (Hu et al., 2021). Some high-resolution models (CESM2, EC-Earth3, EC-Earth3-Veg) exhibit a closely similar elevational profile of the R10mm trend with respect to ERA5, albeit affected by a positive bias at all altitudes.

In the Greater Alpine Region, the application of CMIP6 MEM revealed no significant altitudinal dependency in most indices changes (except CWD), in contrast to the results obtained with ERA5. When degrading ERA5 to a coarse resolution, the EDPC signal seems to disappear; in fact, ERA5deg shows an altitudinal profile perfectly compatible with CMIP6 MEM and all CMIP6 high-resolution models, as shown by the cluster analysis. It is important to note that the overall trend distribution above 500 meters comprises very few grid points, underscoring the crucial impact of spatial resolution in simulating extreme precipitation in a relatively small region. Models that can better represent values of long-term mean intense precipitation are also clustered together in group #2 (EC-Earth3 and GFDL family model).

This cluster's shape closely resembles ERA5, albeit affected by a positive bias, as observed in the TP.

In the US Rockies, the CMIP6 models and their MEM, show a positive and significant EDPC signal, indicating a larger increase in extreme precipitation at high altitudes. In contrast, ERA5deg, similarly to what was found with ERA5, shows a linear and negative R10mm trend elevational gradient, attributed to an intensified drying effect at high altitudes. Further investigations are necessary to understand the origin of this difference.

In the tropical and subtropical Andes, the CMIP6 models exhibit notable differences when compared to the results obtained with ERA5. Considering the CMIP6 MEM, a positive altitudinal gradient is observed for several ETCCDI indices in the tropical Andes (ANN), whereas a non-significant EDPC signal is noted for the subtropical Andes (ANS). On the contrary, using ERA5 at its original spatial resolution, a non-significant signal of stratification is identified for the ANN, while a more complex pattern emerges in the ANS, featuring positive (negative) and significant stratification above (below) 2000 meters. Altering the spatial resolution of ERA5 reveals no substantial differences in the EDPC signal in the ANN, while a significant damping effect is evident in the ANS. Moreover, comparing each CMIP6 model to ERA5, many models encounter challenges in accurately representing the R10mm long-term mean, particularly in the tropical area. High-resolution models seem to exhibit slightly better performance, except for CMCC-ESM2, CMCC-CM2-SR5 and TaiESM, which perform worse than lower resolution models. Analyzing the altitudinal profiles of clusters, it is observed that, in the ANN below 3000 meters, no model closely resembles ERA5. However, models included in cluster #1 (EC-Earth3, EC-Earth3-CC, EC-Earth3-Veg, GFDL-ESM4) exhibit compatible values of binned trends above this threshold. Similarly, when considering cluster #3 (EC-Earth3, EC-Earth3-CC, EC-Earth3-Veg, GFDL-CM4, and GFDL-ESM4) for the ANS, several models demonstrate a compatible altitudinal profile within the error bars of ERA5deg, albeit affected by a positive bias, as observed in the TP and in the GAR.
The Andes are a very narrow mountain chain, thus model resolution can play a crucial role. The analysis performed with ERA5 at its original resolution (0.25° latitude-longitude, chapter 3) has revealed

distinct altitudinal stratification depending on the side of the mountain chain, in both the tropical and subtropical regions (Figure 3.13). Notably, separating the eastern and western sides of the Andes is crucial for understanding the observed distribution patterns and binned altitudinal profiles. The finer resolution facilitates a clear separation of these aspects, as shown by the ERA5 R10mm trend distribution (panel (g) and (i), Figure 4.2) that portrays two almost symmetric distributions, with positive (negative) values corresponding to the western (eastern) side of Andes. This separation can not be clearly appreciated when we degradate ERA5 at a lower resolution (panels (h) and (j), Figure 4.2). Moreover, this analysis becomes impracticable when using coarser resolutions, due to the limited number of pixel for each side. Consequently, the discrepancy observed in the profiles, might be attributed to the models' inability to capture the different behaviors exhibited on the western and eastern side of the Cordillera.

In general, our analysis reveals that, across the majority of the considered regions, high-resolution CMIP6 models outperform those characterized by coarser spatial resolutions in accurately simulating both long-term mean and temporal trends of extreme precipitation. Nevertheless, certain regions, such as the Andes, present a significant uncertainty across nearly all CMIP6 models. When using ERA5 as a reference dataset, certain models demonstrate better performance in simulating extreme precipitation and its altitudinal dependency, such as EC-Earth3, EC-Earth3-CC and EC-Earth3-Veg, GFDL-CM4 and GFDL-ESM4. It is noteworthy that the EC-Earth3 model family possesses the finest resolution and employs the same atmospheric module as ERA5. The GFDL family also features high resolution. Further investigation is required to discern the specific characteristics of these models that differentiate them from the others and contribute to their good performance.

The capability of models to reproduce extreme precipitation becomes significantly lower when rainfall is associated with local mechanisms. It has been assessed that in complex orography regions, localised convection is an incredibly important element (Giorgi et al., 2016), so that just high resolution, convection-permitting models (Hamouda and Pasquero, 2021) are able to include their structure. Although the CMIP6 models have shown significant improvement over the previous generation of CMIP5 models (Lei et al., 2023), there are still large

uncertainties in simulating regional and mountainous intense and extreme precipitation that needs to be improved.

# Chapter 5

# Conclusions and future perspectives

In this thesis, I presented my contribution to deepen current knowledge on extreme precipitation. Firstly, by exploiting an approach that seeks to reduce model uncertainties in future projections, with attention to specific aspects of the hydrological cycle. Secondly, by analysing how extreme precipitation, which indeed is a key aspect of the changing hydrological cycle, is represented in reanalysis data and state-of-the-art climate models in mountainous areas. The main outcome of the previous chapters are summarised here below, with a broader view and a look at future work.

## 5.1 Summary and concluding remarks

***Emergent Constraints.*** In the first PhD year, we applied the Emergent Constraint (EC) technique to model projections of precipitation, one of the variables most affected by model uncertainties and still insufficiently explored within the context of ECs, particularly for the recent CMIP6 model ensemble. We tested previously documented precipitation ECs, originally evaluated with CMIP3/CMIP5 data, by evaluating their existence and robustness using different subsets of CMIP5 and CMIP6 models and exploring the sensitivity to the ensemble composition. Our results show that most precipitation ECs considered so far do not "survive" to a change in the model ensemble and ensemble composition. The main findings and conclusions of our analysis are listed below:

1. When a new EC is proposed, it is fundamental to provide a robust physical description and explanation of the relationship between

the variables involved and associated mechanisms. Special attention is required when the EC variables are related through feedbacks or pertain to different climate regimes; in these cases, assessing a simple linear relationship that describes the EC and at the same time is able to effectively narrow model uncertainties becomes a very challenging task.

2. Exploring ECs at the local scale could be a more effective approach. Aggregating or averaging different geographical areas, in fact, may pose challenges, as these regions can differ significantly from one another in terms of climatological regimes, large-scale and local mechanisms. Such discrepancies may pose a limitation in applying ECs, given that these differences have the potential to impact the overall model performance, in both historical simulations and future projections.

3. In general, the practical application of the EC technique for reducing uncertainties in model projections should be regarded with caution. The remarkable sensitivity of the EC method to the model ensemble composition represents a weakness of the technique. A fruitful application of the technique could lie in the ability to describe climate phenomena, and to investigate connections between different climate variables.

Considering the limitations of the EC technique that have been highlighted, it is important to explore what can be done to improve its robustness for evaluating new ECs. Furthermore, it would be interesting research to explore alternative methodologies to narrow these uncertainties.

***Elevation-Dependent Precipitation Change in ERA5.*** In this part of the thesis, we performed a global comparison of changes in mean precipitation and precipitation extremes between key global mountain areas (the Tibetan Plateau, the US Rocky Mountains, the Greater Alpine Regions, and the Andes) focusing on their dependency on elevation, using the ERA5 global reanalysis dataset. The elevational gradient of temporal trends over the period 1951–2020 of mean precipitation and several ETCCDI extreme precipitation indices was investigated, both averaged on altitudinal bins and considering the overall distribution across individual pixels. Our analysis revealed the presence of an EDPC signal in most of the mountainous areas considered. Our main findings are summarised below:

1. Mean precipitation, extreme precipitation (R10mm) and length of consecutive wet days (CWD) show a consistent behavior in every area in terms of elevational dependence of their trend

2. The overall elevation dependency (EDPC) can be described by a simple linear regression approach in the Alps and in the Rockies but it can be largely misleading in the Tibetan Plateau and the Andes.

3. The Tibetan Plateau, the Greater Alpine Region and the western side of the Andes show a wetting effect (positive trends) at high altitudes, respectively 4000, 1500 and 3500 meters.

EDPC results from a combination of various physical processes, competing phenomena and climate feedbacks and it might be influenced by local factors, general atmospheric circulation dynamics or by thermodynamic drivers. The similarity of EDPC patterns across different areas suggests that some of those drivers may be generalised, as found for the Elevation-Dependent Warming.

***CMIP6 historical EDPC evaluation*** In the last part of my PhD research, we evaluated CMIP6 models' capability to accurately simulate the recent past Elevation-Dependent Precipitation Change within the same five mountain regions described above, analysing ETCCDI extreme precipitation indices spanning the period 1950 to 2014. CMIP6 models and their ensemble-mean (MEM) were compared to ERA5 in order to identify which models exhibit better performances in simulating R10mm trends and their altitudinal stratification and highlighting regional differences. Below, we present the main outcome of our analysis and we summarise our key conclusions:

1. Spatial resolution has a significant impact on model performance in simulating extreme precipitation and its altitudinal stratification, particularly in small or extremely narrow mountain areas such as the Greater Alpine Region or the Andes. In general, higher resolution CMIP6 models, such as EC-Earth3 or GDFL, have shown the best results.

2. In the US Rockies and in the tropical Andes, models display markedly distinct behaviors compared to ERA5. In the former case, these differences emerge when analyzing temporal trends, whereas in the Andes, models encounter challenges also in accurately simulating the R10mm long-term climatological mean.

3. In the Tibetan Plateau, in the Greater Alpine Region, and in the subtropical Andes, a positive bias has been identified, indicating that models exhibit larger trend values compared to ERA5.

If one sets the goal of conducting more extensive validation of historical model simulations for the EDPC, the results presented in this section could be integrated with further comparisons, considering other datasets taken as a reference, possibly high-resolution global datasets based on observations or reanalyses. Particular attention should be paid to the regions that, in our study, have shown the greater discrepancies between ERA5 and CMIP6 models, such as the Rockies and the Andes. Secondly, a further natural step to expand this analysis involves looking at the EDPC signal in future model projections, analysing whether altitudinal patterns that have emerged in the recent past, may exist or undergo changes in the future.

## 5.2 Future perspectives

Our work provides some insights, summarised in the previous section, and raises some questions addressed to the scientific community. An extensive methodology to identify which variables might be regarded as primary drivers of the Elevation Dependent Warming has already been assessed in the literature (e.g. Pepin et al., 2015). Future studies should focus on adapting this methodology to the Elevation Dependent Precipitation Change (EDPC). As previously discussed in chapters 3 and 4 and in the literature, EDPC drivers could be divided into three categories: Thermodynamical, Dynamical, and Microphysical drivers (Houze, 2012). **Thermodynamical drivers** may exhibit common characteristics across various mountainous regions, regardless of distinct climatological or geographical features. The altitudinal gradient of precipitation and its extremes is strongly related to changes in the surface energy balance. As a consequence, snow-albedo feedbacks, atmospheric moisture, thermal emission, aerosols, and clouds and their relationship with EDPC should be investigated in more detail. Nevertheless, different influences may arise due to morphological factors, such as slope and exposure, leading to changes influenced by local topography. **Dynamical** EDPC **drivers** are related to the atmospheric circulation across very different spatial scales. The complex interaction between synoptic flow and orographically induced circulations contributes significantly to the variability in the elevational distribution of precipitation. In the midlatitudes, alterations in pre-

cipitation patterns over mountainous regions may be influenced by planetary waves and the Jet Stream, impacting e.g. the Rockies or the northern area of the Tibetan Plateau (Pepin et al., 2022). Another example is represented by the North Atlantic Oscillation (NAO), as it might represent a potential factor affecting intense precipitation changes over the Alps, influencing the availability of moisture during winter and local convective structures during summer (Napoli et al., 2023). Furthermore, the orography of mountainous regions can induce modifications also in meso- and micro-scale circulations, driven by slope winds and their enhanced windward ascent in a warmer climate (Pepin et al., 2022). Additionally, specific studies should focus on investigating the role of the air column stability in affecting convection patterns. Finally, a comprehensive exploration of the impact of **aerosols** on extreme orographic precipitation change and its altitudinal stratification needs to be performed. Another interesting aspect that still needs to be better investigated involves the impact of **land use** on both precipitation extremes and their correlation with orography, particularly through afforestation and urbanization. On the one hand, alterations in the tree line altitude caused by warming may represent a driver for EDPC, due to shifts in humidity exchanges or changes in the albedo feedback. Consequently, the examination of vegetation indices, such as the normalized difference vegetation index (NDVI), and their correlation with elevation-dependent variations in temperature and precipitation may represent an important research application (Li et al., 2015). On the other hand, a more in-depth investigation needs to focus on the role of urbanization in mountainous areas, as it has been identified as a key factor contributing to the enhancement of both frequency and intensity of extreme rainfall over the past century (e.g. Yang et al., 2014).

In this context, the EC technique might be regarded as a valuable approach to assess the EDPC drivers owing to its capability to connect various climate variables in recent historical data and future projections. An interesting future perspective of this study could be exploring the applicability of the concept proposed by the Emergent Constraint technique to regional climate models, possibly overcoming the challenges associated with spatial resolution and the uncertainties related to the parameterization of sub-grid climatic processes.

# Appendices

# Appendix A

# Emergent Constraints

Here we discuss the additional information that have not been reported in the main text of chapter 2. Moreover, further considerations about the assessment of new ECs for extreme precipitation in mountain areas have been discussed.

## A.1 CMIP5 bootsrap models

As mentioned in the main text, for this specific EC a different bootstrap analysis was performed on a larger set of 39 CMIP5 models, using subsets with the same number of GCMs as in our initial CMIP5 ensemble (27 models, listed in Table 1 of the main text). The 12 added models are shown in Table S1. The results of the bootstrap analysis, in terms of probability distribution of correlation coefficient, is shown in Figure 2.3.

## A.2 Further considerations about the assessment of new ECs for extreme precipitation in mountain areas

Given the weaknesses of the Emergent Constraints outlined in this study, which were proposed and used in previous studies, we have tried to evaluate a new EC, specifically devised to study extreme precipitation in high-altitude regions. As a first step, we put a focus on a specific region, rather than perform aggregation of diverse areas, as recommended in the ECB discussion. Secondly, we decided to employ the same variable for both the predictor and the predictand, in line with the insights pointed out by the analysis of ECG. We

**Table S1:** Additional CMIP5 models considered for the bootstrap analysis of ECL. The full set (39 models) consists of the these models and the ones listed in Table 1 of the main text.

| Model name | Institution name |
|---|---|
| BNU-ESM | BNU |
| CMCC-CESM | CMCC |
| CMCC-CM | CMCC |
| CMCC-CMS | CMCC |
| FIO-ESM | FIO |
| GFDL-CM3 | NOAA-GFDL |
| GISS-E2-H-CC | NASA-GISS |
| GISS-E2-H | NASA-GISS |
| GISS-E2-R-CC | NASA-GISS |
| GISS-E2-R | NASA-GISS |
| HadGEM2-AO | MOHC |
| NorESM1-ME | NCC |

attempted to identify a robust EC linking the inter-model spread in projected future extreme orographic precipitation changes across the Greater Alpine Region to a current climate predictor, possibly associated with temperature increases in climate change scenarios. However, no significant relationship emerged between the selected predictand and the inter-model spread across various climate variables examined for the predictor, including precipitation extremes (ETCCDI indices - same as predictand), temperature change, temperature trend, and hydrological sensitivity. Considering the relatively limited size of the Alpine region, compared to the spatial resolution of CMIP6 models, and acknowledging the challenges faced by coarse resolution models in simulating extreme precipitation, particularly in mountain areas (see Section 1.3.2), we broadened our investigation, beginning with an exploration of the Tibetan Plateau.

Several variables have been evaluated over the region of the Tibetan Plateau [25-40°E; 70-105°N]. Here we reported as an example, one of the relationships that has been found with CMIP6 models. In this case, the predictor that has been identify is defined as the R99pTOT index ($[mm/year]$ - annual total precipitation exceeding the 99th percentile threshold on wet days evaluated over the 1961–1990 reference period) normalised by local-mean surface air temperature $[^{\circ}C]$, averaged over the period 1960–1999. The predictand is represented by the same variable averaged over the period 2060–2099 of ssp585 scenario. Figure A.1 displays the scatterplot between the predictor and the pre-

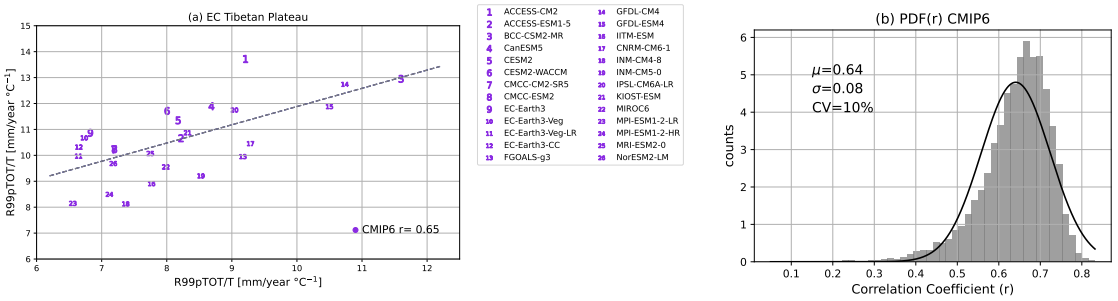


**Figure A.1:** Analysis of new EC over the Tibetan Plateau region. (a) Scatterplot of the predictand (mean R99pTOT normalised by local-mean surface air temperature ) – $[mm/year\,^{\circ}C^{-}1]$) against the predictor (same variable) for CMIP6 model ensemble. The dashed line shows the ordinary least-squared best fit. (b) Probability distribution of the correlation coefficient for the bootstrap analysis of the EC CMIP6 models.

dictand calculated using CMIP6 models, while panel (b) illustrates the bootstrap analysis performed to assess the robustness of the relationship to variations in the model ensemble (refer to Section 2.2 for detailed information). A correlation coefficient of 0.65 (p-value$\leq$0.05) was identified, and the bootstrap analysis computed a distribution with a standard deviation of 0.08 (mean value of 0.64), affirming the robustness of the identified EC.

This relationship connects the historical climatological long-term mean value of extreme precipitation with its future projections. When attempting to identify an EC within the same area using as predictor and predictand the temporal trend or change of extreme precipitation respectively in the past and in the future, no robust EC can be established. While there is more consensus concerning the long-term mean and in the sign of heavy precipitation change, the real challenge lies in narrowing the significant uncertainties that persist in projecting the magnitude of future changes in precipitation extremes (Thackeray et al., 2022). Further investigation is warranted to gain a comprehensive understanding of the situation.

# Appendix B

# EDPC with ERA5

Here I reported the additional plots that have not been included in the main text of chapter 3

## B.1 Mountain areas

The following plots show the seasonal geographical distribution of R10mm index for each of the mountain areas considered in chapter 3.

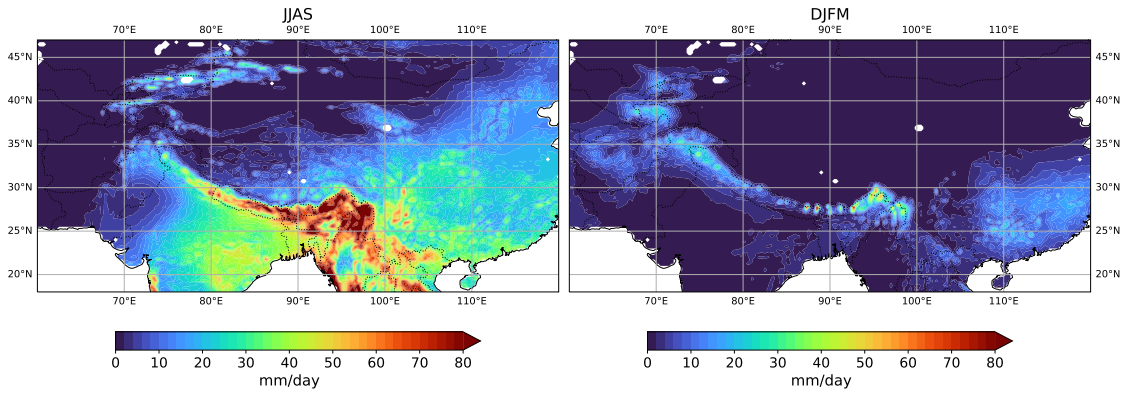


**Figure B.1:** Map of the geographical distribution in the Tibetan Plateau area of extreme precipitation (R10mm index, *days*) evaluated with ERA5 over the 1951-2020 period in summer (JJAS) and winter (DJFM) seasons

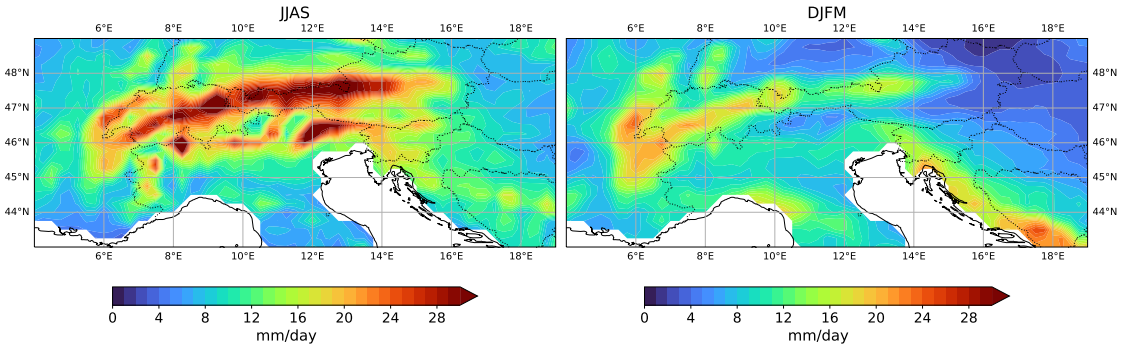


**Figure B.2:** Map of the geographical distribution in the Greater Alpine Region of extreme precipitation (R10mm index, *days*) evaluated with ERA5 over the 1951-2020 period in summer (JJAS) and winter (DJFM) seasons

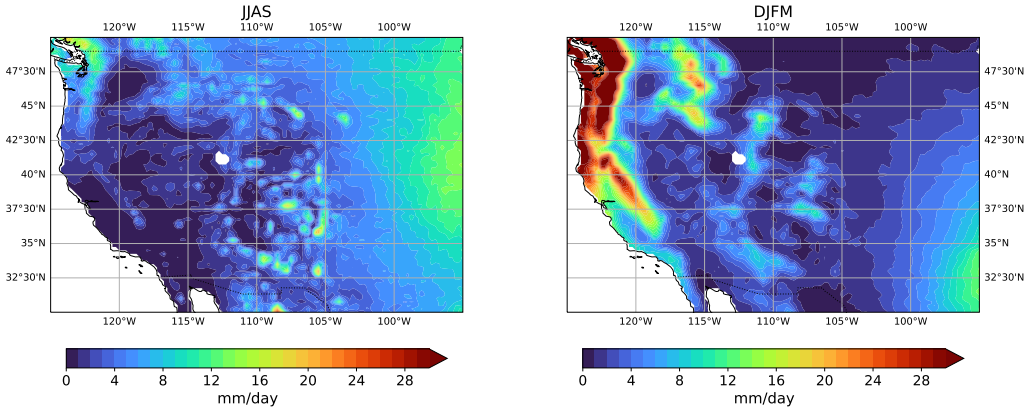


**Figure B.3:** Map of the geographical distribution in the US Rocky mountain of extreme precipitation (R10mm index, *days*) evaluated with ERA5 over the 1951-2020 period in summer (JJAS) and winter (DJFM) seasons

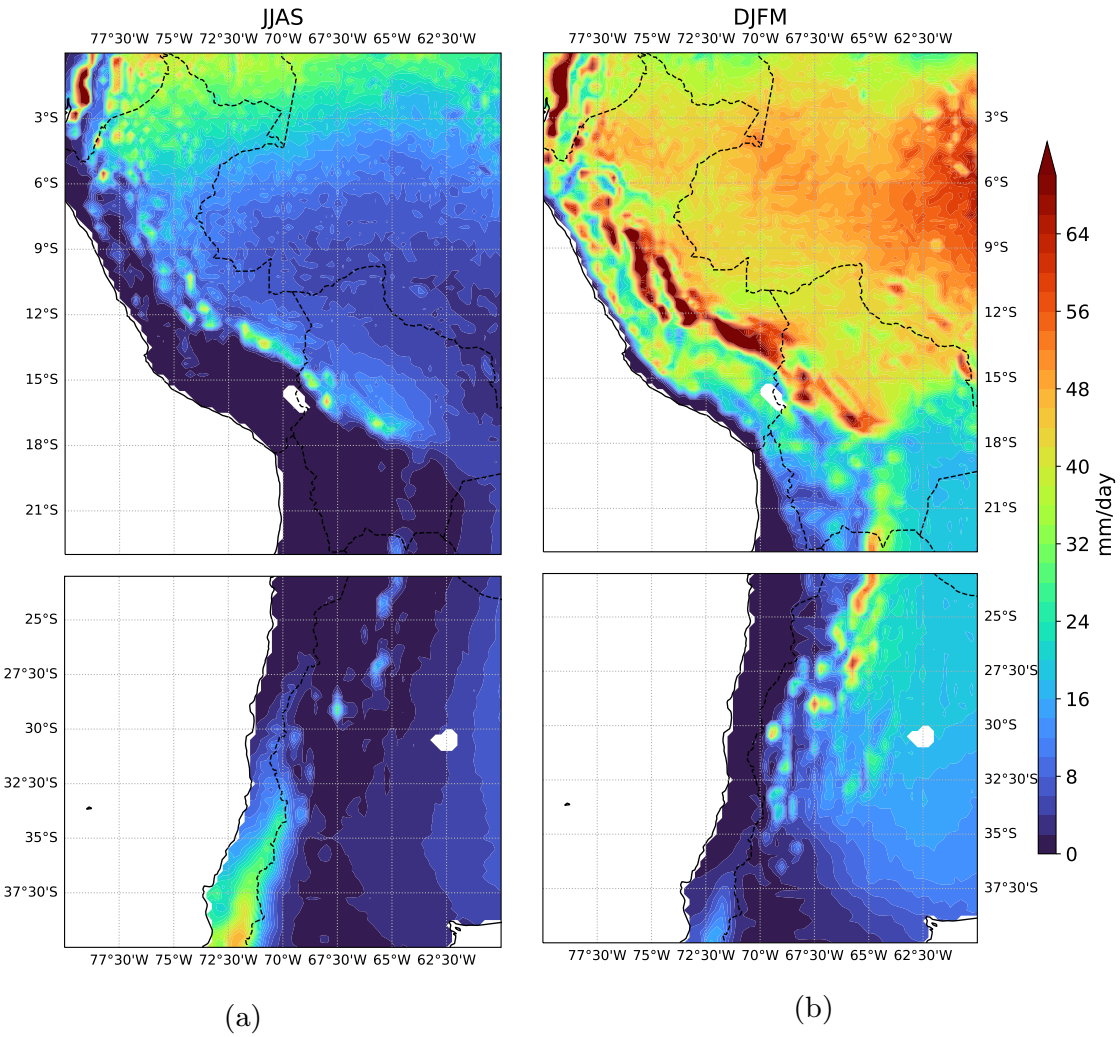


(a) (b)

**Figure B.4:** Map of the geographical distribution in the Andes of extreme precipitation (R10mm index, *days*) evaluated with ERA5 over the 1951-2020 period in boreal winter (JJAS) and boreal summer (DJFM) seasons.

## B.2 Altitudinal dependency of climatological mean and extreme precipitation indices

In this section, I show the elevational dependence of climatological mean and extreme precipitation indices in the five main areas considered in this study.

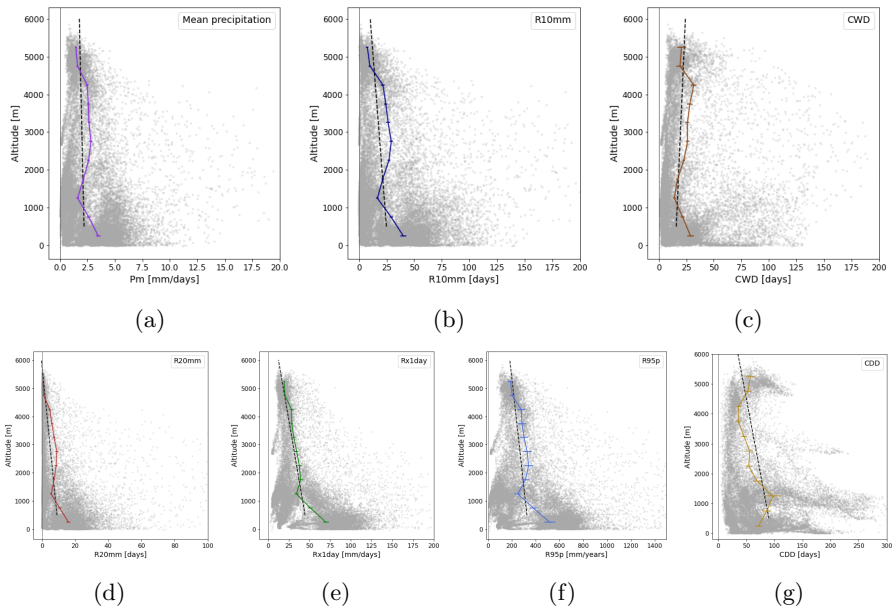


**Figure B.5: Tibetan Plateau.** Elevational dependence of climatological mean of precipitation indices (see labels) for the TP. Each panel shows the vertical profile of spatially averaged binned data (top scale) superimposed to the distribution of trends of individual grid points (grey, bottom scale). Vertical profiles include errors on the trend and the significance of the trend (filled squares when $\geq$95%). Point distributions are accompanied by their linear regression (dashed line)

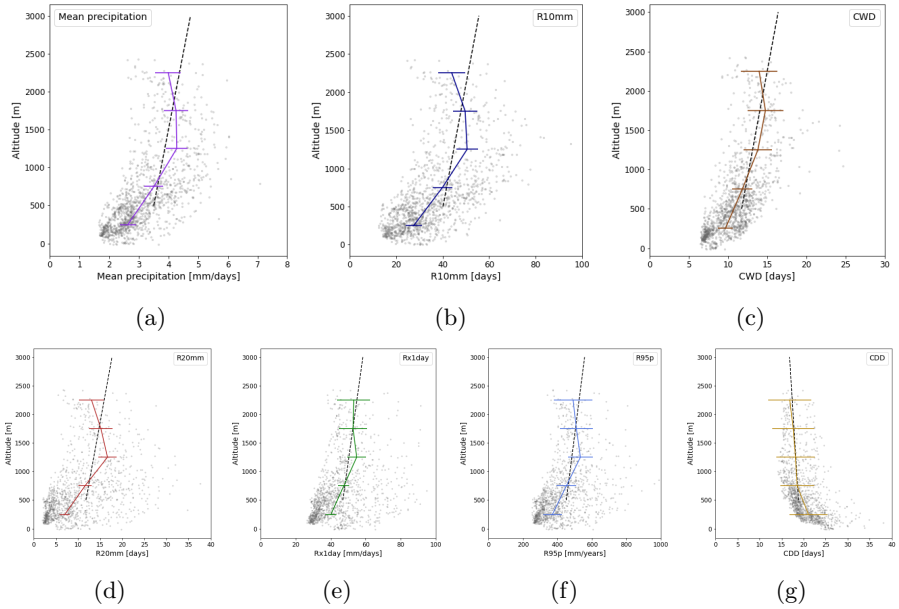


**Figure B.6:** Same as B.5 but for the **Greater Alpine Region**

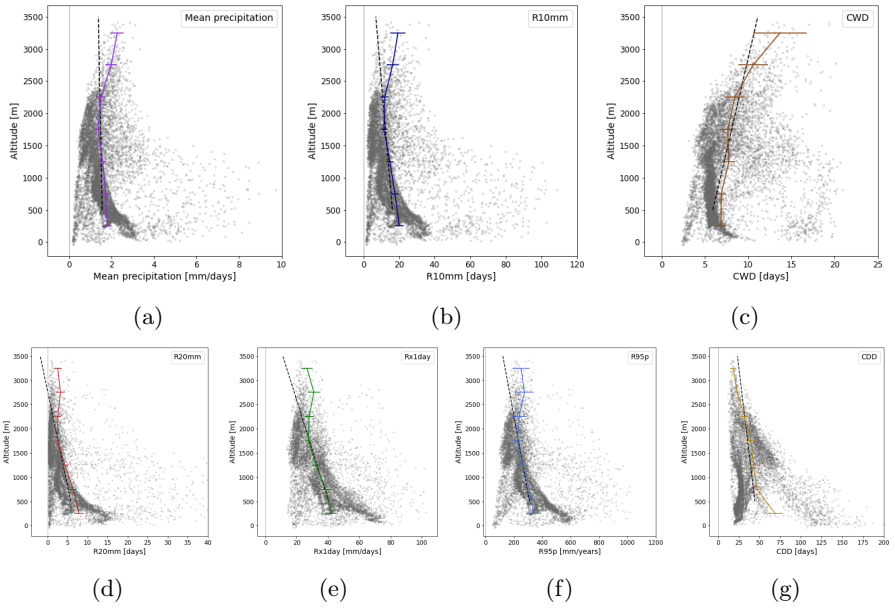


**Figure B.7:** Same as B.5 but for the **US Rockies**

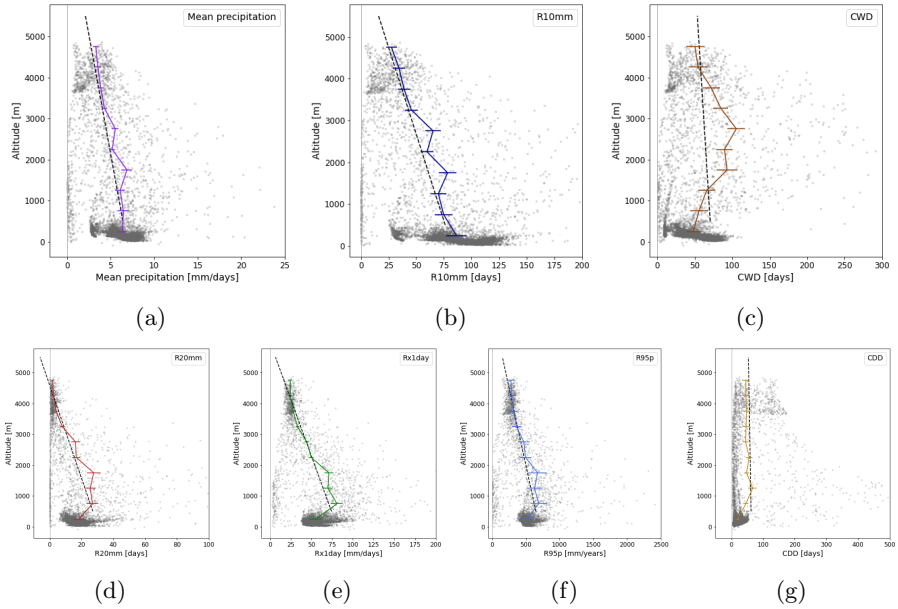


**Figure B.8:** Same as B.5 but for the **Tropical Andes**

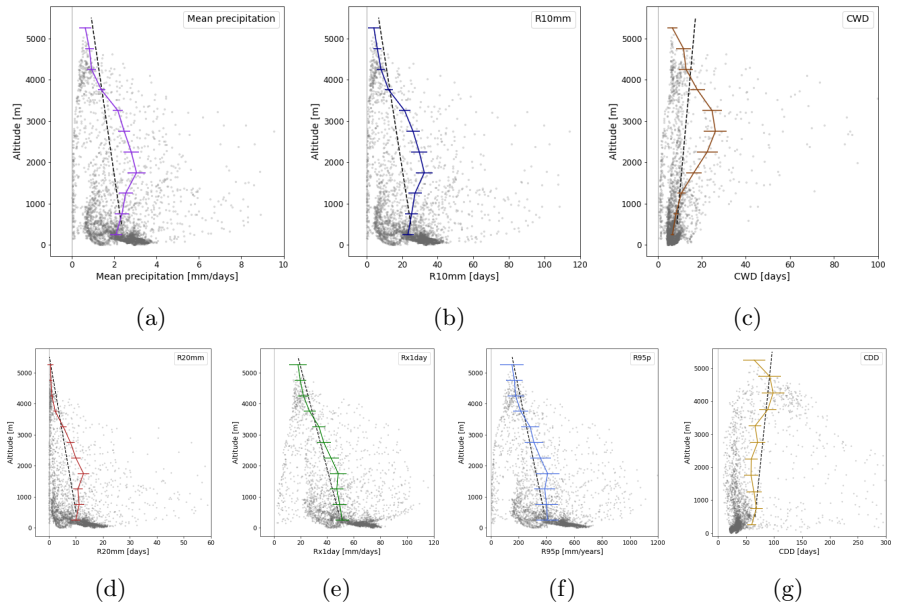


**Figure B.9:** Same as B.5 but for the **Sub-tropical Andes**

## B.3 Altitudinal dependency of temporal trends

Here I show the elevational dependence of temporal trends of extreme precipitation indices that has not been shown in the main text for each study area.

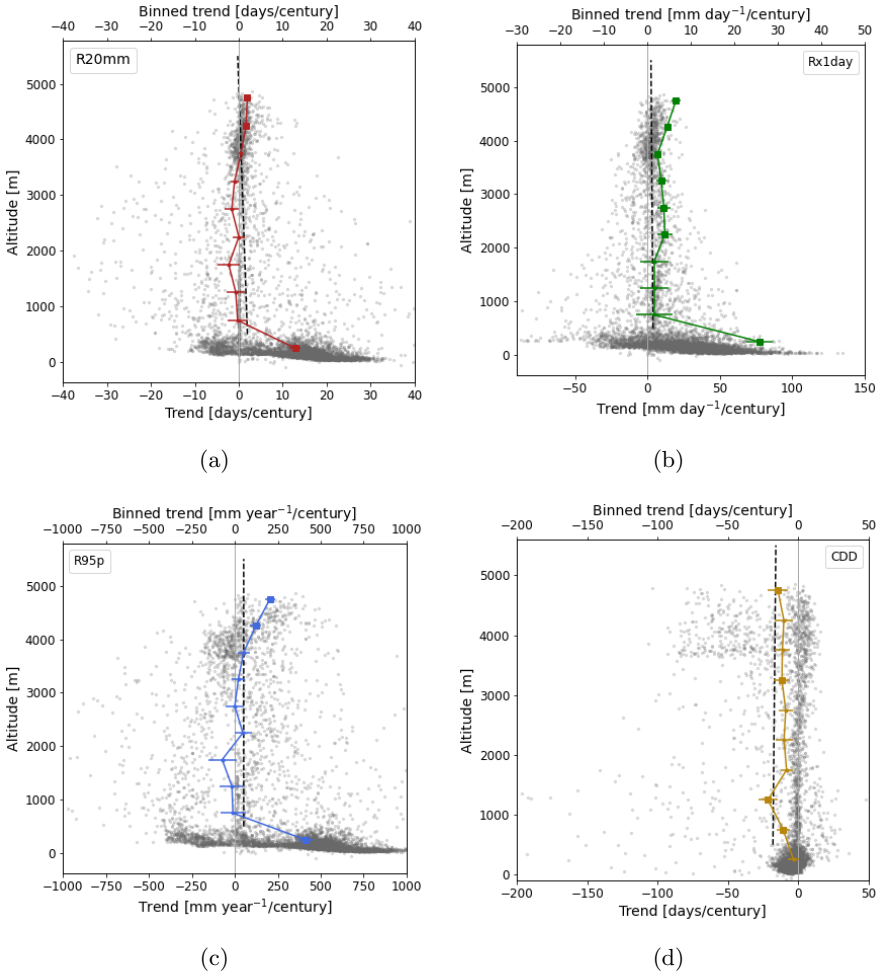


**Figure B.10: Tropical Andes.** Elevational dependence of temporal trends of precipitation indices (see labels) for ANN. Each panel shows the vertical profile of spatially averaged binned data (top scale) superimposed to the distribution of trends of individual grid points (grey, bottom scale). Vertical profiles include errors on the trend and the significance of the trend (filled squares when $\geq$95%). Point distributions are accompanied by their linear regression (dashed line). Note that the scale for vertical profiles is magnified by a factor 10.

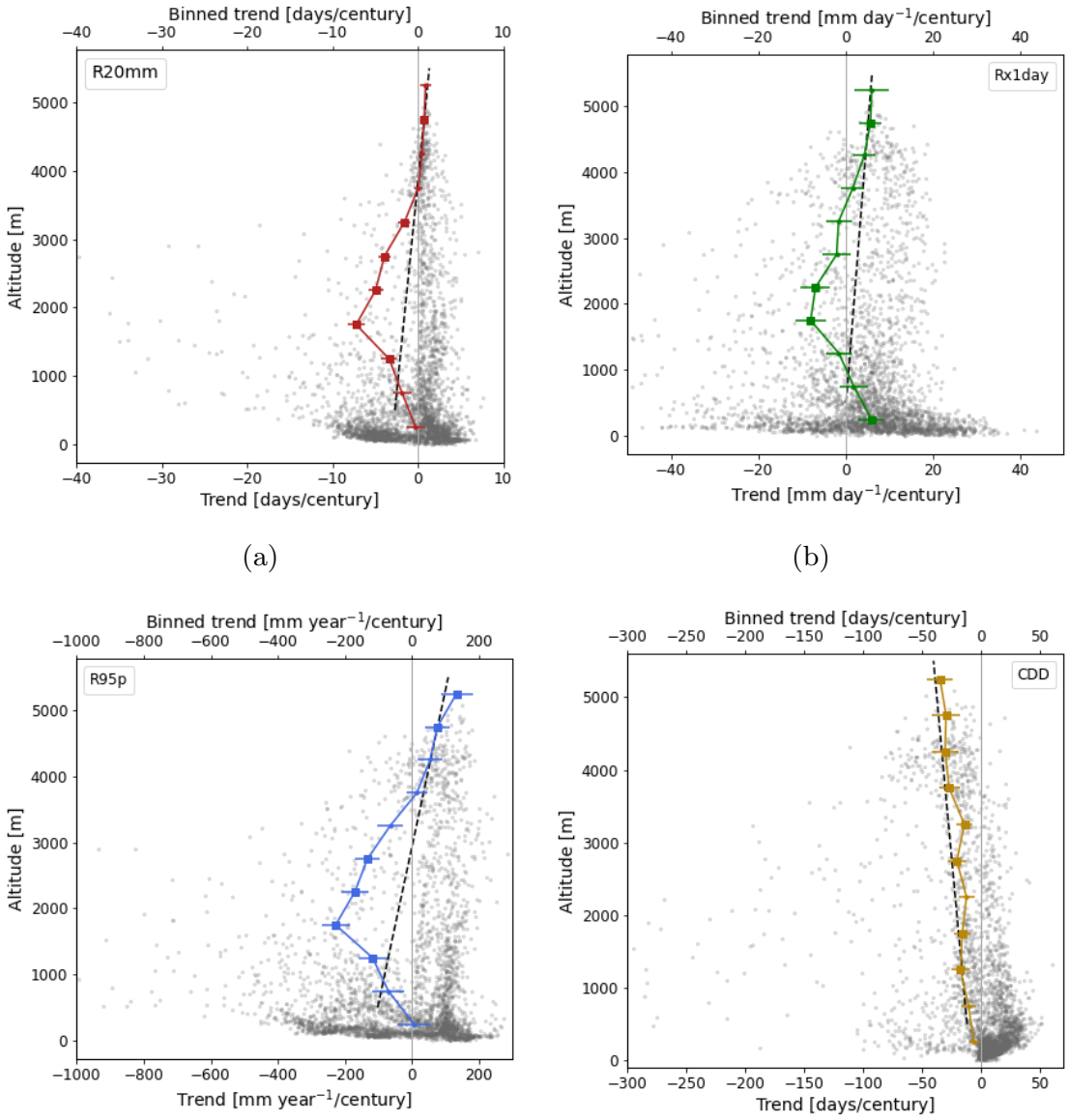


**Figure B.11:** Same as B.10 but for **subtropical Andes**

## B.4 Seasonal analysis

Here I reported the additional plots that have not been included in the main text of section 3.3.2.

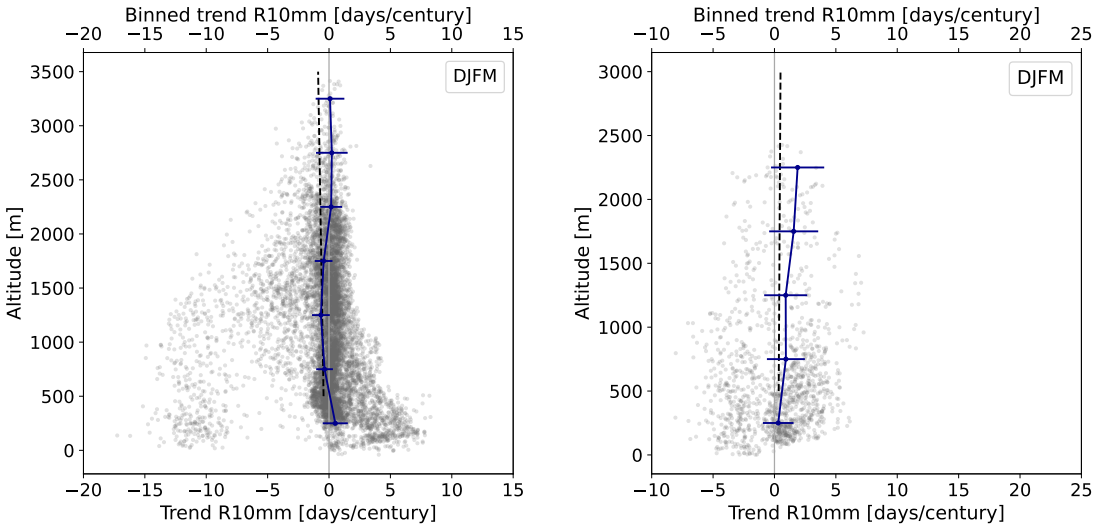


(a) US Rockies

(b) Greater Alpine Region

**Figure B.12:** Elevational dependence of temporal trends of R10mm for winter season (DJFM) for the RO (a) and the GAR (b).

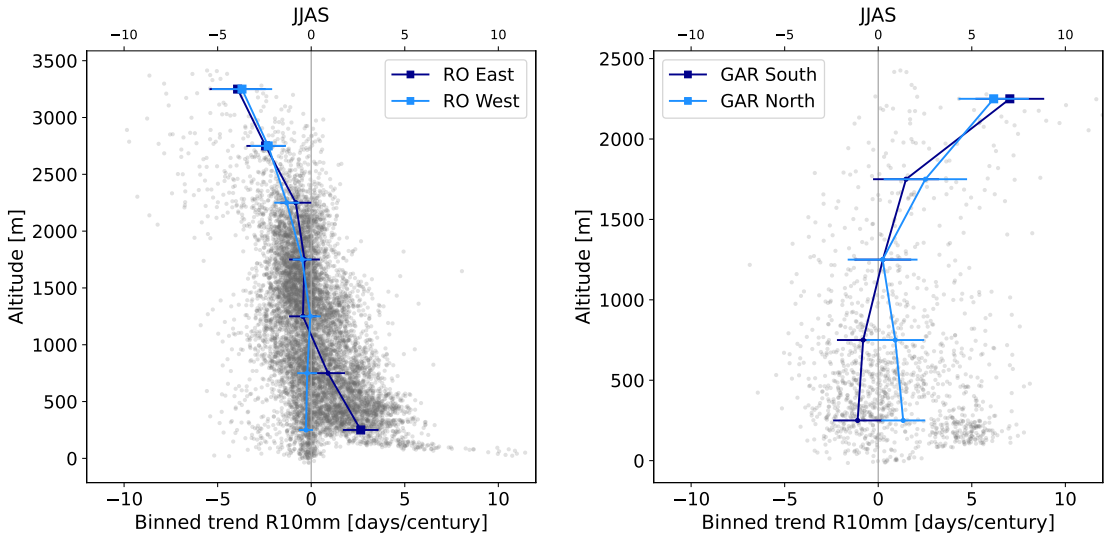


(a) (b)

**Figure B.13:** Elevational dependence of temporal trends of R10mm for summer season (JJAS) for the RO (a) and the GAR (b). For the GAR (RO), the two sides of the mountain chains have been separated along the meridional (zonal) direction.

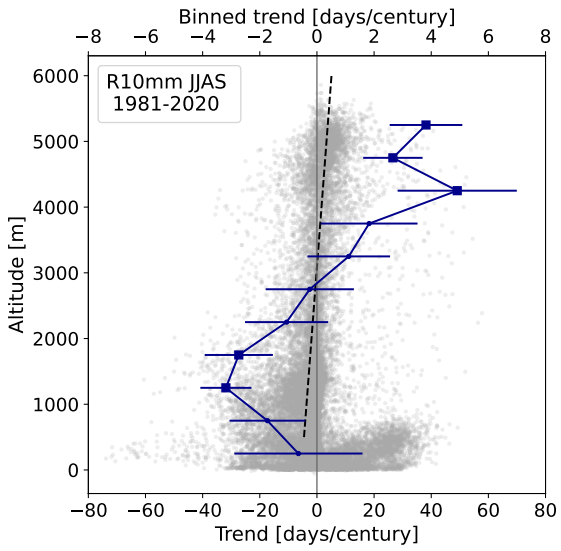


**Figure B.14:** Elevational dependence of temporal trends of R10mm for summer season (JJAS) in the Tibetan Plateau considering the period 1981–2020.

# Appendix C

# EDPC in CMIP6 models

Here I reported the additional plots that have not been included in the main text of chapter 4

## C.1 CMIP6 model ensemble mean (MEM)

Here I show the elevational dependence of temporal trends of extreme precipitation indices that has not been shown in the main text for each study area, computed with CMIP6 MEM.

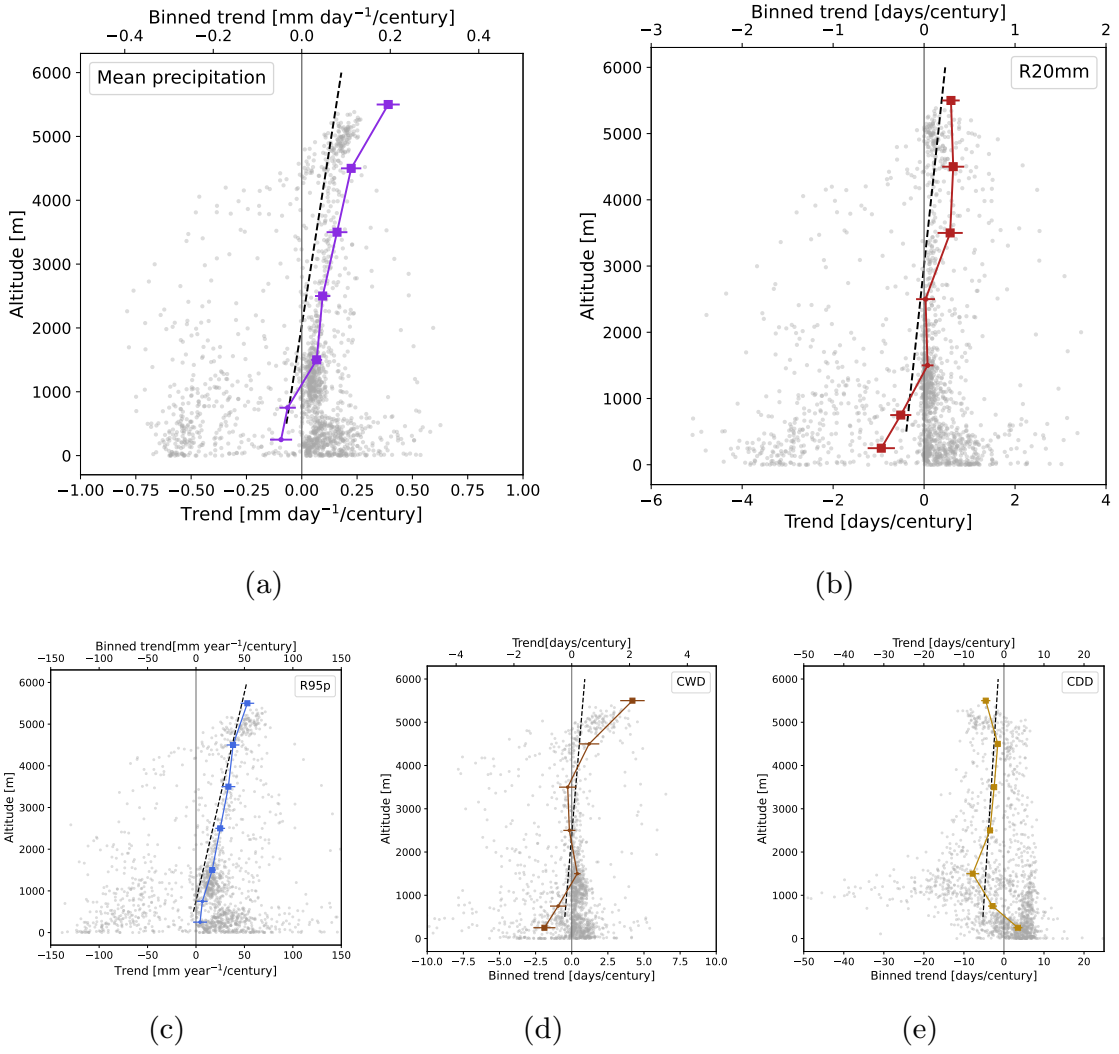


**Figure C.1: Tibetan Plateau.** Elevational-dependence of temporal trends of precipitation indices (see labels) for the Tibetan Plateu (TP) area. Each panel shows the vertical profile of spatially averaged binned data (top scale) superimposed to the distribution of trends of individual grid points (grey, bottom scale). Vertical profiles include errors on the trend and the significance of the trend (filled squares when $\geq$95%). Point distributions are accompanied by their linear regression (dashed line).

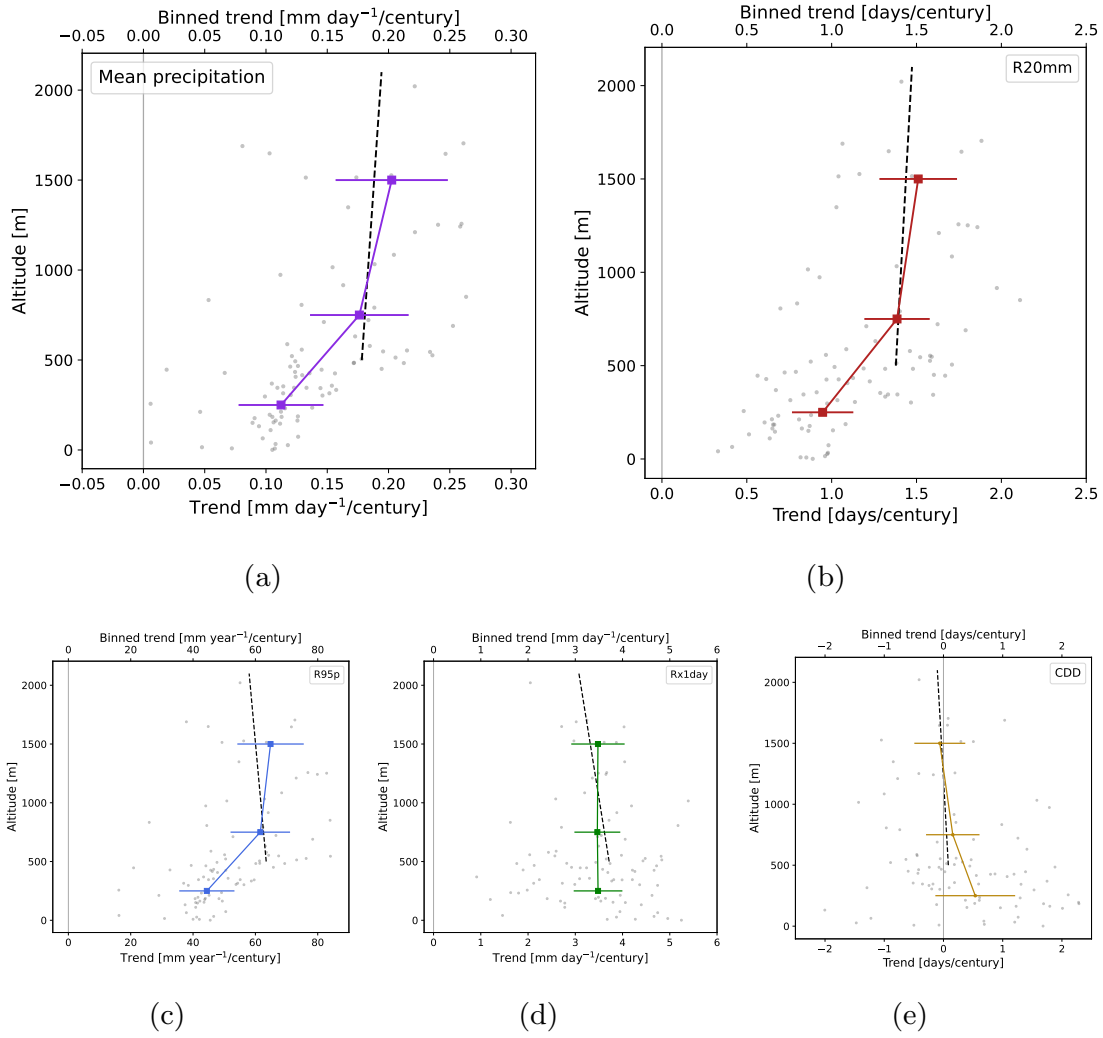


**Figure C.2:** Same as Figure C.1 but for the **Greater Alpine Region** (GAR).

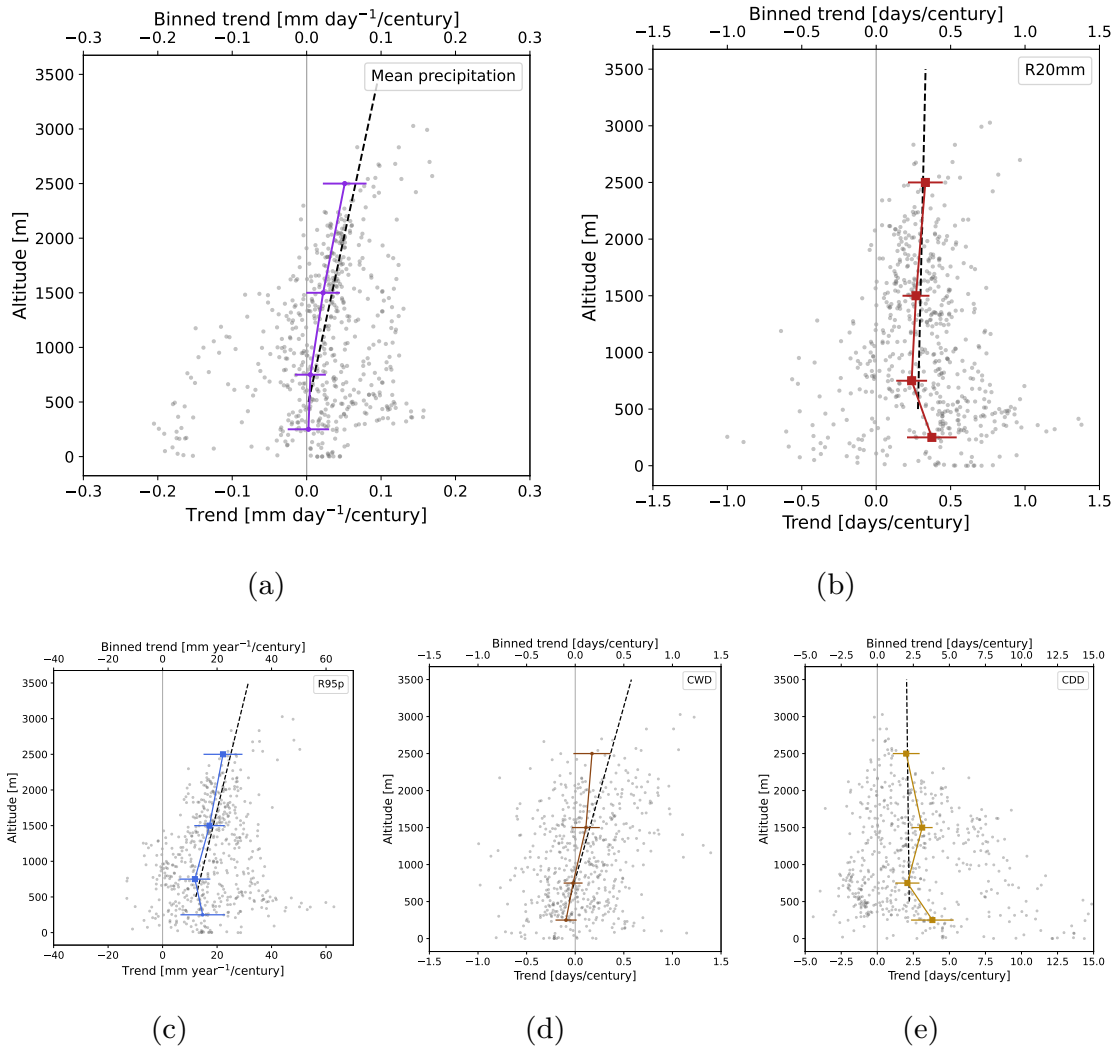


**Figure C.3:** Same as Figure C.1 but for the **US Rockies** (RO).

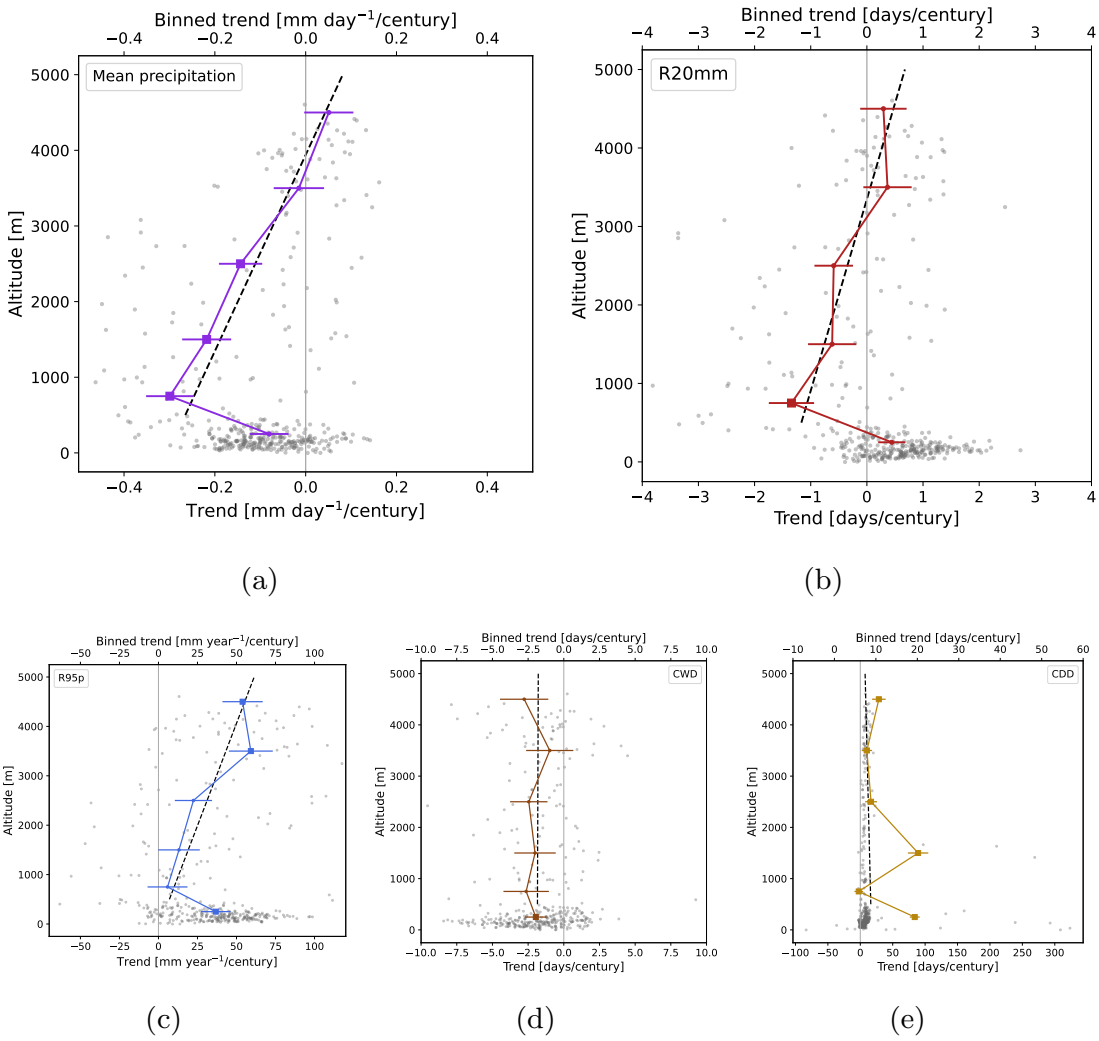


**Figure C.4:** Same as Figure C.1 but for the **tropical Andes** (ANN).

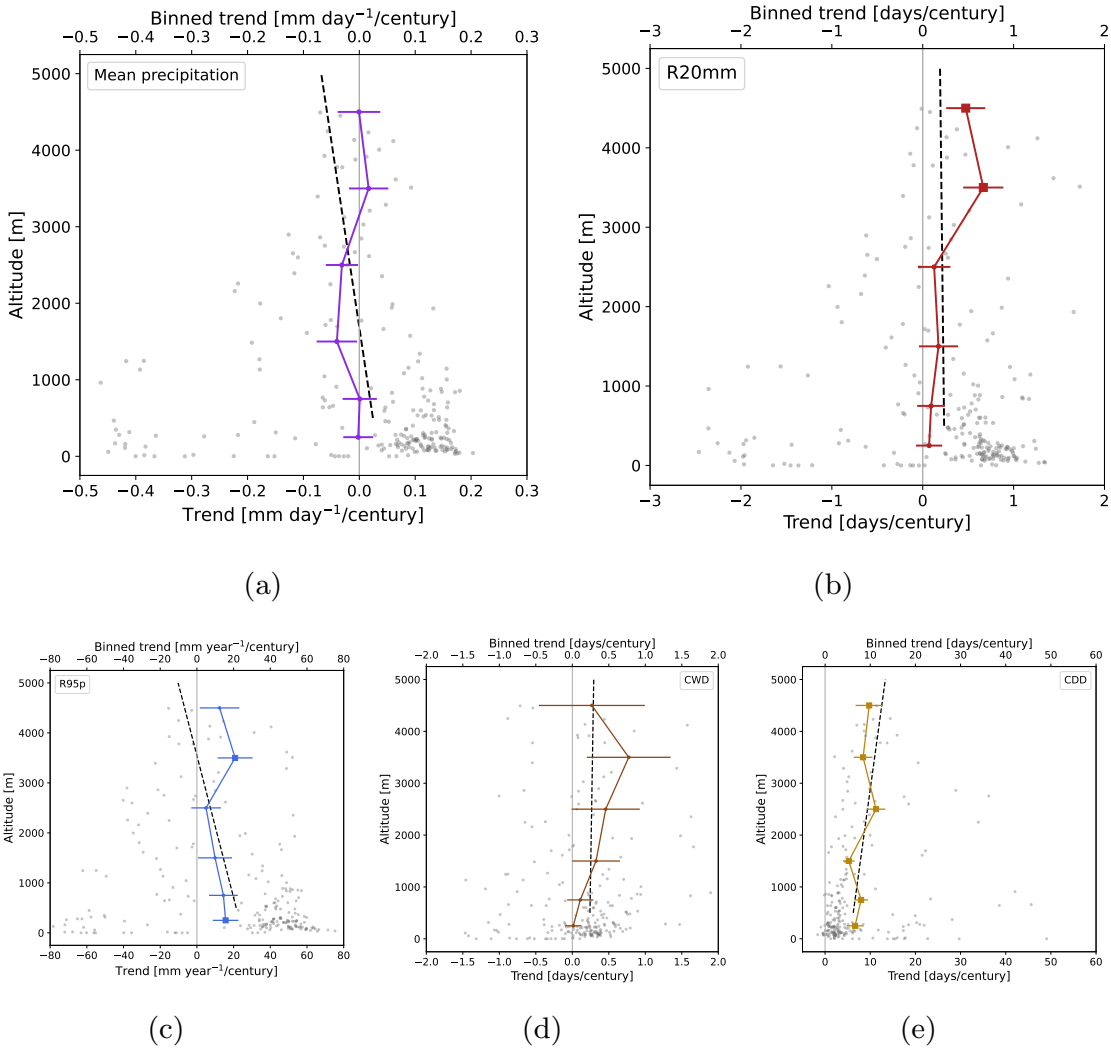


**Figure C.5:** Same as Figure C.1 but for the **sub-tropical Andes** (ANS).

## C.2 K-mean cluster analysis

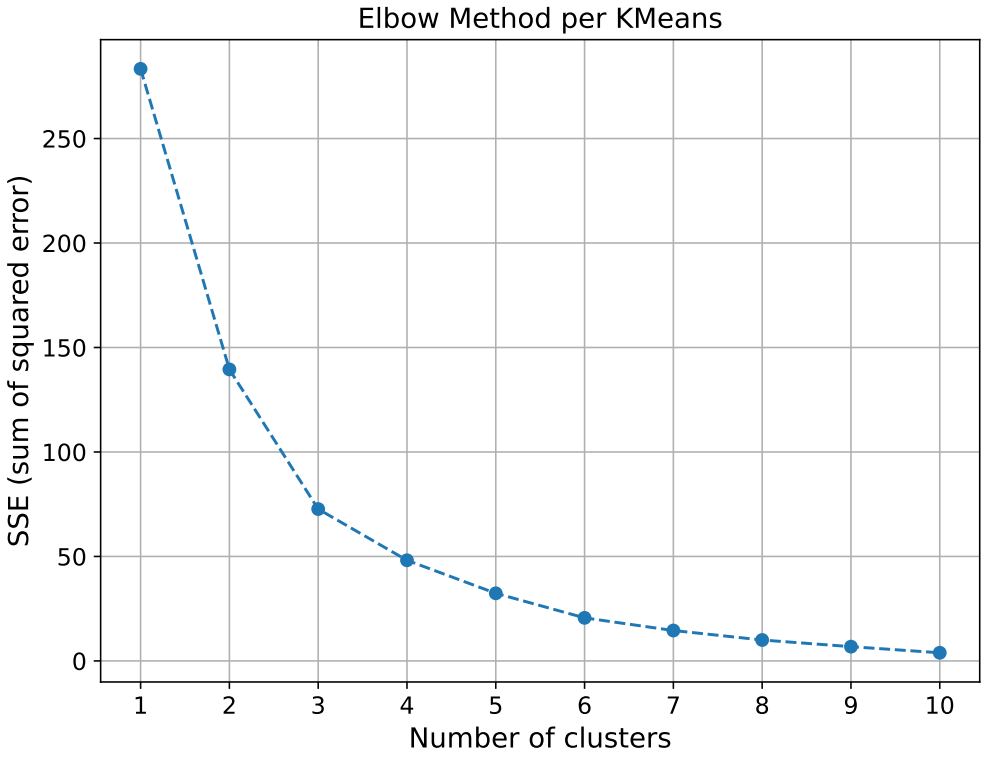


**Figure C.6:** Elbow method plot for determining optimal number of clusters for the **Tibetan Plateau** area. The plot illustrates the sum of squared errors (SSE) as a function of the number of clusters.

# Bibliography


Abbate, A., Papini, M., and Longoni, L. (2022). Orographic precipitation extremes: An application of lume (linear upslope model extension) over the alps and apennines in italy. Water, 14:2218.

Adachi, Y., Yukimoto, S., Deushi, M., and et al. (2013). Basic performance of a new earth system model of the meteorological research institute. Papers in Meteorology and Geophysics, 64.

Adcroft, A., Anderson, W., Balaji, V., and et al. (2019). The gfdl global ocean and sea ice model om4.0: Model description and simulation features. Journal of Advances in Modeling Earth Systems, 11.

Allan, R. P., Barlow, M., Byrne, M. P., and et al. (2020). Advances in understanding large-scale responses of the water cycle to climate change. Annals of the New York Academy of Sciences, 1472(1):49–75.

Allen, M. R. and Ingram, W. J. (2002). Constraints on future changes in climate and the hydrologic cycle. Nature, 419.

Arakawa, A. (2004). The cumulus parameterization problem: Past, present, and future. Journal of Climate, 17(13):2493 – 2525.

Arora, V. K., Scinocca, J. F., Boer, G. J., and et al. (2011). Carbon emission limits required to satisfy future representative concentration pathways of greenhouse gases. Geophysical Research Letters, 38.

Barry, R. G. (1981). Mountain weather and climate. Mountain weather and climate.

Bellouin, N., Rae, J., Jones, A., and et al. (2011). Aerosol forcing in the climate model intercomparison project (cmip5) simulations by hadgem2-es and the role of ammonium nitrate. Journal of Geophysical Research Atmospheres, 116.

Beniston, M. (2003). Climatic change in mountain regions: A review of possible impacts. Climatic Change, 59.

Bentsen, M., Bethke, I., Debernard, J. B., and et al. (2013). The norwegian earth system model, noresm1-m – part 1: Description and basic evaluation of the physical climate. Geoscientific Model Development, 6.

Bi, D., Dix, M., Marsland, S. J., and et al. (2013). The access coupled model: Description, control climate and evaluation. Australian Meteorological and Oceanographic Journal, 63.

Bibi, S., Wang, L., Li, X., and et al. (2018). Climatic and associated cryospheric, biospheric, and hydrological changes on the tibetan plateau: a review. International Journal of Climatology, 38(S1).

Borodina, A., Fischer, E. M., and Knutti, R. (2017). Emergent constraints in climate projections: A case study of changes in high-latitude temperature variability. Journal of Climate, 30.

Boucher, O., Servonnat, J., Albright, A. L., and et al. (2020). Presentation and evaluation of the ipsl-cm6a-lr climate model. Journal of Advances in Modeling Earth Systems, 12.

Brient, F. (2020). Reducing uncertainties in climate projections with emergent constraints: Concepts, examples and prospects. Advances in Atmospheric Sciences, 37.

Caicedo, P., Daniel, J., Arias, P., and et al. (2020). Observed and projected hydroclimate changes in the andes. Frontiers in Earth Science, 8.

Caldwell, P. M., Bretherton, C. S., Zelinka, M. D., and et al. (2014). Statistical significance of climate sensitivity predictors obtained by data mining. Geophysical Research Letters, 41.

Caldwell, P. M., Zelinka, M. D., and Klein, S. A. (2018). Evaluating emergent constraints on equilibrium climate sensitivity. Journal of Climate, 31.

Cao, J., Wang, B., Yang, Y. M., and et al. (2018). The nuist earth system model (nesm) version 3: Description and preliminary evaluation. Geoscientific Model Development, 11.

Capecchi, V., Pasi, F., Gozzini, B., and Brandini, C. (2022). A convection-permitting and limited-area model hindcast driven by era5 data: precipitation performances in italy. Climate Dynamics, 61.

Cattani, E., Ferguglia, O., Merino, A., and Levizzani, V. (2021). Precipitation products' inter–comparison over east and southern africa 1983–2017. Remote Sensing, 13(21).

Chen, X. and Zhou, T. (2015). Distinct effects of global mean warming and regional sea surface warming pattern on projected uncertainty in the south asian summer monsoon. Geophysical Research Letters, 42.

Cherchi, A., Fogli, P. G., Lovato, T., and et al. (2019). Global mean climate and main patterns of variability in the cmcc-cm2 coupled model. Journal of Advances in Modeling Earth Systems, 11.

Chow, F. K., Schär, C., Ban, N., and et al. (2019). Crossing multiple gray zones in the transition from mesoscale to microscale simulation over complex terrain. Atmosphere, 10(5).

Daly, C. (2006). Guidelines for assessing the suitability of spatial climate data sets. International Journal of Climatology, 26(6):707–721.

Danabasoglu, G., Lamarque, J. F., Bacmeister, J., and et al. (2020). The community earth system model version 2 (cesm2). Journal of Advances in Modeling Earth Systems, 12.

D*ö*scher, R., Acosta, M., and Alessandri, A. e. a. (2022). The EC-Earth3 Earth system model for the Coupled Model Intercomparison Project 6. Geoscientific Model Development, 15(7):2973–3020.

Deangelis, A. M., Qu, X., Zelinka, M. D., and Hall, A. (2015). An observational radiative constraint on hydrologic cycle intensification. Nature, 528.

Delworth, T. L., Broccoli, A. J., Rosati, A., and et al. (2006). Gfdl's cm2 global coupled climate models. part i: Formulation and simulation characteristics. Journal of Climate, 19.

Dunne, J. P., Horowitz, L. W., Adcroft, A. J., and et al. (2020). The gfdl earth system model version 4.1 (gfdl-esm 4.1): Overall coupled model description and simulation characteristics. Journal of Advances in Modeling Earth Systems, 12.

Eyring, V., Bony, S., Meehl, G. A., and et al. (2016). Overview of the coupled model intercomparison project phase 6 (cmip6) experimental design and organization. Geoscientific Model Development, 9.

Ferguglia, O., von Hardenberg, J., and Palazzi, E. (2023). Robustness of precipitation emergent constraints in cmip6 models. Climate Dynamics, 61.

Field, C., Barros, V., Stocker, T. F., and et. al (2012). IPCC 2012: Managing the Risks of Extreme Events and Disasters to Advance Climate Change Adaptation. Cambridge University Press, Cam-

bridge, United Kingdom and New York.

Gettelman, A., Hannay, C., Bacmeister, J. T., and et al. (2019). High climate sensitivity in the community earth system model version 2 (cesm2). Geophysical Research Letters, 46.

Giorgetta, M. A., Jungclaus, J., Reick, C. H., and et al. (2013). Climate and carbon cycle changes from 1850 to 2100 in mpi-esm simulations for the coupled model intercomparison project phase 5. Journal of Advances in Modeling Earth Systems, 5.

Giorgi, F., Torma, C., and et al., E. C. (2016). Enhanced summer convective rainfall at alpine high elevations in response to climate warming. Nature Geoscience, 9.

Gobiet, A., Kotlarski, S., and et al., M. B. (2014). 21st century climate change in the european alps-a review. Science of the Total Environment, 493.

Goodison, B., Louie, P., and Yang, D. (1998). Wmo solid precipitation measurement intercomparison. World Meteorological Organization-Publications-WMO TD, 67.

Goosse, H. (2015). Climate System Dynamics and Modelling. Cambridge University Press.

Guo, X., Wang, L., Tian, L., and Li, X. (2017). Elevation-dependent reductions in wind speed over and around the tibetan plateau. International Journal of Climatology, 37.

Hall, A., Cox, P., Huntingford, C., and Klein, S. (2019). Progressing emergent constraints on future climate change. Nature Climate Change, 9.

Hall, A. and Qu, X. (2006). Using the current seasonal cycle to constrain snow albedo feedback in future climate change. Geophysical Research Letters, 33.

Hamouda, M. and Pasquero, C. (2021). European extreme precipitation: The effects of spatio-temporal resolution of the data. Weather and Climate Extremes, 33:100337.

Harsch, M. A., Hulme, P. E., McGlone, M. S., and Duncan, R. P. (2009). Are treelines advancing? a global meta-analysis of treeline response to climate warming. Ecology Letters, 12(10):1040–1049.

Hartigan, J. A. and Wong, M. A. (1979). Algorithm as 136: A k-means clustering algorithm. Journal of the Royal Statistical Society. Series C (Applied Statistics), 28(1):100–108.

Henderson-Sellers, A. (1995). Future climates of the world: a

modelling perspective. Elsevier Science.

Hersbach, H., Bell, B., Berrisford, P., and et al.. (2023). Era5 hourly data on single levels from 1940 to present. Copernicus Climate Change Service (C3S) Climate Data Store (CDS).

Hourdin, F., Foujols, M. A., Codron, F., and et al. (2013). Impact of the lmdz atmospheric grid configuration on the climate and sensitivity of the ipsl-cm5a coupled model. Climate Dynamics, 40.

Houze, R. (2012). Orographic effects on precipitating clouds. Reviews of Geophysics, 50:1001–.

Hu, W., Yao, J., He, Q., and Chen, J. (2021). Elevation-dependent trends in precipitation observed over and around the tibetan plateau from 1971 to 2017. Water (Switzerland), 13.

Humaira, H. and Rasyidah, R. (2020). Determining the appropiate cluster number using elbow method for k-means algorithm.

Hurrell, J. W., Holland, M. M., Gent, P. R., and et al. (2013). The community earth system model: A framework for collaborative research. Bulletin of the American Meteorological Society, 94.

Huss, M., Bookhagen, B., and et al., C. H. (2017). Toward mountains without permanent snow and ice.

Huss, M. and Hock, R. (2018). Global-scale hydrological response to future glacier mass loss. Nature Climate Change, 8.

Im, E.-S. and Ahn, J. B. (2011). On the elevation dependency of present-day climate and future change over korea from a high resolution regional climate simulation. Journal of the Meteorological Society of Japan, 89:89–100.

Immerzeel, W. W. (2020). Importance and vulnerability of the world's water towers. Nature, 577:364–369.

Johnson, G. L. and Hanson, C. L. (1995). Topographic and atmospheric influences on precipitation variability over a mountainous watershed. Journal of Applied Meteorology and Climatology, 34(1):68 – 87.

Karl, T. R., Nicholls, N., and Ghazi, A. (1999a). Clivar/gcos/wmo workshop on indices and indicators for climate extremes - workshop summary. volume 42.

Karl, T. R., Nicholls, N., and Ghazi, A. (1999b). Clivar/gcos/wmo workshop on indices and indicators for climate extremes workshop summary. Climatic Change, 42(1):3–7.

Kim, Y.-H., Min, S.-K., Zhang, X., Sillmann, J., and Sandstad, M.

(2020). Evaluation of the cmip6 multi-model ensemble for climate extreme indices. Weather and Climate Extremes, page 100269.

Kittel, T., Thornton, P., Royle, J., and Chase, T. (2002). Climates of the rocky mountains: Historical and future patterns. In Fagerberg, J., Mowery, D. C., and Nelson, R. R., editors, Rocky Mountain Futures: An Ecological Perspective, chapter 4. Island Press, Covelo, CA.

Klein, S. A. and Hall, A. (2015). Emergent constraints for cloud feedbacks. Current Climate Change Reports, 1.

Kochendorfer, J., Rasmussen, R., and Wolff, M. e. a. (2017). The quantification and correction of wind-induced precipitation measurement errors. Hydrology and Earth System Sciences, 21:1973–1989.

Kotlarski, S., Bosshard, T., Lüthi, D., Pall, P., and Schär, C. (2012). Elevation gradients of european climate change in the regional climate model cosmo-clm. Climatic Change, 112.

Kotz, M., Levermann, A., and Wenz, L. (2022). The effect of rainfall changes on economic production. Nature, 601:223–227.

Krakauer, N. Y., Pradhanang, S. M., Lakhankar, T., and Jha, A. K. (2013). Evaluating satellite products for precipitation estimation in mountain regions: A case study for nepal. Remote Sensing, 5(8):4107–4123.

Kriegler, E., Bauer, N., Popp, A., and et al. (2017). Fossil-fueled development (ssp5): An energy and resource intensive scenario for the 21st century. Global Environmental Change, 42.

Krishnan, R., Swapna, P., Vellore, R., and et al. (2019). The IITM Earth System Model (ESM): Development and Future Roadmap.

Kuhn, M. (1989). The Response of the Equilibrium Line Altitude to Climate Fluctuations: Theory and Observations.

Kuhn, M. and Olefs, M. (2020). Elevation-Dependent Climate Change in the European Alps.

Kumar, P. V., Naidu, c., and Prasanna, K. (2020). Recent unprecedented weakening of indian summer monsoon in warming environment. Theoretical and Applied Climatology, 140.

Lavers, D., Simmons, A., Vamborg, F., and Rodwell, M. (2022). An evaluation of era5 precipitation for climate monitoring. Quarterly Journal of the Royal Meteorological Society, 148.

Lee, W. L., Wang, Y. C., Shiu, C. J., and et al. (2020). Taiwan earth system model version 1: Description and evaluation of mean state.

Geoscientific Model Development, 13.

Lei, X., Xu, C., Liu, F., Song, L., Cao, L., and Suo, N. (2023). Evaluation of cmip6 models and multi-model ensemble for extreme precipitation over arid central asia. Remote Sensing, 15:2376.

Levizzani, V. and Cattani, E. (2019). Satellite remote sensing of precipitation and the terrestrial water cycle in a changing climate. Remote Sensing, 11(19).

Li, C. and Yanai, M. (1996). The onset and interannual variability of the asian summer monsoon in relation to land–sea thermal contrast. Journal of Climate, 9(2):358 – 375.

Li, G., Xie, S. P., He, C., and Chen, Z. (2017a). Western pacific emergent constraint lowers projected increase in indian summer monsoon rainfall. Nature Climate Change, 7.

Li, H., Li, Y., Shen, W., and et al. (2015). Elevation-dependent vegetation greening of the yarlung zangbo river basin in the southern tibetan plateau, 1999–2013. Remote Sensing, 7:16672–16687.

Li, L., Lin, P., Yu, Y., and et al. (2013). The flexible global ocean-atmosphere-land system model, grid-point version 2: Fgoals-g2. Advances in Atmospheric Sciences, 30.

Li, L., Yu, Y., Tang, Y., and et al. (2020). The flexible global ocean-atmosphere-land system model grid-point version 3 (fgoals-g3): Description and evaluation. Journal of Advances in Modeling Earth Systems, 12.

Li, X., Wang, L., Guo, X., and Chen, D. (2017b). Does summer precipitation trend over and around the tibetan plateau depend on elevation? International Journal of Climatology, 37(S1):1278–1284.

Lin, J.-L. (2007). The double-itcz problem in ipcc ar4 coupled gcms: ocean-atmosphere feedback analysis. Journal of Climate - J CLIMATE, 20.

Liu, X., Cheng, Z., Yan, L., and Yin, Z.-Y. (2009). Elevation dependency of recent and future minimum surface air temperature trends in the tibetan plateau and its surroundings. Global and Planetary Change, 68:164–174.

Martin, G. M., Bellouin, N., Collins, W. J., and et al. (2011). The hadgem2 family of met office unified model climate configurations. Geoscientific Model Development, 4.

Masson-Delmotte, V., Zhai, P., Pirani, A., and et al. (2021). IPCC 2021: The Physical Science Basis. Contribution of Working Group I

to the Sixth Assessment Report of the Intergovernmental Panel on Climate Change. Cambridge University Press, Cambridge, United Kingdom and New York.

Mauritsen, T., Bader, J., Becker, T., and et al. (2019). Developments in the mpi-m earth system model version 1.2 (mpi-esm1.2) and its response to increasing co2. Journal of Advances in Modeling Earth Systems, 11.

Meehl, G. and Washington, W. (1996). El nino-like climate change in a model with increased atmospheric co2 concentrations. Nature, 382:56–60.

Meehl, G. A., Covey, C., Delworth, T., and et al. (2007). The wcrp cmip3 multimodel dataset: A new era in climatic change research. Bulletin of the American Meteorological Society, 88.

Meehl, G. A., Washington, W. M., Arblaster, J. M., and et al. (2012). Climate system response to external forcings and climate change projections in ccsm4. Journal of Climate, 25.

Mei, Y., Anagnostou, E., Nikolopoulos, E., and Borga, M. (2014). Error analysis of satellite rainfall products in mountainous basins. Journal of Hydrometeorology, 15:1778 – 1793.

Meinshausen, M., Smith, S. J., Calvin, K., and et al. (2011). The rcp greenhouse gas concentrations and their extensions from 1765 to 2300. Climatic Change, 109.

Merino, A., García-Ortega, E., and Navarro Martínez, A. e. a. (2021). Evaluation of gridded rain-gauge-based precipitation datasets: Impact of station density, spatial resolution, altitude gradient and climate. International Journal of Climatology, 41.

Minder, J. R., Letcher, T. W., and Liu, C. (2018). The character and causes of elevation-dependent warming in high-resolution simulations of rocky mountain climate change. Journal of Climate, 31.

Mote, P. W., Li, S., Lettenmaier, D. P., Xiao, M., and Engel, R. (2018). Dramatic declines in snowpack in the western us. npj Climate and Atmospheric Science, 1.

Musselman, K. N., Clark, M. P., Liu, C., Ikeda, K., and Rasmussen, R. (2017). Slower snowmelt in a warmer world. Nature Climate Change, 7.

Müller, W. A., Jungclaus, J. H., Mauritsen, T., and et al. (2018). A higher-resolution version of the max planck institute earth system model (mpi-esm1.2-hr). Journal of Advances in Modeling Earth Systems, 10.

Napoli, A., Crespi, A., Ragone, F., Maugeri, M., and Pasquero, C. (2019). Variability of orographic enhancement of precipitation in the alpine region. Scientific Reports, 9.

Napoli, A., Pepin, N., Palazzi, E., and Zardi, D. (2023). A workshop on advances in our understanding of elevation dependent climate change. volume 40.

Neelin, J. D. (2010). Climate models, page 145–192. Cambridge University Press.

O' Gorman, P. A. (2012). Sensitivity of tropical precipitation extremes to climate change precipitation extremes increase in intensity over many regions of the globe in simulations of a warming climate. Nature Geoscience, 5.

O'Gorman, P. A. (2014). Contrasting responses of mean and extreme snowfall to climate change. Nature, 512:416–8.

O'Gorman, P. A. and Schneider, T. (2009). The physical basis for increases in precipitation extremes in simulations of 21st-century climate change. Proceedings of the National Academy of Sciences of the United States of America, 106.

Ohmura, A. (2012). Enhanced temperature variability in high-altitude climate change. Theoretical and Applied Climatology, 110.

Oyler, J. W., Dobrowski, S. Z., Ballantyne, A. P., Klene, A. E., and Running, S. W. (2015). Artificial amplification of warming trends across the mountains of the western united states. Geophysical Research Letters, 42.

O'Gorman, P. A. (2015). Precipitation extremes under climate change.

Pak, G., Noh, Y., and et al., M.-I. L. (2021). Korea institute of ocean science and technology earth system model and its simulation characteristics. Ocean Science Journal, 56.

Palazzi, E., Filippi, L., and von Hardenberg, J. (2016). Insights into elevation-dependent warming in the tibetan plateau-himalayas from cmip5 model simulations. Climate Dynamics, 48.

Palazzi, E., Hardenberg, J., and Provenzale, A. (2013). Precipitation in the hindu-kush karakoram himalaya: Observations and future scenarios. Journal of Geophysical Research, 118:85–100.

Palazzi, E., Mortarini, L., Terzago, S., and von Hardenberg, J. (2019). Elevation-dependent warming in global climate model simulations at high spatial resolution. Climate Dynamics, 52.

Palazzi, E., von Hardenberg., J., Terzago, S., and Provenzale, A.

(2014). Precipitation in the karakoram-himalaya: a cmip5 view. Climate Dynamics, 45.

Parmesan, C. (2006). Ecological and evolutionary responses to recent climate change.

Pendergrass, A. G. (2020). The global-mean precipitation response to co2-induced warming in cmip6 models. Geophysical Research Letters, 47.

Pepin, N., Bradley, R. S., Diaz, H. F., and et al. (2015). Elevation-dependent warming in mountain regions of the world. Nature Climate Change, 5.

Pepin, N. C., Arnone, E., Gobiet, A., and et al. (2022). Climate changes and their elevational patterns in the mountains of the world. Reviews of Geophysics, 60.

Pepin, N. C. and Lundquist, J. (2008). Temperature trends at high elevations: Patterns across the globe. Geophysical Research Letters, 35(14).

Piao, S., Friedlingstein, P., Ciais, P., and et al. (2007). Changes in climate and land use have a larger direct impact than rising co2 on global river runoff trends. Proceedings of the National Academy of Sciences, 104(39):15242–15247.

Portner, H. O., Roberts, D., Masson-Delmotte, V., and et al. (2019). IPCC 2019: Special Report on the Ocean and Cryosphere in a Changing Climate. Cambridge University Press, Cambridge, United Kingdom and New York.

Potter, E., Fyffe, C., and Orr, A. e. a. (2023). A future of extreme precipitation and droughts in the peruvian andes. Climate and Atmospheric Science, 6.

Rangwala, I., Miller, J., and Xu, M. (2009). Warming in the tibetan plateau: Possible influences of the changes in surface water vapor. Geophysical Research Letters, 36.

Rangwala, I. and Miller, J. R. (2012). Climate change in mountains: A review of elevation-dependent warming and its possible causes. Climatic Change, 114.

Rangwala, I., Sinsky, E., and Miller, J. (2016). Variability in projected elevation dependent warming in boreal midlatitude winter in cmip5 climate models and its potential drivers. Climate Dynamics, 46.

Rotstayn, L. D., Jeffrey, S. J., Collier, M. A., and et al. (2012). Aerosol- and greenhouse gas-induced changes in summer rainfall and

circulation in the australasian region: A study using single-forcing climate simulations. Atmospheric Chemistry and Physics, 12.

Rowell, D. P. (2019). An observational constraint on cmip5 projections of the east african long rains and southern indian ocean warming. Geophysical Research Letters, 46.

Samset, B. H., Sand, M., Smith, C. J., and Bauer, S. E. e. a. (2018). Climate impacts from a removal of anthropogenic aerosol emissions. Geophysical Research Letters, 45(2):1020–1029.

Sanderson, B. M., Pendergrass, A. G., Koven, C. D., and et al. (2021). The potential for structural errors in emergent constraints. Earth System Dynamics, 12.

Scherrer, S., Ceppi, P., Croci-Maspoli, M., and Appenzeller, C. (2012). Snow-albedo feedback and swiss spring temperature trends. Theoretical and Applied Climatology, 110.

Schlund, M., Lauer, A., Gentine, P., Sherwood, S. C., and Eyring, V. (2020). Emergent constraints on equilibrium climate sensitivity in cmip5: Do they hold for cmip6? Earth System Dynamics, 11.

Schneebeli, M., Dawes, N., Lehning, M., and Berne, A. (2013). High-resolution vertical profiles of x-band polarimetric radar observables during snowfall in the swiss alps. Journal of Applied Meteorology and Climatology, 52:378–394.

Schär, C., Davies, T. D., Frei, C., Wanner, H., and et al. (1998). Current alpine climate. In Cebon, P., Dahinden, U., Davies, H., Imboden, D., and Jäger, C., editors, Views from the Alps: regional perspectives on climate change, pages 21–72. MIT Press, Boston.

Seland, Ø., Bentsen, M., and Olivié, D. e. a. (2020). Overview of the norwegian earth system model (noresm2) and key climate response of cmip6 deck, historical, and scenario simulations. Geoscientific Model Development, 13(12):6165–6200.

Shi, X. and Durran, D. R. (2014). The response of orographic precipitation over idealized midlatitude mountains due to global increases in co2. Journal of Climate, 27.

Siler, N. and Roe, G. (2014). How will orographic precipitation respond to surface warming? an idealized thermodynamic perspective. Geophysical Research Letters, 41.

Simpson, I. R., McKinnon, K. A., Davenport, F. V., and et al. (2021). Emergent constraints on the large-scale atmospheric circulation and regional hydroclimate: Do they still work in cmip6 and how much can they actually constrain the future? Journal of Climate, 34.

Singh, P., K. S. R. and Kumar, N. (1995). Topographic influence on precipitation distribution in different ranges of the western himalayas. Nord. Hydrol., (26):259–284.

Sorte, F. A. L. and Jetz, W. (2010). Projected range contractions of montane biodiversity under global warming. Proceedings of the Royal Society B: Biological Sciences, 277.

Stevens, B. and Bony, S. (2013). What are climate models missing? Science, 340(6136):1053–1054.

Stocker, T., Qin, D., Plattner, G. K., and et al. (2013). IPCC, 2013: Climate Change 2013: The Physical Science Basis. Contribution of Working Group I to the Fifth Assessment Report of the Intergovernmental Panel on Climate Change. Cambridge University Press, Cambridge, United Kingdom and New York.

Swart, N. C., Cole, J. N., Kharin, V. V., and et al. (2019). The canadian earth system model version 5 (canesm5.0.3). Geoscientific Model Development, 12.

Takahashi, C., Watanabe, M., and Mori, M. (2017). Significant aerosol influence on the recent decadal decrease in tropical cyclone activity over the western north pacific. Geophysical Research Letters, 44(18):9496–9504.

Tatebe, H., Ogura, T., Nitta, T., and et al. (2019). Description and basic evaluation of simulated mean state, internal variability, and climate sensitivity in miroc6. Geoscientific Model Development, 12.

Taylor, K. E. (2001). Summarizing multiple aspects of model performance in a single diagram. Journal of Geophysical Research: Atmospheres, 106(D7):7183–7192.

Taylor, K. E., Stouffer, R. J., and Meehl, G. A. (2012). An overview of cmip5 and the experiment design. Bulletin of the American Meteorological Society, 93.

Terzago, S., Palazzi, E., and von Hardenberg, J. (2018). Stochastic downscaling of precipitation in complex orography: A simple method to reproduce a realistic fine-scale climatology. Natural Hazards and Earth System Sciences, 18:2825–2840.

Thackeray, C. W., DeAngelis, A. M., Hall, A., Swain, D. L., and Qu, X. (2018). On the connection between global hydrologic sensitivity and regional wet extremes. Geophysical Research Letters, 45.

Thackeray, C. W., Hall, A., Norris, J., and Chen, D. (2022). Constraining the increased frequency of global precipitation extremes under warming. Nature Climate Change, 12.

Thornton, J. M., Palazzi, E., and et al., N. C. P. (2021). Toward a definition of essential mountain climate variables.

Thornton, J. M., Pepin, N., Shahgedanova, M., and Adler, C. (2022). Coverage of in situ climatological observations in the world's mountains. Frontiers in Climate, 4.

Toledo, O., Palazzi, E., Toro, I. M. C., and Mortarini, L. (2022). Comparison of elevation-dependent warming and its drivers in the tropical and subtropical andes. Climate Dynamics, 58.

Vitasse, Y., Hoch, G., Randin, C. F., and et al. (2012). Tree recruitment of european tree species at their current upper elevational limits in the swiss alps. Journal of Biogeography, 39(8):1439–1449.

Viviroli, D., Archer, D. R., and et al., W. B. (2011). Climate change and mountain water resources: Overview and recommendations for research, management and policy. Hydrology and Earth System Sciences, 15.

Viviroli, D., Dürr, H. H., Messerli, B., Meybeck, M., and Weingartner, R. (2007). Mountains of the world, water towers for humanity: Typology, mapping, and global significance. Water Resources Research, 43.

Viviroli, D., Kummu, M., Meybeck, M., Kallio, M., and Wada, Y. (2020). Increasing dependence of lowland populations on mountain water resources. Nature Sustainability, 3.

Voldoire, A., Saint-Martin, D., Sénési, S., and et al. (2019). Evaluation of cmip6 deck experiments with cnrm-cm6-1. Journal of Advances in Modeling Earth Systems, 11.

Voldoire, A., Sanchez-Gomez, E., y Mélia, D. S., and et al. (2013). The cnrm-cm5.1 global climate model: Description and basic evaluation. Climate Dynamics, 40.

Volodin, E. M., Dianskii, N. A., and Gusev, A. V. (2010). Simulating present-day climate with the inmcm4.0 coupled model of the atmospheric and oceanic general circulations. Izvestiya - Atmospheric and Ocean Physics, 46.

Volodin, E. M., Mortikov, E. V., Kostrykin, S. V., and et al. (2017a). Simulation of modern climate with the new version of the inm ras climate model. Izvestiya - Atmospheric and Ocean Physics, 53.

Volodin, E. M., Mortikov, E. V., Kostrykin, S. V., and et al. (2017b). Simulation of the present-day climate with the climate model inmcm5. Climate Dynamics, 49.

von Storch, H. and Zwiers, F. W. (1984). Statistical Analysis in Climate Research.

Watanabe, M., Kamae, Y., Shiogama, H., DeAngelis, A. M., and Suzuki, K. (2018). Low clouds link equilibrium climate sensitivity to hydrological sensitivity. Nature Climate Change, 8.

Watanabe, M., Suzuki, T., O'Ishi, R., and et al. (2010). Improved climate simulation by miroc5: Mean states, variability, and climate sensitivity. Journal of Climate, 23.

Watanabe, S., Hajima, T., Sudo, K., and et al. (2011). Miroc-esm 2010: Model description and basic results of cmip5-20c3m experiments. Geoscientific Model Development, 4.

Watson, R. and the Core Writing Team (2001). Climate change 2001: Synthesis report. a contribution of working groups i, ii, and iii to the third assessment report of the integovernmental panel on climate change. Technical report. 398 pp.

Wilcox, L. J., Highwood, E. J., and Dunstone, N. J. (2013). The influence of anthropogenic aerosol on multi-decadal variations of historical global climate. Environmental Research Letters, 8(2):024033.

Williamson, M. S., Thackeray, C. W., Cox, P. M., Hall, A., Huntingford, C., and Nijsse, F. J. (2021). Emergent constraints on climate sensitivities. Reviews of Modern Physics, 93.

Wu, F., You, Q., Cai, Z., and et al. (2022). Characteristics of elevation dependent warming over the tibetan plateau based on the modis daytime land surface temperature data. Chinese Journal of Atmospheric Sciences, 46:442–454.

Wu, T., Li, W., Ji, J., and et al. (2013). Global carbon budgets simulated by the beijing climate center climate system model for the last century. Journal of Geophysical Research Atmospheres, 118.

Yang, K., Ye, B., and Zhou, D. e. a. (2011). Response of hydrological cycle to recent climate changes in the tibetan plateau. Climatic Change, 109:517–534.

Yang, L., Tian, F., Smith, J., and Hu, H. (2014). Urban signatures in the spatial clustering of summer heavy rainfall events over the beijing metropolitan region. Journal of Geophysical Research: Atmospheres, 119.

Yang, X., Zhou, B., Xu, Y., and Han, Z. (2021). Cmip6 evaluation and projection of temperature and precipitation over china. Advances in Atmospheric Sciences, 38.

Yao, J., Yang, Q., Mao, W., Zhao, Y., and Xu, X. (2016). Precipitation trend-elevation relationship in arid regions of the china. Global and Planetary Change, 143.

Yukimoto, S., Adachi, Y., Hosaka, M., and et al. (2012). A new global climate model of the meteorological research institute: Mri-cgcm3: -model description and basic performance-. Journal of the Meteorological Society of Japan, 90.

Yukimoto, S., Kawai, H., Koshiro, T., and et al. (2019). The meteorological research institute earth system model version 2.0, mri-esm2.0: Description and basic evaluation of the physical component. Journal of the Meteorological Society of Japan, 97.

Zelinka, M. D., Myers, T. A., and McCoy, D. T. e. a. (2020). Causes of higher climate sensitivity in cmip6 models. Geophysical Research Letters, 47.

Zhang, W., Furtado, K., Zhou, T., Wu, P., and Chen, X. (2022). Constraining extreme precipitation projections using past precipitation variability. Nature Communications, 13.

Zhou, S., Zhou, S., Lintner, B., Findell, K., and Zhang, Y. (2023). Projected increase in global runoff dominated by land surface changes. Nature Climate Change, 13:1–8.

Ziehn, T., Chamberlain, M. A., Law, R. M., and et al. (2020). The australian earth system model: Access-esm1.5. Journal of Southern Hemisphere Earth Systems Science, 70.